# Near-Field Scanning Optical Microscopy

Robert C. Dunn

*Department of Chemistry, University of Kansas, Lawrence, Kansas 66045*

*Received March 6, 1999 (Revised Manuscript Received July 15, 1999)*



## *Contents*



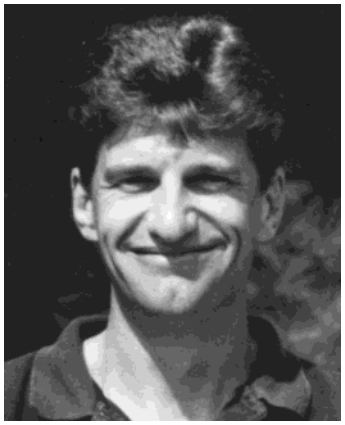

Robert Dunn is an Associate Professor of Chemistry at the University of Kansas. He received his B.S. degree in Chemistry from the California State University at Sacramento in 1988. He obtained his Master's degree in 1990 and his Ph.D. degree in Physical Chemistry in 1992 from the University of California at San Diego working in the area of ultrafast spectroscopy. From there he spent two years as a postdoctoral fellow at Pacific Northwest Laboratory before joining the faculty at the University of Kansas in 1995. His research interests include the study of artificial membranes, protein channels, and single molecule dynamics using novel high-resolution techniques. His group is also active in developing nanometric chemical sensors and in exploring new techniques for high-resolution optical measurements.

## *I. Introduction*

The ability to view and study samples under high magnification is enormously important in many disciplines such as the biological sciences and materials research. Traditionally, optical techniques have been the most widely employed for these purposes given their long historical development, noninvasiveness, specificity, ease of use, and relatively low cost. However, the spatial resolution attainable with conventional optical techniques is limited to approximately half the wavelength of the light source used. For visible radiation, this results in a theoretical resolution limit of 200−300 nm which is restrictive for many applications. This limitation motivated the development of higher resolution techniques such as scanning electron microscopy (SEM) and transmission electron microscopy (TEM) along with the recent emergence of other scanning probe techniques such as atomic force microscopy (AFM) and scanning tunneling microscopy (STM). The introduction of these and related forms of microscopy have brought about fantastic gains in resolution to the point where it is now possible to image and study single atoms.

These gains in resolution, however, have been made at the expense of the optical contrast mechanisms available to light microscopy. The spectroscopic capabilities, high temporal resolution, and polarization properties inherent in optical microscopy are enormously powerful and informative for many applications. Moreover, many of the higher resolution techniques place increased demands on sample preparation and have reduced flexibility in the possible working environments. For example, SEM applications require that the sample be vacuum compatible and, in most cases, conductive. For biological samples, these conditions are met by extensive sample drying and coating with conductive materials. While these techniques have provided a wealth of important structural data on biological samples, the extreme sample conditions and environments preclude in vitro

10.1021/cr980130e CCC: $35.00 
Published on Web 09/24/1999

or dynamic measurements. AFM, on the other hand, can be used to study samples near the atomic level at ambient conditions but yields little chemical information. For the most part, AFM reveals topographical information which can be difficult to interpret for samples with complicated morphology. Ideally, one would like to combine the high resolution of these techniques with the sensitivity, specificity, and flexibility afforded by optical techniques. This goal has driven the development of near-field scanning optical microscopy (NSOM or SNOM) which can be used to conduct optical measurements with a spatial resolution beyond the classical diffraction limit.[1−28]

The diffraction limit in conventional microscopy arises from the size of the spot that a light beam can be focused to with normal lens elements. At the focal point, the beam forms a symmetric pattern of concentric rings known as the Airy disk pattern. The dimensions of the Airy disk pattern were first described in detail by Ernst Abbe in 1873.[29] From Abbe, the distance, $d$, from the highest intensity point located in the middle of the center spot, to the first node in intensity is given by

$$d = 0.61(\lambda_0/n \sin \theta) \quad (1)$$

where $\lambda_0$ is the vacuum wavelength, $n$ is the refractive index of the medium in which the light travels, and $\theta$ is the light convergence angle for the focusing element. The denominator in eq 1, $n \sin \theta$, is also known as the numerical aperture (NA) for the objective and can be as high 1.3−1.4 for modern objectives working in high-index mediums such as water or oil. Now that the intensity profile of the focused light beam can be described, the question of resolution arises. How close can two objects reside and still be resolvable by an ideal optical system using a lens?

The accepted practice is to invoke the Rayleigh criterion which states that two objects are resolvable if they are separated by a distance at least equal to the distance given in eq 1. As stated earlier, numerical apertures of 1.3−1.4 are now obtainable with high-quality objective lenses; therefore, eq 1 is usually simplified to $d = \lambda/2$. The maximal resolution is then approximately equal to half the wavelength of the radiation used, which for visible light applications results in a spatial resolution of 250−300 nm. The arbitrary nature of the definition, however, only provides guidance for determining the optical resolution, and in actual practice, the experimental situation is often quite different. For instance, with excellent signal-to-noise and/or an accurate description of the instrumental response function, smaller distances can often be determined. More often, however, the experimental conditions and aberrations in the optical components conspire to lower the resolution and prevent attainment of the theoretical limit.

These limitations have been well-known for some time and, not surprisingly, led many to begin exploring alternative ways of achieving higher resolution optical measurements. Early in the 20th century, Synge published a series of visionary papers in which he proposed a new type of optical microscope designed to circumvent the limitations imposed by the diffraction limit.[30−32] This remarkable collection of papers details the foundations upon which the modern day NSOM is based. Although technically challenging to implement, Synge's idea to beat the diffraction limit was eloquently simple.

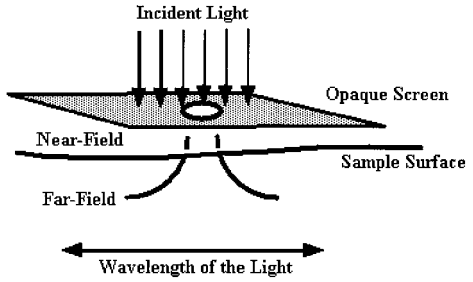


**Figure 1.** Schematic representation of Synge's idea for achieving subdiffraction limit spatial resolution. Incident radiation is passed through a small, subwavelength hole in an opaque screen. By the positioning of the screen close to the sample, the emerging radiation is forced to interact with the sample before diffracting out.

Synge proposed forming a microscopic aperture with dimensions much smaller than the optical wavelength in an opaque screen.[30−32] By illuminating the backside of the screen with a high-intensity light source, light passing through the aperture would be confined by the dimensions of the hole. This is shown schematically in Figure 1. Once positioned in close proximity to the sample surface, the light emerging from the aperture could be used to image a specimen before it had time to diffract out and degrade the resolution. Included in Synge's original proposal was a keen awareness of the technical difficulties that would have to be overcome to construct such a microscope.[30−32] The difficulties in aperture formation, illumination, and sample manipulation were all recognized as hurdles that would have to be overcome.

The experimental feasibility of high-resolution imaging using a subwavelength aperture was first demonstrated by Ash and Nicholls in 1972 using microwave radiation.[33] With 3 cm microwaves passing through a small aperture, periodic features in a metal grating sample were measured with $\lambda/60$ spatial resolution. These exciting results illustrated the feasibility of Synge's idea and renewed interest in carrying out similar experiments using visible radiation. However, the much shorter wavelengths associated with visible light imposed technological difficulties in aperture formation and positioning that required another decade to overcome.

It was not until the mid 1980s that Pohl's laboratory at IBM Zurich first reported subdiffraction-limited optical measurements using the ideas outlined by Synge a half century earlier.[34,35] This group and another group working independently at Cornell University overcame the significant technical barriers associated with subdiffraction-limited optical imaging and started the developmental activity which has resulted in the modern day NSOM instrument.[34−38] While still not completely routine, high-resolution optical measurements with NSOM are beginning to address important questions ranging

from solid-state physics to biology. The sensitivity of the technique has been amply demonstrated through single molecule measurements while the high spatial resolution has revealed previously undiscovered features in a variety of samples.

The number and breadth of applications using NSOM to gain insight into sample properties at the submicrometer level is expanding at a rapid pace. Applications that are discussed here include examples of NSOM in single molecule studies,[39−67] thin film analysis,[11,21,59,63,68−119] and probing biological samples.[19,36,40,41,46,49,52,53,58,66,67,112,120−156] An effort has been made to highlight those applications that benefit from the unique imaging capabilities of NSOM. For instance, single molecule diffusion experiments illustrate how the low detection limits and high spatial resolution can yield new, previously hidden, dynamics at interfaces. The plethora of measurements on thin films from conducting polymers to liquid crystals demonstrates both the flexibility in the optical contrast mechanisms and the power of collecting simultaneous optical and topographical information. For biological samples, the examples discussed portray a technique posed to make a significant impact once issues involved in imaging soft and often dynamic samples are resolved. While NSOM measurements on fixed cells both dry and under buffered conditions have become routine, the extension to unfixed cells has proven problematic. Once this hurdle is overcome, as it certainly will be soon, the potential for measuring the structure and dynamics of living cells at the nanometric level offers exciting possibilities.

To limit the scope of this review, solid-state applications will not be covered here although it could easily be argued that the resolution gains over conventional far-field techniques are greatest in the extreme environments (low temperature, high vacuum, etc.) that many of these studies are conducted. Before discussion of the applications that will be covered here, a short description of common microscope designs and the most prevalent techniques for forming the nanometric light source and positioning it close to the sample surface will be presented. In addition, since the interpretation of NSOM images requires a knowledge of the fields present at the end of the NSOM tip, theoretical treatments of light passing through small apertures will be discussed.

## *II. NSOM*

### II.A. NSOM Microscope

The final NSOM design can take on several forms depending on the particular needs of the research. One of the common microscope designs utilized for NSOM measurements is shown in Figure 2. In this design, the NSOM is built atop an inverted fluorescence microscope. This is particularly well suited for applications in which the normal imaging modes of the inverted microscope are still required to locate and study the sample before performing the higher resolution NSOM experiments.

As shown in Figure 2, laser light is passed through a band-pass filter to remove unwanted colors followed by a combination of half-wave and quarter-wave plates to control the polarization of the light. This light is then coupled into a single mode optical fiber, the end of which is fabricated into the NSOM tip. In the arrangement shown, the near-field tip is mounted in a *z*-piezo tube which controls the tip−sample gap during scanning. The transparent sample is mounted in a separate *x*−*y* piezo stage which scans the sample under the tip during the experiment. Light exiting the NSOM tip excites fluorescence in the sample which is collected from below using a high numerical aperture microscope objective. Residual laser excitation light is removed using filters, and the remaining fluorescence signal is imaged onto a high quantum efficiency detector, such as an avalanche photodiode operating in single photon counting mode. The software and electronics necessary to scan the piezos and record images are similar to that used in atomic force microscopy.

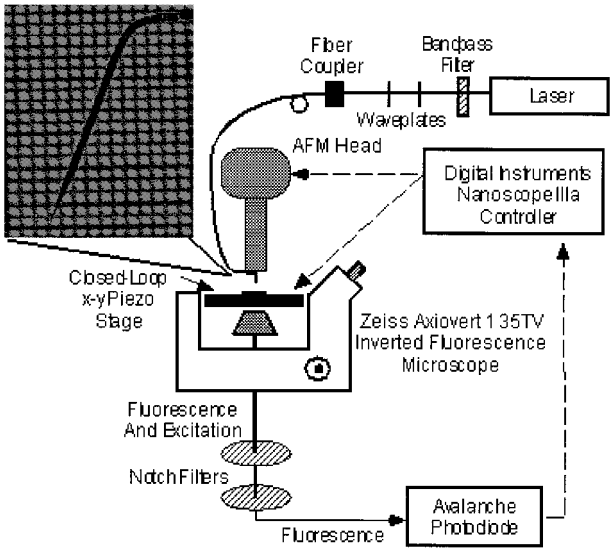


**Figure 2.** Schematic of a near-field microscope built around an inverted fluorescence microscope. In this particular NSOM, a cantilevered fiber optic probe is used although the basic design remains unchanged for straight fiber probes. Laser light is filtered and passed through waveplates to control the polarization and then sent into an optical fiber, the end of which is fashioned into a near-field probe. The tip is held in a *z*-piezo head which is positioned above the sample. The sample is mounted in a separate *x*−*y* piezo stage which scans the sample under the tip while imaging. Radiation emerging from the tip illuminates the sample, and light is collected from below with a high NA objective. The light is filtered and imaged onto an avalanche photodiode. Electronics similar to that used in AFM are used to drive the scans and record the images. The experimental arrangement shown is designed for fluorescence measurements on transparent samples.

There are several NSOM configurations that can be utilized, the choice of which is often dictated by sample properties or working environments.[1−3,6,8,10,15] The particular NSOM configuration shown in Figure 2 is usually referred to as illumination mode NSOM. In this mode, the NSOM tip illuminates the sample and light (transmitted or fluorescence) is collected from beneath the transparent sample. In collection mode, the sample is illuminated from the far-field and the NSOM probe is used to collect light. For opaque samples, reflection mode is utilized in which

the NSOM probe illuminates the sample and light is either collected back through the same probe (shared aperture) or from the side with a long working distance collection element. Another common mode utilizes the tip to frustrate an evanescent wave produced in a sample by total internal reflectance. This generates propagating waves that can be collected by the probe and is generally referred to as photon tunneling microscopy.[157−163]

Despite minor variations in design, all NSOMs share common features such as the small nanometric NSOM tip used as the excitation source and/or collection element and a mechanism for positioning and holding the NSOM tip within nanometers of the sample surface during scanning. These two features pose the greatest technical challenge in the implementation of NSOM and will be discussed in more detail below.

## II.B. Fiber Optic NSOM Probes

The heart of any near-field microscope lies in the quality of the aperture used to deliver the nanometric spot of light. Early NSOM tip designs included etched quartz crystals and pulled micropipets, but these tips generally suffered from low throughput and poor reproducibility.[26,34−37] By far, the most successful NSOM tip design to date was introduced by Betzig et. al. at AT&T Bell Labs and makes use of a tapered fiber optic waveguide coated with a reflective metal coating.[5,164]

These tips are fabricated by heating and pulling a single mode optical fiber down to a fine point in a commercial micropipet puller.[5] By control of the heating and pulling parameters, highly reproducible tapers and tip diameters can be produced. Excellent sources are available that discuss the mechanical and optical properties produced by different taper shapes.[10,165,166] In general, throughput for a given aperture size increases as the taper angle of the tip becomes more steep. As the diameter of the fiber in the taper region is reduced beyond the mode-field cutoff of the waveguide, light escapes from the sides of the tip which prevents the formation of a well-defined aperture. To form an aperture, the sides of the probe must be coated with an opaque metal to confine the light.[4−6,34] For visible radiation, aluminum has the smallest skin depth (≈13 nm at 500 nm) and, therefore, should require the least amount of coating thickness. This, however, is complicated by the propensity for grain formation in aluminum which decreases the reflectivity of the film. To block light from escaping, approximately 50−100 nm of aluminum is coated around the sides of the taper region. It should also be mentioned that silver coatings have been successfully used with no apparent loss in tip performance.[12,79,81,167] A schematic view of an aluminum-coated optical fiber tip is shown in Figure 3.

Vacuum evaporative techniques are usually employed to deposit the aluminum coating around NSOM tips. Although it is generally accepted that sputtering leads to higher quality metal films, for aluminum this does not seem to be the case. Evaporation of aluminum is much faster than sputtering, thus reducing the time available for oxide formation at the freshly deposited metal surface. Oxides of aluminum are known to increase the surface roughness and decrease the coating reflectivity, both of which are extremely important parameters in NSOM tip fabrication.[168−170] Grain formation is well understood during the coating process and can be minimized by reducing the background pressure, increasing the coating rate, and reducing the partial pressure of oxygen and water in the vacuum chamber.[165,171] Reducing the temperature of the substrate should also produce smoother aluminum coatings, but this has proven difficult to implement.

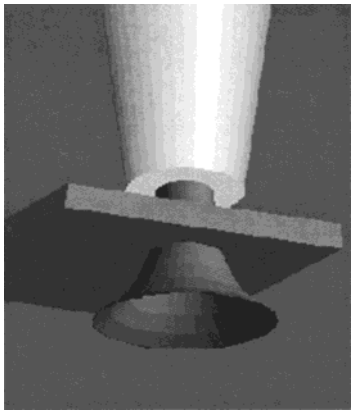

**Figure 3.** Idealized view of a metal-coated fiber optic probe used to deliver light to dimensions small than the optical wavelength.

Evaporative techniques are also desirable for NSOM tip fabrication because they are line-of-sight. Simply pointing the NSOM probe away from the evaporation source during film deposition allows the aperture at the end of the tip to remain uncoated. Rotating the tips during coating leads to an even metal coating around the sides of the tip. As in any scanning probe technique, the quality of the images obtained is largely a function of the probe used in the imaging. This seems to be especially true for NSOM. Obtaining a high-quality, smooth aluminum coating on the near-field tip is critical for high-resolution measurements.[165,171] Scanning electron micrographs of NSOM tips with various sized tip apertures are shown in Figure 4.[172] These coatings are extremely smooth for aluminum, yet grain structures are clearly visible around the tip aperture and are a common feature of NSOM tips.

The power output and throughput efficiency of these probes is highly dependent on the particular parameters of the tip. Typically, however, tips with 80−100 nm diameter apertures can deliver tens of nanowatts of light with hundreds of microwatts coupled into the fiber. Although restrictive for some applications, nanowatts of output power is still relatively high considering the small size of the aperture. The power density exiting the near-field tip is on the order of 100 W/cm$^2$ which has proven adequate for many applications. The inefficiency of the tips ($10^{-4}$−$10^{-7}$) results from the transition from propagating to evanescent waves as the diameter in the taper region decreases beyond cutoff. The light lost is either reflected back up the fiber from the taper region or is lost by absorption into the alumi-

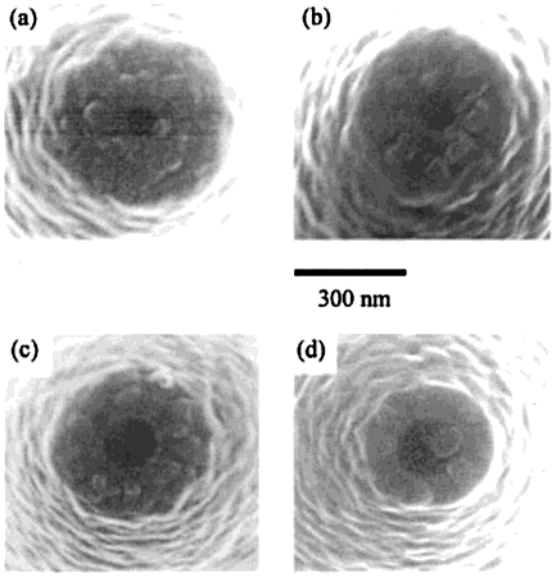


**Figure 4.** Scanning electron microscope images of four aluminum-coated probes with apparent apertures ranging in size from 80 to 150 nm. The grain structures in the aluminum coating can been seen in these magnified views. Reproduced with permission from ref 172. Copyright 1998 American Institute of Physics.

num coating.[173,174] The heating from the absorption of light by the aluminum coating ultimately limits the output power available from a tip. Local heating near the end of the probe can damage the aluminum coating thermally or as a result of stresses introduced through the differential thermal expansions of the glass and aluminum.[175−178] In either case, the tip aperture is usually damaged in the process, rendering it unsuitable for high-resolution imaging.

Temperature profiles along the taper of a NSOM tip have been calculated and measured experimentally by several groups.[175−178] The heating is shown to strongly depend on the taper angle of the tip, decreasing with increasing taper angle. In one study, temperature coefficients varied from 20 K/mW for a large cone angle tip to 60 K/mW for a tip with a longer, less severely tapered tip.[176] In these measurements, the change in temperature was measured approximately 70 $\mu$m from the tip aperture and the coefficients are reported as a function of the power coupled into the tip. The temperature increase was linear with input power until thermal damage eventually occurred at 470 °C with an input power of 9.5 mW. Since this temperature is lower than the melting point of aluminum (660 °C), the failure was ascribed to thermal expansion stress as mentioned earlier.[176]

For some applications, the low efficiency and output from pulled fiber optic probes remains problematic. Low signal applications such as single molecule spectroscopy[39−67] and Raman spectroscopy[135,179−183] or more applied applications in data storage or high-speed imaging[13,14,27,184,185] will all benefit from more efficient NSOM probes. This has led to the exploration of alternative methods of taper formation that offer more control over the cone angle of the tip. Ohtsu and co-workers have been developing etching techniques that can be used to create a variety of novel probe structures.[27,186−188] Several

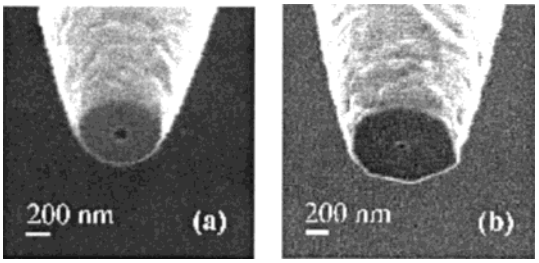


**Figure 5.** Scanning electron microscope images of two NSOM probes in which the ends have been milled flat using a focused ion beam. The apertures have apparent diameters of (a) 120 nm and (b) 35 nm. Reproduced with permission from ref 195. Copyright 1998 American Institute of Physics.

groups have shown that etching techniques can be utilized to fabricate NSOM tips with large cone angles.[96,183,188−193] These tips are at least 1 order of magnitude more efficient than their pulled counterparts. The tips are etched in a 40% HF solution that contains an overlayer of a protecting substance such as *p*-xylene and the tip is produced as the meniscus along the fiber is formed. The choice of the protecting layer dictates the cone angle that is produced.[96,183,188−193] These methods look very promising and eventually may replace the more popular pulling methods in the future.

Another area that is currently leading to vastly improved probe performance involves milling the tip aperture using a focused ion beam (FIB).[194−196] FIB milling can produce structures on the nanometer scale which allow precise alterations to be made in the geometry of the NSOM tip. As shown in Figure 4, when viewed under high magnification, the aperture of an aluminum coated NSOM probe contains grains in the coating that protrude beyond the actual boundary of the pulled fiber.[172] These grains produce several undesirable effects. The structures physically restrict the approach of the tip to the sample, thus limiting the attainable resolution and lowering the intensity seen at the sample. They also reduce the symmetry of the probe aperture and complicate the polarization properties of the light delivered with the tip.

FIB milling can essentially be used to slice off the very end of the NSOM probe to produce a very flat and unstructured aperture region.[194−196] Figure 5 presents SEM images of two NSOM tips that have been milled using an FIB.[195] The tips shown in Figure 5a,b have tip apertures of 120 and 35 nm, respectively. The face of the tip is remarkably smooth following the FIB milling having eliminated the complicated grain structures seen previously (Figure 4). Fluorescence imaging of single molecules was used to test the modified probes. Incredibly, a 1 order of magnitude increase in the fluorescence count rate from a single molecule was observed compared to similar measurements made with unmodified probes.[195] This reflects the ability to position the modified probe in close proximity to the sample. Polarization ratios for the tips were also enhanced with some exhibiting ratios higher than 100:1 in all directions with maximum ratios greater than 250:1.[195]

The results indicate that FIB milling produces a superior aperture over unmodified tips. It may also be possible to use this process to create novel new tip structures that act as waveguides with no cutoff.[174,197,198] Structures such as coaxial probes that incorporate a metal core or probes in which the aluminum coating is milled to produce isolated metal strips running down the sides of the taper would both support propagating modes irrespective of the probe diameter.[174,197,198] This may lead to new methods for increasing both the throughput and resolution of present day NSOM tips. The drawbacks of FIB are, of course, the added cost and availability of the equipment needed and the extra time and failure rate associated with fabricating the tips. There is also a more subtle compromise that arises when using the milled aperture probes. The quality and resolution of the force images collected in NSOM are largely a function of the aluminum grains at the aperture which act as a stylus. Because the FIB milled tips are so pristine and free of grains at the end of the probe, the force imaging characteristics are diminished. For NSOM applications relying on the simultaneous collection of high-resolution topographical information, this may become restrictive.

## II.C. Alternative NSOM Probe Designs

There are several limitations with the standard fiber optic probe that have motivated a great deal of work in developing alternative probe designs. Perhaps the greatest impetus for this research is to increase the spatial resolution possible with NSOM and move the technique firmly into the nanometer regime. Currently, confinement of light within the fiber optic probe limits the fundamental maximal resolution to approximately 12 nm.[4,5] However, with very few convincing exceptions, the practical resolution limit in most NSOM studies is usually no better than approximately 50 nm. This arises mainly from the inverse sixth power dependence in the output power with tip radius, which makes it very difficult to work near the resolution limit.[26,199] In response to this, several novel alternative probe ideas have been discussed and, in some cases, demonstrated to circumvent the use of fiber optic tips.

Perhaps one of the most promising avenues for dramatically improving the spatial resolution in near-field microscopy is through the use of so-called apertureless probes.[200−207] Illumination of the end of a sharpened metal tip can create oscillating surface charges which lead to a greatly enhanced field laterally confined to the tip apex. Simulations have probed the field enhancement under various experimental conditions and proposed new ways of more efficiently enhancing the field by modifying the excitation mode.[202,205] Particle trapping schemes have also been suggested on the basis of the strong forces generated by the fields near the tip.[204] When the apertureless probe is used for imaging, spatial resolution down to the nanometer scale has been reported.[206]

Some of the more exotic tip designs incorporate energy transfer schemes for funneling excitation down to a small point.[8,20,208−210] One incarnation that illustrates the principles of this idea involves the loading of small amounts of a luminescent material into the very end of a pulled capillary. Excitation of the material leads to excitons which can diffuse to the end of the tip where they radiatively decay producing a tiny light source. Several challenges will have to be overcome, however, before these tips provide a reasonable alternative to fiber optic probes. For instance, photobleaching of the luminescent material will impact the useful lifetime of the probes and methods to fabricate and control the tip geometry will need further development.

An idea related to the exciton probe involves taking advantage of the nanometer distance dependence of Förster energy transfer between donor and acceptor molecules.[8,20,211−213] In this scheme, a donor (or acceptor) dye of a fluorescence resonance energy transfer (FRET) dye pair is introduced into the sample and the acceptor (or donor) dye is attached to the imaging tip.[213] As the tip approaches the sample, the excited donor molecules can transfer their energy to the acceptor dye attached to the tip, leading to a new red-shifted fluorescence signal. This technique has recently been demonstrated with subdiffraction spatial resolution.[213]

The experimental arrangement for near-field FRET is shown schematically in Figure 6, where a lipid monolayer containing the acceptor dye is attached to a tapered fiber probe and the donor dye is incorporated in the bottom and top layers of a multilayer film. Figure 6 shows fluorescence images of the same region of the multilayer film monitoring the donor emission (left image) and acceptor emission (right image).[213] The decrease in intensity of some features and the sharpening of the resolution in acceptor emission image are both evidence that energy transfer from the top layer of the film to the tip is occurring.

With further development, this technique may be capable of overcoming several limitations currently encountered with the fiber optic NSOM probes. Since the technique does not depend on funneling light down to a small point, tips such as those used in AFM could be modified for this scheme by attaching the appropriate dye to the tip.[8,20,211−213] This, in principle, could lead to very high spatial resolution. Fiber optic NSOM probes are also problematic for imaging soft samples due to their high spring constants. Using the FRET scheme combined with standard AFM probes, it should be easier to control these parameters and expand the application of NSOM into areas involving fragile samples. For instance, AFM has been very successfully at imaging soft biological samples such as living cells, which has yet to be demonstrated with NSOM. As with the exciton tips, however, photobleaching may limit the convenience of this technique. Developments in photoemissive solid state materials that are more photochemically stable, however, may help alleviate some of these problems associated with near-field FRET imaging and exciton tips.

Other proposed tip designs make use of standard silicon nitride AFM tips to convert the nonpropagating fields in the near-field into measurable propagat-

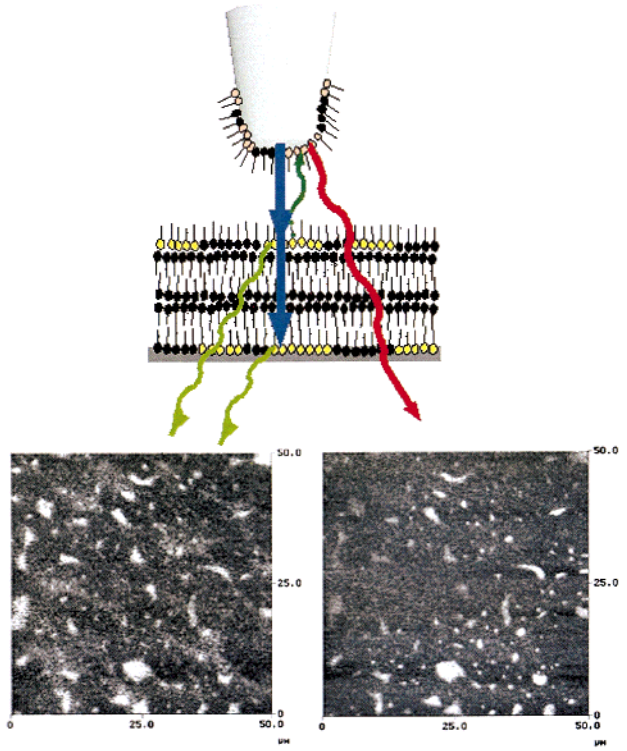


**Figure 6.** Schematic of the FRET scheme used to image a multilayer lipid film. A lipid monolayer containing the acceptor dye (rhodamine) of a FRET pair is attached to an uncoated tapered fiber. The donor dye (fluorescein) is dispersed in the upper and lower monolayers of a multilayer film. Light exiting the tip is resonant with the donor but does not excite the acceptor on the tip. As the tip nears the surface, energy transfer from the excited donor to the acceptor leads to a new red-shifted emission from the dye on the tip. Below left shows a fluorescence image of the film taken by monitoring the emission from the donor. Below right shows the same area of the film taken while monitoring the emission from the acceptor attached to the tip. The strong distance dependence of the FRET process leads to a decreased sensitivity to donor dye located in the bottom layer of the film and a sharpening of the resolution. Both of these effects can be seen when comparing the two images. Reproduced with permission from ref 213. Copyright 1999 Biophysical Society.

ing ones in a photon tunneling configuration.[214−220] Micromachined silicon nitride and silicon cantilevers have also been suggested along with related cantilever designs that are more active in that they integrate excitation and/or detection devices.[214,221−226] Finally, the scanning of optically trapped metallic spheres and lasing microparticles over a surface is also being investigated for possible applications in near-field microscopy.[227−229] While technically formidable, scanning an optically trapped source over a sample could reduce the forces involved in imaging, which is one of the barriers currently limiting the application of NSOM in the biological sciences.

## II.D. Shear-Force Tip Feedback

To obtain high-resolution optical images with NSOM, the tip must be positioned and held within nanometers of the sample surface during scanning. Various feedback mechanisms based on electron tunneling, photon tunneling, impedance, and reflection measurements have been introduced to accomplish this precise positioning.[35,37,78,230−235] One of the most widely adopted is the shear-force technique introduced independently by two groups in 1992.[236,237]

In the shear-force method, the NSOM tip is dithered laterally at one of its mechanical resonances.[1−3,10,66,128,133,137,141−144,149,150,230,236−256] The amplitude of the vibration is kept low, usually <10 nm, to avoid diminishing the resolution in the optical image. As the tip approaches the sample surface, shear forces acting between the tip and the sample dampen the amplitude of the tip vibration. This drop in amplitude normally occurs over a range of tens of nanometers from the sample surface. The amplitude can be monitored by several methods and used to generate a feedback signal to control the tip−sample gap during imaging.

The origins of the shear forces responsible for dampening the tip amplitude upon sample approach are still somewhat controversial.[143,242,244−246,248,250,252−254,257,258] Measurements of tunneling current between the tip and sample during shear-force approach seem to indicate that the tip does mechanically touch the surface at the onset of the amplitude dampening.[143] This would agree with recent experimental results obtained in a vacuum and at liquid-helium temperatures by Gregor et al.[244] This study used measurements of the frequency profile during approach and approach curves as a function of the tilt angle between the tip and sample to probe the forces acting on the tip. There are two factors that can lead to a drop in amplitude of the tip resonance—a shift in the peak resonance and/or a decrease in the quality factor, $Q$. The quality factor is given by the peak frequency divided by the width of the resonance at half of its maximum value ($Q = f_{peak}/f_{fwhm}$). Dissipative frictional forces, which are proportional to the velocity, decrease $Q$, while spatially varying forces shift the peak resonance. Gregor et al. observed an upward shift in the peak resonance frequency on approach toward the surface which was accompanied by the appearance of asymmetries in the resonance profiles.[244] These observations are consistent with a spatially varying force in the dither direction and indicate that, under these conditions, the dominant source of tip dampening arises from a nonlinear bending force associated with contact between one side of the NSOM tip and the sample surface.

These measurements, however, were taken on samples under conditions in which the surfaces are free from surface contaminants. For samples under ambient conditions, a contamination layer of water or other substances is commonly found on the sample surface which can lead to the addition of a viscous damping of the tip amplitude. This is reflected in a decrease in the tip $Q$ factor and acts over a longer range than the short-range, mechanical contact force discussed previously. For samples in air, numerous studies have found evidence of these dissipative forces. Typically, both the peak resonance and the $Q$ are found to change upon approach to the surface.

Most of the early implementations of the shear-force technique monitored the vibration amplitude of the tip using optical methods.[10,236,237] This can be

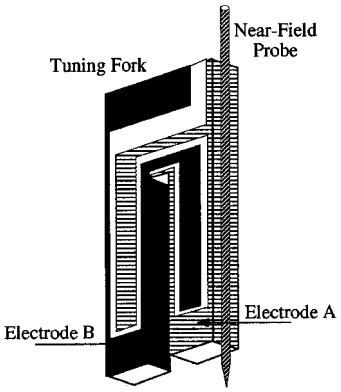


**Figure 7.** Schematic of the tuning fork method used for shear-force tip feedback. The NSOM tip is rigidly attached to one arm of the tuning fork, and the two electrodes provide the pickup for the piezoelectric signal. Reproduced with permission from ref 28.

accomplished using interferometric techniques, by monitoring the specular reflection of a probe beam focused at the tip/sample intersection, or by shadowing a beam across the tip shaft. These techniques have been very successful at mapping surface topography and have also worked well in aqueous environments.[137,144,150]

In the last several years, a tuning-fork technique for shear-force detection has been introduced and is finding widespread application.[1,3,241,248,249,254,259] As shown in Figure 7, an NSOM tip is attached to a commercially available quartz crystal tuning fork that has a well-defined resonance frequency (commonly 32.768 kHz).[28] The tuning fork resonance, which oscillates the NSOM probe, can be driven directly or by a ceramic piezoelectric tube or bimorph in which it is rigidly held.[1,3,241,248,249,254,259] At resonance, the motion of the two prongs of the tuning fork is maximal and generates a piezoelectric potential that can be monitored from contacts integrated into each arm of the fork. In analogy to the optical detection schemes, small changes in the oscillating signal can be detected using phase sensitive detection referenced to the drive signal. When the tip approaches the sample, a drop in the tuning fork vibration amplitude occurs which can be used in a feedback loop for regulating the tip−sample separation.

The tuning fork method has several advantages over the optical detection schemes which accounts for its current popularity. Since it is not based on optical detection of the dither motion, problems associated with stray light interfering with the detection of the NSOM signal are removed. It is also very compact and easy to implement and does not require the separate laser source and focusing elements as in the optical methods. The compact and self-aligning nature (i.e. not requiring the separate alignment of a detection system as in the optical methods) of the tuning fork technique makes it much more amenable for studies in extreme environments such as those encountered when working at low temperatures or in a vacuum, where remote operation is necessary.

The tuning fork resonances are characterized by well-defined resonant frequencies and extremely high $Q$. Typically, tuning forks with resonant frequencies at 32.768 kHz have $Q$ factors ranging from approximately 64 000 in a vacuum to 7500 in air. Depending on the characteristics and geometry of the attached NSOM tip, the combined tip/tuning fork $Q$ drops down to between several hundred to several thousand.[241,248,249,254,259] This raises two issues that are sometimes at odds with one another when using these high-$Q$ devices in a feedback loop.

The first issue involving the high-$Q$ oscillator revolves around the forces imparted to the sample during imaging. For soft or fragile samples, a reduction in the forces between the NSOM tip and sample is desirable such that perturbation to the sample from the tip feedback is eliminated. At first, the large spring constant or compliance of the tuning fork, which is typically around 20 000 N/m, would seem to limit the use of tuning fork feedback to only the most rugged samples. However, the high $Q$ of the oscillator makes the effective compliance of the oscillating fork relatively small. This can be seen by the relation $k_{\text{eff}} = k/(Q\sqrt{3})$, where $k$ is the static compliance and $k_{\text{eff}}$ is the effective compliance when oscillated. This equation shows that the effective fork compliance is inversely related to the $Q$, which is usually quite high for these oscillators. The high $Q$ makes the system very sensitive to small drag forces which can be on the order of piconewtons.[241,259]

The tradeoff with the high $Q$ comes in the form of the settling time or response time of the transient amplitude. The response time of the feedback system is related to the $Q$ of the oscillator through the relation $\tau = 2Q\sqrt{3}/\omega_o$, where $\tau$ is the time constant and $\omega_o$ is the resonance frequency of the tuning fork with the NSOM tip attached.[241,249,259] For typical situations, this leads to time constants of tens of milliseconds which translates into a total settling time ($5\tau$) on the order of hundreds of milliseconds. This long settling time reduces the response time of the feedback system and, at first glance, the maximal scanning speed possible. In a vacuum the situation is further exacerbated by the increase in $Q$ that occurs without the damping by air.

As has been pointed out recently, however, the limitation in scan speed from the high $Q$ can be addressed using a closed-loop feedback system as shown in Figure 8.[249] In Figure 8, the tuning fork is driven at resonance by sampling the tuning fork output current, converting this to a voltage, and feeding this back into driving the fork. This positive feedback system consequently tracks small shifts in the combined tuning fork/NSOM tip resonance. These shifts are demodulated by inputting the tuning fork signal into a phase-locked loop that detects the phase differences between this signal and a separate reference signal. A $z$-piezo tube moves the tip vertically with respect to the sample surface until the frequency of the tuning fork/NSOM tip system matches that set at the reference signal. The frequency of the reference input can, therefore, be used to set the desired tip−sample gap.

Using this configuration, Atia and Davis tested the closed-loop frequency response of a tuning fork feedback system.[249] The experiments utilized a tuning fork with a $Q$ of 2100, corresponding to a settling

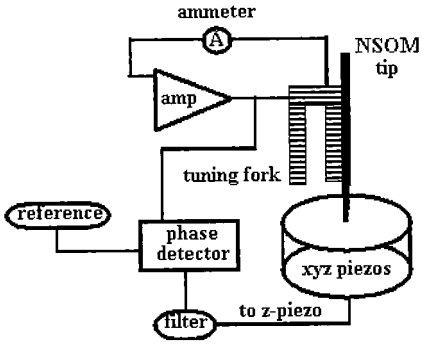


**Figure 8.** Schematic of the closed-loop feedback circuit used to increase the bandwidth in feedback for high-*Q* tuning forks. The oscillation signal from the tuning fork is sampled and fed back into the tuning fork to drive it at its resonance frequency. This signal, which automatically tracks shifts in the resonance frequency, is compared to a separate reference signal and demodulated in a phase detector. The frequency of the reference signal is used to set the tip−sample gap. The demodulated error signal is filtered and sent to the *z*-piezo. Adapted from ref 249. Copyright 1987 American Institute of Physics.

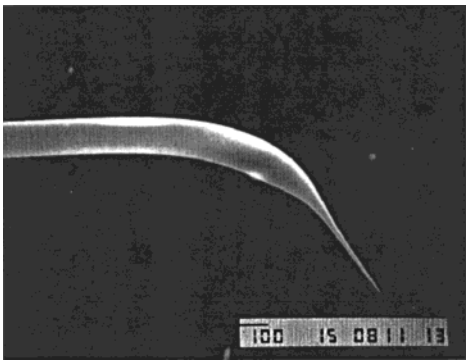

**Figure 9.** Magnified view of a bent NSOM probe used in tapping-mode feedback. Reproduced with permission from ref 263. Copyright 1995 American Institute of Physics.

time of $5\tau = 175$ ms and an amplitude response bandwidth of only 5.7 Hz. However, the experimentally determined bandwidth for the closed-loop feedback system was found to be 70 Hz, over 1 order of magnitude larger than the amplitude response. This is obviously much larger than expected using the amplitude response and shows that high-*Q* oscillators can still provide reasonable scan speeds.

## II.E. Tapping-Mode Tip Feedback

Tapping-mode feedback has also been utilized for tip−sample distance control in NSOM using standard fiber optic probes that incorporate a near 90° bend near the tip aperture.[22,65,106,147,154,155,260−267] A typical bent NSOM tip is shown in Figure 9.[263] With the bend, the probes can be oscillated vertically to the sample surface at their resonance frequency. As in tapping-mode AFM, the oscillation amplitude can be monitored optically by reflecting a laser off the bend in the tip and detecting the reflected light with a quadrant photodiode. Tapping-mode feedback has also been implemented using the nonoptical tuning-fork method and shares many of the advantages discussed above.[265] Several groups have used the bent tip probe combined with tapping-mode feedback in single molecule detection, under water applications, in studies on biological samples, and to correlate optical and height information from thin film samples.[22,52,65,72,103,105,106,108,109,119,129,131,146,147,154,155,261,263−278]

This method of tip feedback, like shear-force, has both strengths and weaknesses. Many of the strengths of this technique arise from the strong analogy that can be made between this method and tapping-mode feedback used in the more mature AFM field. Because of this, the tip−sample interactions are fairly well understood and many of the imaging modes developed for AFM can be incorporated into NSOM. The technique also works well in aqueous environments, and it is straightforward to reduce the forces in imaging by decreasing the spring constant of the tip.

Most of the drawbacks in the method result from changes in tip properties and the increased difficulty in tip fabrication, both of which arise from the inclusion of the bend near the tip end. For example, large bending losses occur at the bend which further reduces the throughput efficiency of the tips. This, however, can easily be compensated for by simply coupling more light into the probes. For polarized light measurements, lower extinction coefficients have been reported for bent probe designs compared with straight NSOM tips. When measured in the far-field, extinction ratios of approximately 70:1 have been reported for bent tips[266] and upward of 100:1 for conventional straight probes.[42,195,197]

It is important in tapping-mode feedback that the tip oscillation remains small when compared to the tip aperture to achieve high resolution. At high drive amplitudes, the oscillation amplitude is increased and resolution in the NSOM optical image is compromised. However, it has been shown that sufficiently small drive amplitudes are possible and resolution is not degraded in tapping-mode NSOM.[65] Another route to increase resolution is through synchronizing the collected NSOM signal to the tip oscillation. With this technique it is still possible to achieve high resolution at relatively large oscillation amplitudes. This was demonstrated by Chiba et. al. by imaging 20 nm thick chromium patterns on a quartz substrate.[108] In these experiments, the light coupled into the NSOM probe was modulated with an acousto-optic (AO) modulator placed in the light beam. A phase shifter connected to the AO modulator allowed complete control over the phase and duty cycle of the square wave irradiation with respect to the tip oscillation. The results demonstrated that the resolution in the optical image could be improved by adjusting the phase such that the sample was only irradiated when the tip was in closest approach to the sample.[108] This illustrates that even for large tip displacements, high-resolution NSOM optical contrast can be achieved by synchronizing the optical signal with the oscillation of the probe.

The use of metal-coated fiber optic probes introduced by Betzig and co-workers is ubiquitous in modern day NSOM, and the quality of the results is still largely governed by the quality of these tips. This could change in the future as new probe designs, such as apertureless probes, become more prevalent, but for now it is most important to understand the

particular properties of the metal coated fiber probes. To interpret NSOM results it is necessary to understand how these devices deliver light to subwavelength dimensions and to characterize the fields at the aperture.

The following discussion briefly explores the early diffraction theory treatments of light passing through small holes in perfectly conducting screens. Although these models offer greatly simplified views of an actual NSOM tip, the treatments yield surprisingly accurate results. This is followed by recent results using the multiple multipole (MMP) method to calculate the fields in and around more realistic NSOM probes. This semianalytical technique has been very successful in modeling the specific geometry of a tapered, metal-coated dielectric NSOM tip. The results provide insights into the propagation of radiation in the taper region and the nature of the fields emanating from the aperture. Pure numerical methods such as finite difference time domain (FDTD) calculations, other boundary matching calculations, and various forms of scattering theory have also been widely applied to model the fields in NSOM.[1−3,9,61,217,279−295] Generally, the results obtained among the various techniques are similar. The end of the next section, therefore, will highlight the MMP treatments which relay the important characteristics of light propagation through NSOM probes and are representative of results obtained with the various other treatments.

## *III. Theoretical Foundations of NSOM*

### III.A. Diffraction through a Small Hole

From a theoretical standpoint, the feasibility of Synge's idea was first confirmed in the work of Bethe who treated the passage of light through a subwavelength diameter hole formed in an infinitely thin, perfectly conductive screen.[296] This work, with corrections later introduced by Bouwkamp, were key in describing the fields near a small aperture and led to a surprisingly accurate picture of the radiation emerging from a near-field probe.[199,297,298] The general scheme applied is similar to that shown schematically in Figure 1, where radiation is incident on an infinitely thin, perfectly conducting screen incorporating a small hole of radius $a$. Before the work of Bethe, conventional diffraction methods mainly dealt with diffraction through holes large compared to the wavelength of the radiation ($a \gg \lambda$). These methods failed to accurately meet the boundary conditions at the aperture, namely that there should be no tangential component of the electric field on the screen. This deficiency, although small in the limit of large holes, becomes increasingly problematic as the hole diameter is decreased. Bethe overcame this limitation by satisfying Maxwell's equations and the boundary conditions with the introduction of fictitious magnetic surface charges and currents in the aperture region.[296] With these constructs in place, the tangential components of the electric field on the screen vanish (boundary condition satisfied) and diffraction through subwavelength holes can be treated.[199,296−298]

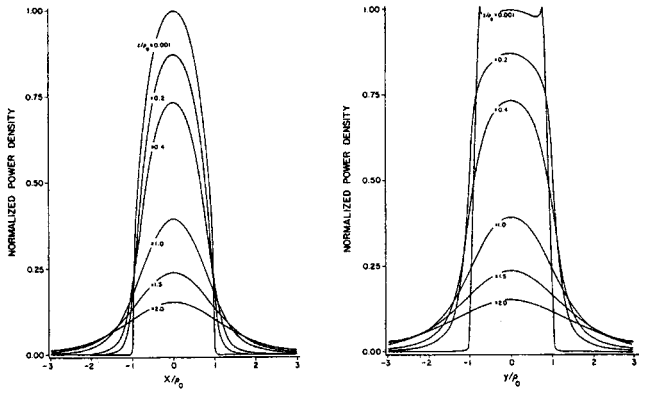


**Figure 10.** Plots of the time averaged Poynting vector as a function of distance away from a small aperture (radius $\rho_o = \lambda/150$) in a perfectly conducting, infinitely thin screen. The power density remains approximately collimated as a function of distance away from the aperture ($z/\rho_o$) up to distances equal to the aperture radius, $\rho_o$. Reproduced with permission from ref 299. Copyright 1986 American Institute of Physics.

In Bethe's original work the electric field in the aperture was not continuous due to an error in the magnetic current density expression. This error, which did not affect the calculated fields far from the aperture, leads to erroneous results near the aperture. Bouwkamp discovered and corrected this error, and the proper expressions for the field components in the near-field region just beyond the aperture, taken from his original paper, are shown:[298]

$$E_x = \mathrm{i}kz - 2ikau/\pi\{1 + v \arctan v + {}^1/_3(u^2 + v^2) + (x^2 - y^2)/3a^2(u^2 + v^2)(1 + v^2)^2\} \quad (2)$$

$$E_y = 4\mathrm{i}kxyu/3\pi a(u^2 + v^2)(1 + v^2)^2 \quad (3)$$

$$E_z = 4\mathrm{i}kxv/3\pi(u^2 + v^2)(1 + v^2) \quad (4)$$

Here $a$ is the aperture radius, $k$ is the wavenumber, and $x$, $y$, and $z$ are given in oblate-spheroidal coordinates $u$, $v$, and $\varphi$ through the relations

$$x = a[(1 - u^2)(1 + v^2)]^{1/2} \cos \varphi \quad (5)$$

$$y = a[(1 - u^2)(1 + v^2)]^{1/2} \sin \varphi \quad (6)$$

$$z = auv \quad (7)$$

With the proper expressions yielding consistent results for the fields both near and far from the aperture, insights into the fields emanating from a near-field aperture can be obtained.

The results from one such treatment by Leviatan using the method of moments are summarized in Figure 10.[299] The surfaces shown represent the normalized power density emerging from an aperture of radius $\rho_0 = \lambda/150$ as a function of the distance, $z/\rho_0$, away from the hole. In these calculations the incident radiation is polarized in the $x = 0$ plane and the resulting components in both the $x$ and $y$ planes are plotted in Figure 10a,b, respectively. Although calculations such as this assume perfect conductivity and disregard the finite thickness of the screen, many useful characteristics about the field distribution are

revealed. For example, Figure 10 shows that the light passing through the aperture remains collimated for a distance approximately equal to the radius of the aperture ($z/\rho_0 = 1$).[299] This important result shows that it is indeed possible to obtain subdiffraction limit resolution if a small aperture can be positioned and held within one aperture radius of the sample. The results shown in Figure 10 also reveal a substantial field enhancement near the edges of the hole in the screen for the *p*-polarized light. This edge effect arises from a divergence in the electric field at the infinitely sharp corner of the hole. This enhancement has also been observed in other more realistic models of the NSOM aperture which incorporate the finite conductivity of the metal cladding.

Calculations such as these are also useful in identifying potential problems for high-resolution NSOM measurements. For instance, when the ratio of the aperture radius to wavelength is less than 0.3 for a circular aperture, all modes in the near-field probe become evanescent. This leads to a significant tradeoff between resolution and throughput, with the output power decreasing as the inverse sixth power of the tip radius. This problem can be avoided using a slit as the near-field light source.[26,38] The slit geometry can always support a propagating mode and therefore has a much higher transmission coefficient. This, however, will only provide high resolution in one direction and has not been widely adopted. Light throughput, therefore, remains a formidable barrier toward achieving the ultimate resolution in aperture NSOM experiments and has motivated recent interest in alternative probe designs.

The work started with Bethe and Bouwkamp on the idealized perfectly conducting infinitely thin screen laid the foundation for subsequent theoretical treatments designed to more accurately describe the electromagnetic field distribution as applied to the specific geometry of the NSOM probe. This includes modifications that allow the perfectly conducting screen to have a finite thickness as any real NSOM probe must incorporate to be sufficiently opaque.[300−302] These modifications have shown that the light collimation length beyond the screen remains essentially unchanged compared to the infinitely thin screen model. All of these treatments, however, suffer in that they neglect the finite conductivity of the metal cladding used in real NSOM probes and provide little resemblance to the actual tip geometries utilized in experiments. Perhaps more importantly, the fields are calculated on isolated tips free from the influence of a nearby sample. As will be shown, the inclusion of a sample near the tip aperture can strongly influence the power transmission through the probe while the finite conductivity of the real metal coating can affect the resolution possible with a given NSOM tip. To provide a more complete picture of these effects, a number of numerical methods have been exploited.

## III.B. Multiple Multipole Method

In principle, modeling of near-field optics requires exact solutions of Maxwell's equations. Except in the most simple cases, however, analytical solutions are not available and approximate methods must be invoked. As mentioned earlier, several techniques have been widely adopted to model the fields for the specific geometry of the NSOM probe. One class of methods is based on matching boundary conditions at interfaces. The multiple multipole (MMP) method falls into this class and has provided a useful and powerful framework for exploring specific probe/sample geometries in NSOM. In particular, Novotny and co-workers have used this method to reveal a detailed microscopic view into the field distribution and radiation properties of realistic NSOM probes, positioned both far and near a sample surface.[21,24,88,173,174,303]

MMP is a semianalytical method that can accurately model the specific geometry of the tapered dielectric, finite conductivity of the metal cladding, and inclusion of a nearby sample in NSOM. In general, this approach requires dividing the space into domains. Inside each domain, the field is approximated by a series expansion

$$f^{(i)}(\mathbf{r}) \approx \sum a^{(i)}_j \cdot g_j(\mathbf{r}) \qquad (8)$$

using basis functions that are known analytical solutions of the Helmholtz equation $(\nabla^2 + k^2) f_{e,m}(\mathbf{r}) = 0$. In eq 8, $f^{(i)}$ are the scalar fields, $\mathbf{r}$ is the position vector, $g_j$ are the basis functions and $a^{(i)}_j$ are the unknown expansion coefficients to be determined. The basis functions, $g_j$, can be waveguide modes, plane waves, or evanescent waves. In the MMP technique, the basis functions are multipoles which are solutions to the Helmholtz equation in cylindrical (two-dimensional) or spherical (three-dimensional) coordinates.

Several origins along the boundaries between each domain are chosen for multipole expansions. The coefficients in eq 8 are determined by matching the expansions from adjacent domains at discrete points along the domain interface.[173] The multipole functions used as the basis set are short range and only significantly affect their immediate neighbors. This makes them useful in modeling complex localized structures such as that found in NSOM tip geometries. The MMP technique also reduces the computational time required over pure numerical methods, such as the finite difference time domain (FDTD) method,[47,304] since only the boundaries between domains need to be discretized. Thus, the MMP approach provides a flexible and efficient environment to explore geometries and conditions encountered experimentally in NSOM.

Using the MMP method, simulations of the fields in and around NSOM tips have been calculated using both 2-D and 3-D models of the probe.[24,88,173,174] The details of the probes used in the modeling vary but basically consist of a tapered glass core embedded in a cladding of aluminum, as shown in Figure 11.[173] In Figure 11, the tapered lines indicate the boundary between the glass core and the aluminum cladding of the probe and the horizontal line beneath the probe represents the glass sample surface. In these calculations, 488 nm light is launched into the probe at which wavelength the dielectric of the core and

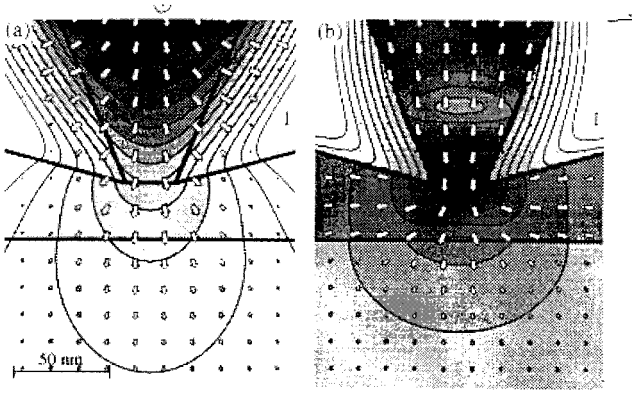


**Figure 11.** Results from 2-D MMP calculations of light propagation through a glass wedge surrounded by aluminum. The results are shown for the (a) *s* polarization (perpendicular to the plane of the figure) and the (b) *p* polarization (parallel to the plane of the figure). The direction and magnitude of the time-averaged Poynting vector are represented by the arrows and the gray scale contours map regions of constant $|E|^2$. Each contour line represents a factor of 2 change in $|E|^2$. Reproduced with permission from ref 173. Copyright 1994 Optical Society of America.

cladding are $\epsilon_{core} = 2.25$ and $\epsilon_{cladding} = -34.5 + 8.5i$, respectively.

Figure 11 shows the results for 2-D calculations of a NSOM probe near a glass surface for both *s* (electric field perpendicular to the plane of the figure) and *p* (electric field in the plane of the figure) polarizations.[173] Arrows represent the time-averaged Poynting vector which maps the flux of radiation in and around the tip. The length of the arrows represents the magnitude of the flux with the arrows shown for the *s* polarization increased by a factor of 17 compared to those shown for *p* polarization. The gray scale contours map regions of constant $|E|^2$ which is a measure of the local electric energy density and the quantity of interest for most NSOM applications. Each contour line represents a factor of 2 change in $|E|^2$.

For both polarizations, the calculations reveal complicated standing field patterns inside the taper region of the tip suggesting a fraction of the incident power is reflected back up the tip. The calculations also show the penetration of the radiation into the aluminum cladding of the tip as expected for a real metal with finite conductivity. The observed penetration depth is consistent with the skin depth for aluminum ($\approx$13 nm at 488 nm) and represents a considerable sink of radiation in the taper region. This leads to tip heating which, as mentioned earlier, has been measured experimentally by several groups.[175−178] Figure 11 also shows that the field near the aperture of the tip extends beyond the actual dimensions of the fiber aperture for both polarizations. This increases the effective size of the aperture by an amount dependent on the skin depth of the cladding.

The calculations show that the *s*-polarized component is more confined near the aperture than the *p* component, although the *p*-polarized field density is much stronger. For the *p*-polarized light, where the field is perpendicular to the boundary, large field enhancements are observed near the rim of the aperture as seen earlier in calculations carried out on holes in perfectly conducting, infinitely thin screens. Again, this arises from the quasi-divergence in the electric field caused by the sharp boundary at the tip aperture. For the *s* polarization, where the field is parallel to the boundary, the contours of constant $|E|^2$ vary smoothly across the tip aperture. As apparent from Figure 11, the *p*-polarized light propagates over a much wider angular range than the *s*-polarized component. For both polarizations, this angular spread becomes more pronounced as the tip−sample gap is decreased, sending more light into angles greater than the critical angle—the so-called forbidden zone. This forbidden light contains the highest spatial frequencies but is also most sensitive to tip−sample gap variations and topographical changes.[17,88,110,295,305] Imaging with forbidden light is therefore highly susceptible to artifacts introduced through the mixing of topographical and optical information, and the images are not easily interpreted without a thorough prior knowledge of the sample.

The more computationally demanding 3-D models of the NSOM probe have yielded similar results to the 2-D treatments.[174] The fields in the two planes of the 3-D model are similar to the fields calculated within the 2-D model, as well as the observed increase in output power when the tip is positioned close to a dielectric. The power output is a major concern in NSOM tip design and can be the limiting factor in many near-field studies. Moreover, output power, along with field confinement, is the major obstacle in realizing the ultimate resolution in NSOM. Unfortunately, calculations of output power do not paint a promising picture for the standard fiber optic probes. Calculations of the power within the taper region as a function of distance away from the aperture illustrates the magnitude of the problem. The transmission in a typical probe geometry goes from approximately $10^{-3}$ to $2 \times 10^{-12}$ as the diameter of the dielectric core is reduced from 100 to 20 nm.[174] Several authors have pointed out that it may be possible to fabricate metal structures on NSOM tips to build waveguides that have no cutoff and hence exhibit vastly improved transmission characteristics.[174,197,198] This has yet to be demonstrated for NSOM but may be becoming feasible given the increased reports of ion beam milling of tips.[194−196]

The results from Bethe−Bouwkamp calculations compare surprisingly well with the more rigorous MMP treatments of realistic probe geometries. Bethe−Bouwkamp results overestimate the degree of field confinement within the aperture and at the boundaries and tend to overestimate the field gradients, but the essence of the problem is captured remarkably well for such a simple model. In the presence of a substrate, however, the tip cannot be treated as an independent source and techniques such as MMP must be utilized to model the modified fields.

Figure 12 shows MMP calculations for a 2-D NSOM probe being scanned over a small metal particle.[24,173] The NSOM tip shown has a 30 nm

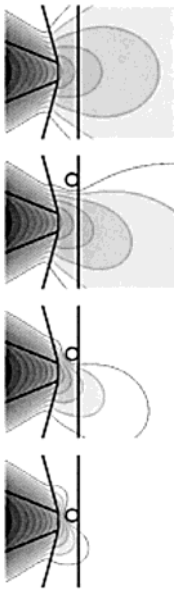

**Figure 12.** Results from 2-D MMP calculations for s polarized light as the NSOM tip is scanned over a small metallic sphere. The diameter of the NSOM tip is 30 nm, and the sphere is 20 nm in diameter. For these calculations, the tip was scanned across the sphere at a constant height of 33 nm above the substrate. Reproduced with permission from ref 16. Copyright 1995 International Society for Optical Engineering.

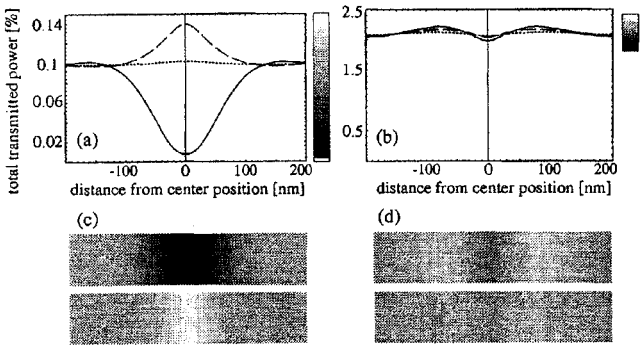


**Figure 13.** Calculated intensity profiles for the *s* and *p* polarization as the NSOM tip is scanned across small spheres of varying dielectric. The tip was scanned at a constant height of 33 nm from the surface, and the 20 nm sphere dielectric was varied from ideally conductive ($\epsilon = -\infty$, solid curves), to glass ($\epsilon = 2.25$, dotted curves), and to highly refractive ($\epsilon = 11.56$, dashed curves). Reproduced with permission from ref 173. Copyright 1994 Optical Society of America.

diameter and is being scanned at a constant distance of 33 nm above the substrate, upon which rests a 20 nm diameter sphere. For the particular series shown in Figure 12, *s* polarization is used and the sphere is metallic.[24] Evident from the figure, the fields near the aperture are heavily influenced by the presence of the metallic particle which tends to act like a mirror, reducing the radiation seen in the far-field. Figure 13 plots the total transmitted power for both *s* and *p* polarizations as a function of the lateral displacement of the metallic sphere under the tip (solid curves).[173] The metallic sphere is assumed to be ideally conducting with a dielectric constant of negative infinity.

Similar calculations, shown in Figure 13, were carried out for a glass sphere ($\epsilon_{glass} = 2.25$, dotted curves) and a highly refracting sphere ($\epsilon_{refracting} = 11.56$, dashed curves) located under the tip.[173] In contrast to the decrease in signal observed for the metallic sphere, as the tip passes over dielectric materials the field is attracted by the particle and the total transmitted power increases. The contrast observed in the far-field switches from negative contrast (loss in transmitted power) to positive contrast (gain in transmitted power) as the refractive index of the particle increases. The transition between contrast levels approximately follows the transition from metallic to dielectric sample properties and, in general, is most apparent in the *s* polarization.

The theoretical results are important for understanding and interpreting images collected under near-field illumination. This is particularly important since there can be a significant coupling between the optical and topographical information which has been a constant source of imaging artifacts in NSOM.[17,305,306] This susceptibility to coupling between the *z*-motion of the tip and the optical signal has led to many claims of high resolution that, more than likely, simply result from this coupling artifact. For this reason, a direct one-to-one correspondence between topography and optical features is often worrisome. Claims of high resolution are therefore usually held to the standard that they be uncorrelated with features in the force image. In the following applications, examples where chosen in which this artifact is clearly not the cause of high-resolution either because fluorescence contrast was utilized, which is less susceptible to this artifact, and/or there is a clear decoupling between the optical and topographical features.

## *IV. Applications in Single Molecule Studies*

### IV.A. Single Molecule Detection

Single molecule detection (SMD) and spectroscopy have long been the goals of spectroscopists. These capabilities have important implications from the fundamental studies of nonensemble behavior to applications in the analytical and biological sciences. Spectral interrogation of single molecules eliminates the averaging encountered in bulk samples. Thus, single molecule dynamics and spectroscopy opens fascinating possibilities for observing many fundamental molecular level processes that would otherwise be hidden in bulk studies. For the biological sciences, the ability to observe the fluorescence from a single protein or tagged protein offers exciting opportunities in structural and dynamic studies in vitro.

In 1993, Betzig and Chichester reported the detection of fluorescence from single molecules with NSOM.[39] The sample they probed consisted of carbocyanine dye ($diIC_{12}$) molecules spread across a thin coating of poly(methyl methacrylate) (PMMA) on a glass cover slip. These landmark results not only demonstrated the single molecule detection limits possible with NSOM but also discovered that orientation information about the transition dipole could also be determined.[39] This was soon followed by

several reports that utilized NSOM to measure the spectra[43,53,54,58] and fluorescence lifetimes[40−42,44,47,54] of individual chromophores.

NSOM detection of single molecules offers higher spatial resolution over far-field techniques and, in certain instances, an increase in the orientational information about the chromophore. Furthermore, the simultaneous force mapping of the surface topography inherent in NSOM can provide insight into the structural landscape surrounding the molecule under study. As in the far-field studies, NSOM measurements can be made under ambient conditions or even in aqueous surroundings. NSOM, however, is a two-dimensional technique in that the chromophore under study must be within a distance equal to the tip radius to obtain the high spatial resolution. This can be an advantage or disadvantage depending on the particular application but is completely complementary with the exquisite sectioning capabilities of confocal microscopy.

## IV.B. Single Molecule Fluorescence Lifetime Measurements

As mentioned, single molecule fluorescence lifetimes have been measured with NSOM by several groups and the results have revealed complications associated with using a metal-coated tip located near the sample.[40−42,44,47,54] The aluminum-coated tip can reduce the fluorescence signal from a single molecule and in some instances modify the measured fluorescence lifetime of the molecule. These complicated effects have been studied in detail, and coherent pictures of the mechanisms responsible have been elucidated.[47] As such, it is useful to review these studies briefly to help define the conditions under which NSOM measurements provide reliable results.

Early single molecule NSOM studies explored the effects of the nearby metal-coated tip on the photophysics of the molecule under study.[40−42,44,54] These studies have been quite useful in identifying potential pitfalls and uncovering the useful limits of the technique. The fluorescence count rate from a single molecule is sufficient to conduct both spectroscopic and time-resolved measurements. For the latter, characterization of the single molecule fluorescence lifetime as a function of tip-molecule position has been carried out by several groups.

Two independent NSOM studies on the fluorescence lifetimes of single molecules as a function of the tip−molecule lateral displacement first appeared in 1994.[42,44] These studies each showed that the fluorescence lifetime is indeed perturbed by the nearby aluminum-coated NSOM tip. In these studies, ultrashort light pulses were coupled through the near-field probe and time-correlated single photon counting was used to build up a histogram of the fluorescence lifetime of the molecule.

In one study, Xie and Dunn dispersed sulforhodamine 101 molecules on a glass substrate and imaged them using an arrangement that allowed for the simultaneous collection of the fluorescence lifetimes.[42] With a NSOM tip−sample gap of 7 nm, a series of images consisting of 64 frames spanning 6.6 ns in time was collected on a 2 $\mu$m × 2 $\mu$m (128 × 128 pixels) field of molecules. Single molecule lifetimes were extracted from the movie by selecting a single $x-y$ coordinate from each time frame. This allowed for a detailed comparison of the measured fluorescence lifetimes as a function of tip−molecule lateral displacement. A plot of fluorescence lifetime versus displacement revealed more than a factor of 2 decrease in lifetimes as the tip was offset from the centered position as shown in Figure 14.[42] Similar phenomena were observed by Ambrose et al. for rhodamine 6G.[44] Here too, the fluorescence lifetimes were highly dependent on the position of the NSOM tip over the molecule and decreased as the tip was offset from the centered position. This study also showed that the fluorescence lifetime is not dependent on excitation power or heating from the NSOM tip.

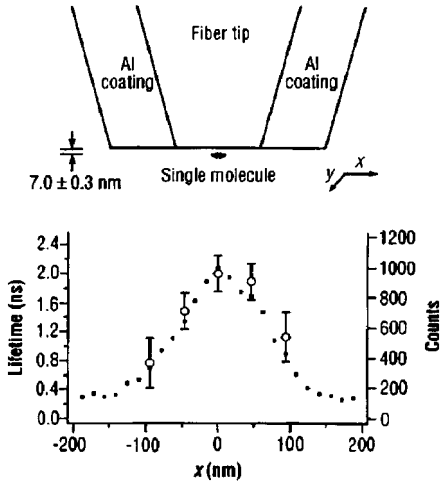


**Figure 14.** Idealized schematic of a single molecule located beneath an aluminum-coated fiber tip. Below is plotted the observed intensity across a single molecule and the associated measured fluorescence lifetime. As the tip is offset with respect to the molecule, the fluorescence lifetime decreases from interactions with the nearby aluminum coating. Reproduced with permission from ref 42. Copyright 1994 American Association for the Advancement of Science.

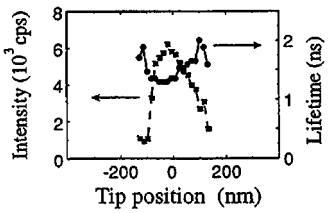


**Figure 15.** Intensity and lifetime measurements made across a single molecule in which a reversal in the lifetime behavior as compared with Figure 14 is observed. Reproduced with permission from ref 54. Copyright 1996 Elsevier Science.

Interestingly, Trautman and Macklin reported time-resolved NSOM measurements that found an opposite trend in the lifetimes.[54] For diI molecules dispersed on a PMMA film, they found that for certain near-field tips the fluorescence lifetimes actually increased as the tip was offset with respect to the molecule as shown in Figure 15.[54] Although highly tip dependent, they routinely found that some lifetimes were longest with the tip laterally displaced from the center of the molecule and shortest when

the tip was directly centered above a molecule. Qualitatively, all of these results can be understood in terms of the distance dependence of radiative and nonradiative perturbations to the lifetime introduced by a nearby metal surface.[307] Therefore, it is possible to measure both decreases and increases in the fluorescence lifetime depending on the actual distance between the metal-coated NSOM tip and the molecule.

Among other contributions, the above results reflect the ambiguity in precisely determining the distance between the near-field tip and the molecule under study. This ambiguity results from the difficulty in obtaining smooth aluminum coatings on the nanometric scale, which introduces uncertainty in the actual tip−molecule gap.[165,171,172] However, the distance between the fluorophore and a metal surface (NSOM tip) affects the observed fluorescence lifetime.[307] A theoretical description of these processes for the specific geometry of an idealized near-field probe (2-dimensional) has recently appeared.[47]

By the numerical solution of Maxwell's equations using the finite-difference time-domain (FDTD) approach, calculations for the specific geometry of the NSOM experiments were carried out.[47] The results confirm the reversal in lifetime behavior seen in experiments as a function of tip lateral displacement. The calculations indicate that this reversal arises from variations in the tip−molecule gap which alters the balance between competing radiative and nonradiative mechanisms. These results are in good qualitative agreement with the experimental data and provide guidance for minimizing the effects of the metal coated NSOM probe on lifetime measurements.[40−42,44,47,54] With the NSOM tip directly centered above the fluorophore, intrinsically fast dynamic processes occurring on the subnanosecond time scale can be measured essentially free from tip induced perturbations.

## IV.C. Single Molecule Spectroscopy

As mentioned earlier, the fluorescence count rate from a single molecule is sufficient to carry out spectroscopic measurements as well as time-resolved experiments.[43,53,54,58] Trautman et al. reported the fluorescence spectra of single diI molecules at a polymer interface using NSOM in 1994.[43] The room-temperature spectra were collected by dispersing the fluorescence onto a cooled CCD camera that was coupled to the near-field microscope. The individual fluorescence spectra revealed a distribution in peak locations, widths, and, in some cases, a time dependence in these properties. In general, the single molecule emission spectra reported were narrowed compared to the bulk spectrum. This reflects the reduction in the inhomogeneous line width caused by the distribution in molecule environments encountered in the bulk experiments.

In light of the above discussion on time-resolved NSOM measurements, it is important to ensure that the spectral measurements are free from complications arising from tip perturbations. The following observations suggests that these measurements are free from complications arising from tip perturbations: (1) the individual single molecule near-field spectra can be summed to reproduce the bulk spectrum; (2) the photochemical stability is consistent with far-field results; (3) the broadened spectra and the frequency of the spectral jumps show no dependence on laser power or tip feedback conditions.[43] A fourth line of evidence comes from the FDTD calculations mentioned earlier which indicate that perturbations to the single molecule spectrum induced by the nearby aluminum coating should be negligible at room temperature.[48]

Satisfied that the observed spectral characteristics are not perturbed by the NSOM tip, what molecular level information do they reveal? As mentioned previously, the individual spectra show a distribution in both peak location and width. These results were cast in terms of a model in which the molecules occupy unique environments which influence their specific spectral characteristics. Many of the molecules also exhibited an evolution in both their peak location and width as a function of time. This was attributed to a distribution in barrier heights associated with rearrangement in the particular microenvironment.[43] This work was later extended to simultaneous measurements of both the emission spectrum and lifetime of single diI molecules using both near-field and far-field approaches.[54] The results are important because they show that spectral measurements at the single molecule level are possible with NSOM and that they can reveal new insights into sample properties.

The perturbations caused by the metal coating continue to be thoroughly investigated, and the results indicate that the mechanisms are understandable and, in some cases, avoidable. For instance, experimental and theoretical results discussed here indicate that perturbations to the room-temperature spectra are minimal. This, however, may not be the case for low-temperature NSOM studies where the individual spectra are narrowed. For time-resolved studies, tip-induced changes in the fluorescence lifetime have been observed by several groups. The measured fluorescence lifetimes can both decrease and increase depending on the tip−sample gap in agreement with FDTD calculations. These effects can be reduced or eliminated if the fluorescence lifetime is fast when compared to the quenching rate. The use of NSOM in some single molecule applications, therefore, requires a cautious and thorough understanding of the possible tip effects when extracting information from the data.

## IV.D. Single Molecule Diffusion at Interfaces

Today, most of the studies on single molecule photophysics where the concentration or, more precisely, the density of molecules can be controlled are carried out using far-field techniques to avoid the complications listed above.[308] Far-field methods are noninvasive, the data usually have higher signal-to-noise, and in most cases the results are generally easier to interpret. Therefore, for many single molecule studies where spatial resolution is not a factor, far-field methods predominate. However, for situations where spatial resolution is a factor, single molecule studies with NSOM remain unequaled.

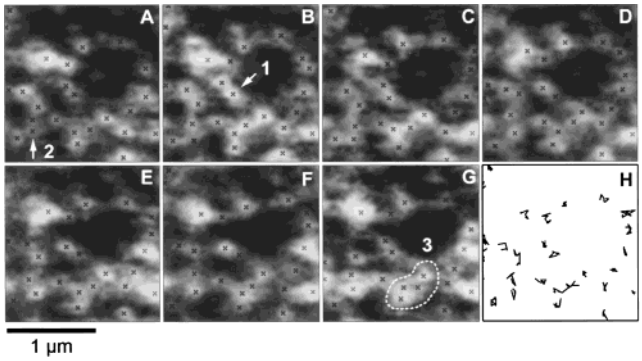


**Figure 16.** Consecutive NSOM fluorescence images of a field of single molecules in which some are observed to laterally diffuse. Successive frames were collected at 13 min intervals, and the trajectories of the diffusing molecules are shown in panel H. Reproduced with permission from ref 59. Copyright 1996 Elsevier Science.

The high spatial resolution of NSOM was combined with its single molecule detection limits to directly measure the diffusion of rhodamine-6G (R-6G) dye molecules in a thin film of polyvinylbutyral (PVB).[59,63] A 25 nm thick polymer film doped with dye molecules was sequentially imaged at the submicrometer level with fluorescence NSOM. The sequential NSOM fluorescence images revealed that some of the molecules in the film were not stationary and laterally diffused on the time scale of minutes. Figure 16 shows a series of 7 NSOM fluorescence images (A−G) of a field of single molecules.[59] The time interval for each frame is 13 min, and the trajectories for the molecules found to diffuse are shown in Figure 16H. The molecular diffusion was not uniform in the field of view with some molecules experiencing isotropic motion, others highly directional motion, and some no motion at all on the time scale of the experiment. The high directionality of some of the molecules, it was suggested, may reflect tubular structures in the polymer host which confines the local diffusion to quasi-one-dimension.

In all, the trajectories of 97 molecules were collected and analyzed.[59] Plots of the *x* and *y* components of all the trajectories collected in a 4 $\mu$m × 4 $\mu$m area resulted in an isotropic distribution, despite the highly anisotropic motion of some of the molecules. Analysis of the mean square displacement (MSD) suggested a random walk process with an average diffusion constant of $2.6 \times 10^{-15}$ cm$^2$/s. This value compares favorably with bulk measurements in similar systems.

The statistical treatment of the data also uncovered interesting behavior tied to the unique properties of the fields emerging from the near-field aperture. The plot of MSD versus time contained a component at zero time which normally suggests confinement in a restricted area.[59,63] However, the authors suggest a more likely model in which the inhomogeneous field distribution at the near-field of the aperture combined with the reorientation dynamics of the dye molecule can lead to apparent shifts in molecule position.[59] Simulations carried out under realistic probe-sample geometries revealed spatial variations in the observed single molecule fluorescence that are coupled to reorientations of the transition dipole

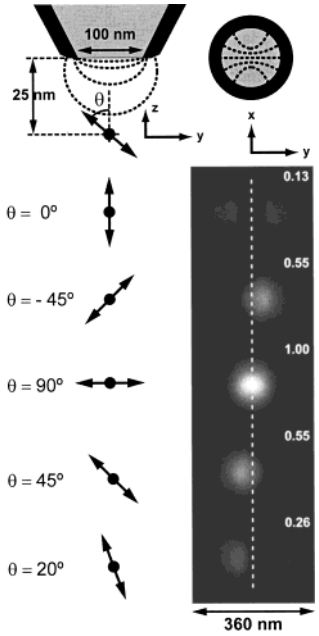


**Figure 17.** Calculations showing how rotations of the transition dipole of the single molecule can manifest itself as apparent lateral displacements of the molecule. Reproduced with permission from ref 59. Copyright 1996 Elsevier Science.

moment angle with respect to the NSOM tip. This can be seen in Figure 17, which displays the excitation efficiency for dye molecules of varying orientation located beneath a near-field probe.[59] As the results show, an ambiguity in the location of the chromophore is introduced by variations in the transition moment of the molecule with respect to the probe.

Single molecule diffusion experiments were also carried out by van Hulst[62,66,67,134] and co-workers on single molecules of R-6G on a glass substrate and carbocyanine (diIC$_{18}$) molecules in/on poly(methyl methacrylate) (PMMA) thin films.[62] For the R-6G molecules dispersed on the glass surface, repeated NSOM fluorescence imaging of the same region revealed a lateral diffusion of some of the molecules on the surface. The origin of the diffusion was ascribed to a thermal process, and analysis of the single molecule trajectories yielded a diffusion constant of $(6.7 \pm 4.5) \times 10^{-15}$ cm$^2$/s.[62]

To further characterize the single molecule dynamics, polarization measurements were used to study the rotational freedom of DiI molecules in and on a thin PMMA film. Following excitation in the near-field with polarized light, the perpendicular components of the fluorescence were separated with a polarizing beam splitter and sent to two avalanche photodiode detectors. In this way, the 0 and 90° fluorescence polarizations could be simultaneously monitored while imaging. These data was then color coded and overlaid to produce one data set with red features corresponding to fluorescence detected at the 0° detector and green corresponding to the 90° detector. In the combined images, therefore, fluorescence features equally dispersed on both detectors appear yellow.

Using this scheme, sequential images of a 1.5 $\mu$m × 1.5 $\mu$m region of the DiI/PMMA film were

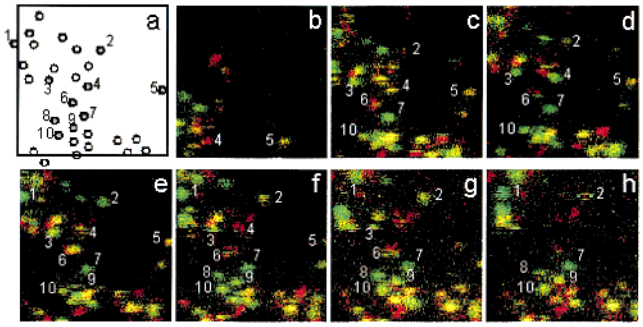


**Figure 18.** Consecutive 1.5 $\mu$m × 1.5 $\mu$m NSOM fluorescence images of DiI molecules on PMMA. The polarized fluorescence was detected by monitoring each of the two perpendicular components. The two images were then recombined using a color coding scheme to create one image that contains the orientation of the chromophores. Fluorescence from single molecules detected at 0° is coded red and 90° is coded green with fluorescence equally distributed between the two detectors giving yellow features. The images were collected sequentially at 10 min intervals. Analysis of the images reveals the rotational diffusion of some molecules. Reproduced with permission from ref 62. Copyright 1997 American Chemical Society.

measured and analyzed to gain insight into the rotational diffusion of the DiI molecules. Figure 18b−h displays 7 sequential frames taken at 10 min intervals. Figure 18a maps the locations of the molecules and identifies molecules by number that remain stationary (3, 5, 7, 10), suddenly appear/disappear or blink (1, 2, 8, 9) and/or rotate (2, 4, 6).[62] Several molecules remained stationary both laterally and rotationally during the course of the experiment (≈1 h) or until they are lost to photobleaching. Others, however, were found to be rotationally active, the time scales of which varied from fast events which occurred within the individual scan lines (2.5 s/line) to longer events in which the dipole slowly rotated between frames (10 min/frame). Further measurements of the 0 and 90° fluorescence components of the single molecule emission were used to characterize the relative orientation between the absorption and emission dipole of DiI.[62] These measurements found strong evidence that the two dipoles lie roughly parallel to each other, in agreement with previous work.

## IV.E. Single Molecule FRET Measurements

The aforementioned examples demonstrate how the high resolution and single molecule detection limits of NSOM can be used to reveal processes beyond the resolution limit of conventional optical techniques. A final single molecule example will be discussed in this section which may hold tremendous promise for future studies in the biological sciences. This report by Weiss and co-workers demonstrated the capabilities of NSOM for probing the energy transfer between a single donor and a single acceptor molecule.[53,58] Energy transfer measurements are becoming increasingly important given their sensitivity to molecular distances. Single molecule energy transfer measurements combined with NSOM may provide a powerful new technique for probing a variety of biological processes.

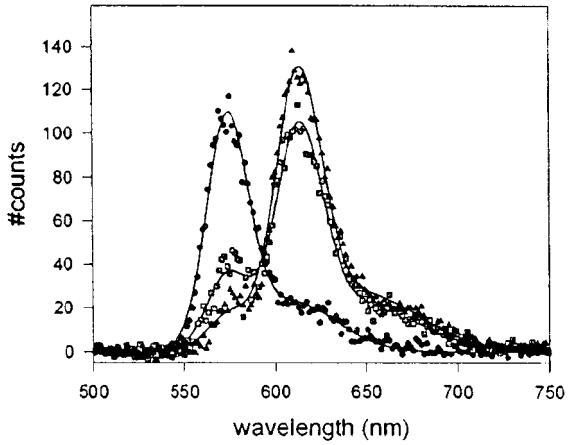


**Figure 19.** Spectra of a single FRET pair of tetramethylrhodamine isothiocyanate and Texas Red attached to the ends of a DNA strand 20 bases long. Energy transfer from a single dye donor to the single dye acceptor is evidenced by the evolution in the spectra shown for the 39th (black triangles), 40th (gray squares), and 41st (black circles) scans. Upon photobleaching of the acceptor, a large increase in the donor emission is observed. Reproduced with permission from ref 53. Copyright 1996 National Academy Press.

The fluorescence resonance energy transfer (FRET) study used DNA-linked donor and acceptor pairs of tetramethylrhodamine isothiocyanate (TMR) and Texas Red (TR), respectively.[53,58] The dyes were attached to the 5′ ends of complementary DNA strands of either 10 or 20 bases in length. The DNA was deposited onto aminopropylsilanized treated coverslips, washed, and dried. Two-color NSOM fluorescence images of the coverslip were used to identify the locations of the two individual chromophores and find regions containing both chromophores which yields information on the degree of DNA hybridization.

To unambiguously assess whether FRET was taking place between the tethered chromophores, NSOM fluorescence spectra were collected as a function of time.[53,58] One signature of energy transfer between a single molecule FRET pair would include an enhanced emission of the acceptor and a quenched emission from the donor and a significant increase in the donor emission upon acceptor photobleaching. The latter relies on there being little acceptor absorption following photobleaching. In this study, a prompt increase in donor emission following acceptor photobleaching in four different TMR-20-TR DNA strands on glass was observed. Figure 19 displays the results from one such pair where the black triangles, gray squares, and filled circles represent the spectra at the 39th, 40th, and 41st scans, respectively.[53] Upon acceptor photobleaching, a large increase in the previously quenched donor emission spectra is observed. These and similar results, which demonstrate FRET between single chromophores, exhibited energy transfer efficiencies ranging from 16 to 85%. This range in efficiencies reflects variations in distance, orientation, spectral overlap, and quantum yields of the particular single molecule dye pairs. Variances in properties such as the spectral overlap are unique issues that arise in nonensemble mea-

surements such as these where individual molecules can exhibit slightly different spectral profiles.

These technically challenging measurements offer exciting possibilities for probing biological systems at the nanometric level. Conformational motions, specific protein interactions, and other dynamical processes in cells should be accessible to FRET measurements with NSOM. Moreover, when these are combined with the force imaging capabilities of NSOM, new insights into structure−function relationships should be forthcoming. Bulk dynamic measurements with FRET require that all molecules move in unison such that the dynamic information does not simply average out in the FRET signal. For single molecule measurements, such as the FRET measurements discussed here, this requirement is removed and single trajectories can be measured.[53,58] This powerful difference may open vast opportunities in areas such as measuring protein conformational dynamics without the need for a kinetic trigger. Contributions arising from quenching by the NSOM probe or the subtleties introduced by the nonensemble properties of single chromophores, however, will need to be understood before all the information can be extracted from these measurements. Progress in these areas continues, and it seems unlikely that this will be the limiting step for the future of such measurements.

Having discussed various NSOM applications in single molecule fluorescence detection, it is useful to explore how measurements made with near-field optics compare with similar measurements made using conventional far-field techniques. Both near-field and far-field techniques are capable of room-temperature measurements and offer flexible working conditions, such as in aqueous environments. Near-field optics offer improved spatial resolution, limited only by the size of the particular tip aperture, while the spatial resolution in confocal microscopy is limited to approximately $\lambda/2$ by diffraction effects. For low-temperature applications, where conventional objective lens systems become problematic, NSOM has a tremendous advantage in spatial resolution but may become problematic in spectral measurements due to the effects of the metal-coated tip.

It is now generally accepted that far-field techniques are superior for studying the unique photophysical properties of single molecules in samples where coverage can be controlled.[308] In these applications, spatial resolution is not critical and far-field techniques offer enhanced signal-to-noise, speed of data acquisition, and avoid perturbations to the observables that the NSOM tip can produce. It should be noted, however, that recent improvements in NSOM tip design, most notably through focused ion beam (FIB) milling of the aperture, have dramatically improved the performance of NSOM in many of these figures of merit and have decreased the gap between far-field and near-field techniques for single molecule studies.[195] Regardless, near-field microscopy offers unique opportunities for determining the orientation of a chromophore and is essentially nonperturbative except in time-resolved applications where the tip effects are understood and somewhat controllable. NSOM also has the powerful capabilities of simultaneously mapping the surface topography. Therefore, the question of whether far-field or near-field techniques are most appropriate largely depends on the particular application. If anything, these techniques are complementary and offer exciting possibilities when used together.

## *V. Applications in Thin Film Analysis*

The various optical contrast mechanisms such as emission, absorption, and transmission, combined with associated polarization and spectroscopic techniques, provide a rich set of tools to probe sample properties at the mesoscopic scale. Recent NSOM studies on a variety of aggregates and small-molecule systems illustrate this flexibility in imaging contrast modes as well as the wealth of chemical information that results (see refs 11, 12, 21, 28, 63, 65, 68−85, 88, 90, 93, 94, 97−103, 105−110, 113, 116−119, 167, 213, 232, 256, 267, 270, 277, 278, 309−319).

### V.A. Light-Emitting Polymers

Electroluminescent thin films of conjugated polymers such as poly(*p*-phenylene vinylene) (PPV) and related derivatives show considerable promise in applications as light-emitting diodes (LED). In particular, these materials are attractive for their possible role in large area LEDs and may also be useful in photodiode detector applications. Interestingly, they have also been suggested as materials for fabricating a new generation near-field probe.[115]

Future industrial utilization of these materials, however, relies on understanding and improving properties such as the photoluminescence and electroluminescence efficiencies. Issues involving the consistency of the polymer thickness that affects the applied electric field distribution and the mesoscale morphology that can influence the local electronic properties of the polymer are also of great interest. As a result, correlations between the optical and topographical features at the submicron level provide much needed insight into polymer photophysics.

Poly(*p*-pyridyl vinylene) (PPyV) films prepared on quartz substrates were studied using polarized NSOM measurements of the photoluminescence (PL).[76] These measurements find evidence for small aggregated domains in the film with sizes on the order of 200 nm. In these experiments, both the horizontal and vertical components of the PL are simultaneously detected following excitation in the near-field with 488 nm light polarized in the 45° orientation. Distinct domains are seen in the PL images for both detection polarizations. Clear differences are also seen between the two PL polarization images indicating that emission was arising from oriented domains in the sample. Moreover, no correlation is found between the PL images and the topography image of the same region. This argues that the observed PL variations do not simply arise from variations in the sample thickness.

Further evidence for aggregation was found using a novel polarization modulation scheme to measure

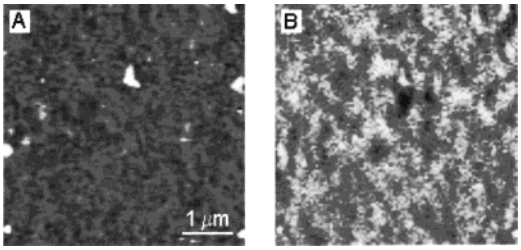


**Figure 20.** (a) NSOM topography and (b) anisotropy images of a PPyV film. Light areas in the anisotropy image correspond to approximately 2.5% polarization anisotropy and are not correlated with features seen in the topography image. Reproduced with permission from ref 76. Copyright 1996 American Institute of Physics.

the small anisotropy in the NSOM transmission.[76] In this technique, a combination of a quarter-wave plate and electrooptic modulator is used to rotate linear polarized light through 180° before coupling into the NSOM probe.[74,76,111,314,318,320] When the probe is positioned above a region of the sample that is optically anisotropic, a modulation in the light detected in the far-field is observed. Phase-sensitive detection can be used to detect the modulated light, and both the magnitude of the anisotropy and its direction (phase) can be measured. For weakly or nonabsorbing samples, the signal is complicated and depends on factors such as sample birefringence and refractive index. For strongly absorbing samples, however, these effects are small and the anisotropic extinction coefficient can be measured with <100 nm spatial resolution.

To complement the NSOM PL images of the PPyV film, polarization-modulation NSOM transmission measurements were taken. Again, domains were found in the film that were not correlated with surface topographical features and had characteristic sizes in the hundreds of nanometers range. Figure 20 shows the topography and NSOM transmission anisotropy images for the PPyV film.[76] The contrast observed in the anisotropic transmission image yields similar results as the NSOM PL images, again suggesting aggregation as the source of the domains. This was further supported by similar polarization-modulation transmission experiments on a nonaggregating polymer in which no contrast was observed. Taken together, these results provide convincing evidence for polymer aggregation on the hundreds of nanometers length scale which results in decreased PL efficiency in the film. As the authors point out, the formation of aggregates is deleterious for future LED applications and will have to be addressed, possibly through the introduction of disorder into the film which prevents aggregate formation.

Unlike studies on the PPyV films, NSOM studies on PPV films have found direct correlations between the structural and optical properties of the films.[81] NSOM PL images reveal small ≈100 nm domains of low PL efficiency in PPV that correlate, for the most part, with polymer clusters observed in the topography image. In some cases, dark areas in the NSOM PL image were not correlated with an obvious cluster in the force image which was attributed to clusters below the surface of the film.[81] Similar domains have also been seen in transmission NSOM experiments

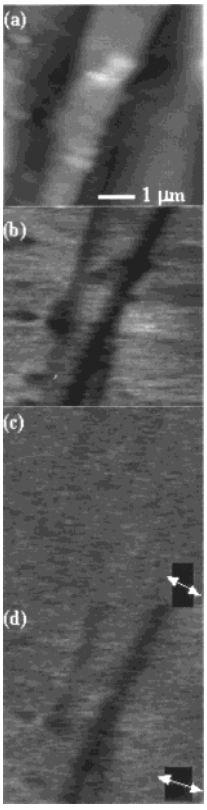


**Figure 21.** NSOM (a) topography, (b) total photoluminescence, and (c, d) polarized photoluminescence of a stretch-oriented PPV film. Comparing the total photoluminescence image (b) with the topography image (a) shows that the photoluminescence efficiency decreases near the edges of the fiberlike features and the clusters. There is little photoluminescence observed at a polarization orthogonal to the stretch axis of the fibers as shown in (c). Reproduced with permission from ref 81. Copyright 1997 Elsevier Science.

and assigned to regions of increased absorption.[107] NSOM PL spectra of the dark domains found that they had spectral profiles similar to those of the bright regions of the film which argues that they are distinct polymer regions and not simply contaminants.[81] Polarized absorption NSOM measurements found regions of polymer order on length scales of 100−500 nm. These areas, not observable in far-field measurements, were assigned to crystalline areas of the polymer on the basis of supporting electron microscopy data.

Stretch-oriented PPV films were also studied at the submicrometer level using NSOM absorption and PL measurements.[81] The films are mechanically stretched 4:1 which orients the polymer and results in a film linear dichroism of 8:1. Figure 21 displays the NSOM topography and the polarized absorption images for the stretch-oriented film. Shear-force topography images of the stretch-oriented PPV films are markedly different than those of unoriented samples. Fiberlike structures running parallel with the stretching axis are observed in the stretch-oriented films along with a reduction in the number of observable polymer clusters. Polarized NSOM absorption measurements on the oriented PPV films also reflect the dramatic changes induced by the stretching process.[81] A large contrast reversal is observed for the two

orthogonal polarizations, indicating a high degree of induced order in the polymer. Interestingly, while these experiments suggest a polymer ordering along the stretch axis in agreement with far-field measurements, they also find evidence for a perpendicular orientation near the edges of the fiber. This is seen in Figure 21 when comparing the two polarized absorption images with the fiber structures apparent in the shear-force image.

NSOM PL images of the stretch-oriented PPV also found a dramatic decrease in the PL efficiency near the edges of the fiber structures in the film.[81] NSOM PL measurements of emission polarized perpendicular to the stretch axis exhibited count rates near the background level. Measurements of the total PL or that polarized along the stretch axis were similar and showed emission from the fiber structure. The striking feature of these images is the loss of PL efficiency near the edges of the fiber which appear dark in the NSOM PL images. This quenching of the PL was ascribed to effects arising from the orientation difference of the polymer near the fiber edges.

Thin films of 9,9-dihexylpolyfluorene are being investigated for use in blue-light-emitting diodes and lasers and for polarizing filters in flat panel displays. Recently, NSOM has been used to study the local ordering in these films using fluorescence polarization measurements.[321] Thin films are produced by spin coating from a toluene solution onto a substrate, followed by annealing at temperatures near the liquid crystalline phase transition. Figure 22 (top) shows a conventional far-field image taken using crossed polarizers in which strong ordering is observed on the 1−5 $\mu$m length scale. The bottom two images are 2 $\mu$m × 2 $\mu$m near-field fluorescence images taken at orthogonal polarizations. Average polarization ratios of ≫20:1 indicate that the polymer is well ordered, with small domains observed on the ≫100 nm scale. Similar studies on polymers of varying alkyl chain lengths indicate that a greater degree of ordering is present in polymers with the shorter chains.[321]

Mixtures of light emitting polymers have also been studied with NSOM due to interest in using these blends to extend the emission range or modify the electronic properties of the polymers.[90,91,95] Fann and co-workers have used absorption NSOM measurements to investigate the inhomogeniety in polymer blends of PPV and poly(dioctyloxyphenylenevinylene) (PdOPV).[90,91] NSOM absorption measurements on films formed from mixing ratios of PPV to PdOPV of 1:1 and 1:14 indicate the presence of domains in both blends. Domain sizes are on the several hundred nanometers scale, relatively insensitive-to-blending ratio, and not correlated with film topography. These results combined with time-resolved measurements of the PL decay suggest that mixing in the higher ratio films is more homogeneous than that at the 1:1 ratio. This, however, is dependent on the film preparation method (dipping versus spin coating).

In other results on blended polymers, distinct differences in domain formation were found as the polymer ratio was adjusted. In the study by Webster et al., the photoluminescent and electroluminescent conjugated polymer poly(2,5-dialkoxy-*p*-phenylenevinylene) (PDAOPV) was mixed at different ratios with nonelectrically excitable poly(methyl methacrylate) (PMMA).[86] The mixture is spin coated onto glass to form a film of thickness ≈60 nm. NSOM PL images were taken on film compositions of 1%, 10%, 25%, and 50% PDAOPV by weight. At low PDAOPV percentages, small domains of PDAOPV were observed in the film that evolved into a connected network of PL regions as the ratio was increased.

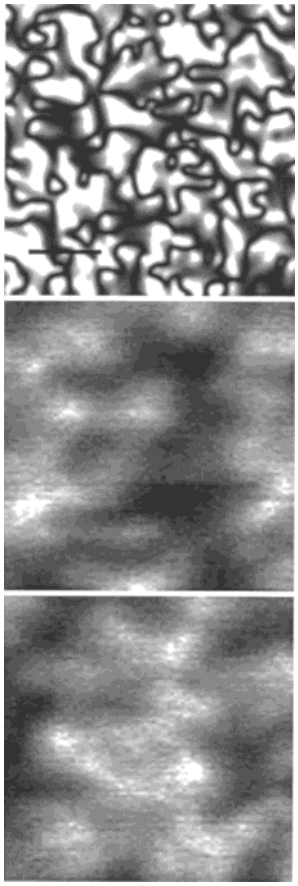

**Figure 22.** Images of a 9,9-dihexylpolyfluorene thin film taken with conventional far-field microscopy using crossed polarizers (top) and with higher resolution near-field fluorescence measurements at orthogonal polarizations (middle and bottom). The scale bar in the top image is 5 $\mu$m, and the bottom two images are both 2 $\mu$m × 2 $\mu$m. Reproduced with permission from ref 321.

For annealed films, contrast reversal is observed in the height images while the NSOM PL images remained relatively unchanged. Figure 23 presents NSOM results and line cuts, respectively, for the shear-force image of a film before annealing (a and b) and of a different sample after annealing (c and d) and the NSOM fluorescence image taken on the postannealed film shown in part c (e and f).[86] Before annealing, shear-force cross sections of the films indicate PDAOPV clusters protruding ≈40 nm from the surface of the film. Upon annealing, these features reverse direction and appear as dips of approximately 15 nm in the film surface. While annealing dramatically affects the topography of the film, the fluorescence images show no evolution in the observed domains. The mechanism of the topography change remains to be determined, and this process

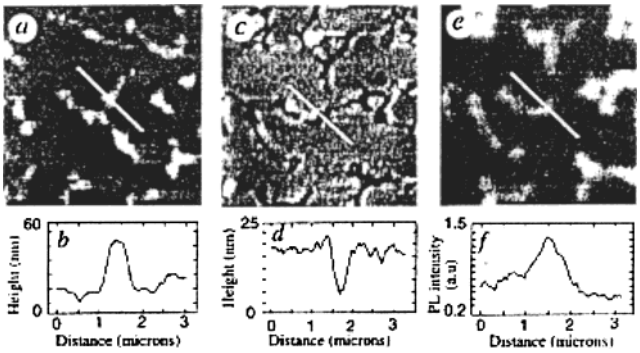


**Figure 23.** Shear-force topography (10 $\mu$m × 10 $\mu$m) (a, c) and fluorescence (e) images of a PDAOPV film before (a) and after (c, e) annealing. Line cuts of the images are shown below (b, d, f) at the regions indicated by the white line in (a, c, e), respectively. Upon annealing, a contrast reversal is observed in the shear-force images in which raised features in (a) before annealing appear as areas of lower height afterward (c). The fluorescence is not affected by annealing the film. Separate films were used to collect the annealed and unannealed data. Reproduced with permission from ref 86. Copyright 1998 Elsevier Science.

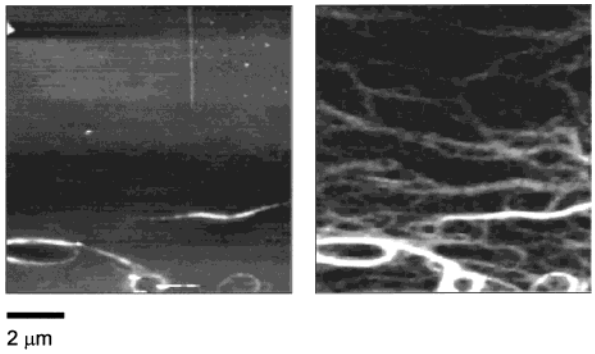


**Figure 24.** NSOM (left) topography and (right) fluorescence images of a 10 $\mu$m$^2$ area of J-aggregates embedded in a thin film of PVS. Thin stringlike J-aggregates are observed throughout the NSOM fluorescence image and are partially correlated in the force image at regions in which they are near the surface of the film. Reproduced with permission from ref 71. Copyright 1995 American Chemical Society.

may be useful in controlling the specific submicron structure of these materials.

Controlling the submicrometer structure in these films presents another area which NSOM may be able to make useful contributions. Recently, micropatterning with 100 nm resolution using NSOM has been demonstrated on electroluminescent films of poly(3,4-diphenyl-2,5-thienylenevinylene) (DP-PTV).[92] At high fluence and in oxygen-rich environments, photooxidation occurs at the $\pi$-bonds to form carbonyl groups which shortens the conjugation length in the polymer and shifts the absorption from the visible to the UV. Therefore, in the presence of oxygen it is possible to photooxidize specific features into films using the visible output from the NSOM probe which can subsequently be read through NSOM imaging of the same area.

## V.B. J-Aggregates

J-aggregates are of interest from both a fundamental and a practical standpoint. For example, they serve as excellent models to study photophysical processes such as exciton migration which is important in the light collection mechanism of photosynthetic antenna systems. From a practical viewpoint, there is interest in probing the molecular level optical properties of J-aggregates due to their utility as sensitizers in the photographic industry. NSOM, therefore, provides a useful window into the optical properties of aggregated systems with a spatial resolution appropriate to directly probe many of the important photophysical properties.[11,70,71,75,77,84,97,98,102,313,322] Molecular aggregates of 1,1′-diethyl-2,2′-cyanine iodide, pseudoisocyanine (PIC), grown in thin films of poly(vinyl sulfate) (PVS) have been the subject of several recent NSOM studies.[11,70,71,75,77,97,313]

NSOM studies by Barbara and co-workers on J-aggregates of 1,1′-diethyl-2,2′-cyanine iodide (PIC) suspended in thin films of poly(vinyl sulfate) (PVS) are excellent examples of the structural and dynamic information accessible with NSOM.[11,70,71,75,77,97,313,314] PIC aggregates form fibrous structures in PVS films and are characterized by considerable local ordering and unique spectral properties associated with the tight packing of the molecular transition moments. This tight packing leads to collective properties such as a red-shifting and narrowing of the lowest energy electronic transition, known as the J-band. The evolution in the transition arises from a delocalized electronic state formed in the aggregate that extends over several neighboring monomeric units.

The samples are prepared by spin-coating a mixture of PIC and PVS onto a glass coverslip to a thickness of tens of nanometers. Threadlike structures of the fluorescent PIC in the PVS host result. Simultaneous shear-force and near-field fluorescence images of J-aggregates suspended in a PVS film are shown in Figure 24.[71] The near-field fluorescence image reveals the threadlike structures in the polymer matrix that extend for tens of micrometers.[11,70,71,75,97,313,314] When the threads extend out of the matrix, a clear correspondence is observed between the shear-force height image and NSOM fluorescence image. Otherwise, the aggregates are only visible through the fluorescence image.

The flexibility of the fibers is suggested by the highly curved regions or even the formation of loops in the aggregates. Excitation of the fluorescence with polarized light at several different wavelengths shows that the monomers forming the aggregates are highly organized. Wavelengths corresponding to excitation of the high-energy (488 nm) and low-energy (570 nm) regions of the exciton band indicate alignment of the transition dipoles perpendicular and parallel, respectively, with the long axis of the aggregates.[11,70,97,314] The polarization measurements indicate that the aggregates adopt a herringbone-like structure. From these measurements, an upper limit of 30° was placed on the spread of local dipole orientations, and this order is found to be maintained over distances relatively large when compared to the NSOM probe.[314]

The order in the aggregates can further be observed through single point spectral measurements taken as a function of position along single aggregate

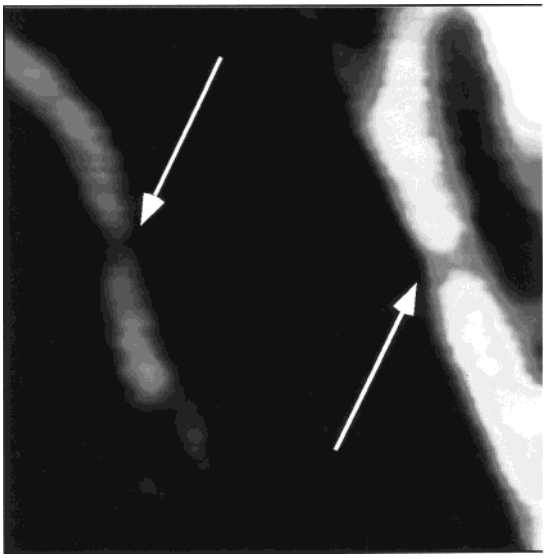

**Figure 25.** NSOM fluorescence image of a 2.5 $\mu m^2$ region of the film in which a line in the J-aggregate fluorescence has been photobleached with the NSOM tip (areas indicated by arrows). Reproduced with permission from ref 71. Copyright 1995 American Chemical Society.

threads. These measurements reveal small 3−5 nm variations in the emission peak wavelength along a single thread or between different threads in the sample.[71] Furthermore, the spectra at specific locations measured by NSOM are very similar to bulk measurements made in the far-field, all of which suggests that inhomogeneous broadening is not significant at the lengths probed by NSOM. These direct measurements confirm the results from studies on bulk samples indicating the long-range order present in the aggregate threads.

The order in the aggregates has also been probed by photobleaching a small line across a thread by increasing the power out of the NSOM tip.[11,71] Figure 25 shows a NSOM fluorescence image of a J-aggregate sample in which a small line has been photobleached, as indicated by the arrows.[71] The high degree of ordering between the close packed monomers in the aggregates leads to strong excitonic coupling between the transition dipoles. Once excited, several mechanisms of exciton decay including photobleaching are possible. In principle, the extent to which the excitons migrate along the aggregate should be visible by examining the size of the photobleached area. If exciton migration is greater than the NSOM probe size, the photobleached area should reflect this in subsequent NSOM fluorescence images. The validity of this, as pointed out by the authors, depends on several assumptions concerning the magnitude of effects such as tip heating and local energy transfer effects to the tip.[71] The results indicated that the extent of exciton migration occurred on length scales smaller than the resolving power of the measurements. This places an upper limit of approximately 50 nm for exciton migration in these aggregates.

The confinement of the exciton migration length to the sub-100 nm scale has also been confirmed through lifetime measurements taken by combining time-correlated, single-photon counting with NSOM.[77] Lifetime measurements were taken as a function of location on an aggregate to probe any structural dependence present in the exciton lifetime. All locations yielded similar decay constants of ≈8.5 ps indicating no structural dependence in the exciton lifetime on length scales of the tip aperture. Moreover, comparisons between near-field and far-field lifetime measurements were in close agreement verifying no perturbation to the lifetime from the nearby metal coated NSOM tip. This is consistent with the fast time scale of the exciton decay.

In related studies, small defects in PIC crystals were found to give rise to interesting spectroscopic signatures.[313] Far-field fluorescence spectra of samples collected as a function of time show a spectral evolution in the PIC peak emission from 620 nm, observed in fresh samples, to 700 nm in aged samples. The fluorescence red shift was assigned to the emergence of defect sites within the crystal. High-resolution NSOM images and spectra show distinct regions within the crystal containing these defect sites. On the basis of far-field excitation spectra and time-correlated single photon counting measurements, the 700 nm emission was attributed to defects in the PIC crystal that serve as low-energy traps for the PIC excitation.[313] Compared to the PIC emission spectra recorded with NSOM excitation, the spectrum collected with far-field illumination broadened approximately 100 $cm^{-1}$. This indicates that the spatial confinement provided by the NSOM tip (100 nm) reduces the amount of inhomogeneous broadening resulting from crystal features that occur over distances greater than 100 nm.

## V.C. Liquid Crystals

Liquid crystals (LC) are an electrically switchable class of materials that are commercially important in areas such as display technologies and window applications. Because these materials are birefringent, far-field optical techniques using crossed polarizers can reveal the LC organization on distances on the order of microns. For higher resolution studies, scanning probe microscopies have provided some information on the topography induced in the sample arising from the underlying LC structures. The optical contrast modes and polarized light capabilities of NSOM are ideally suited to probe sample birefringence at the submicrometer level, thereby complementing other studies in probing LC organization in films and droplets.[74,93,94,256,318,319,323]

LC films of 4′-octyl-4-biphenylcarbonitrile (8CB) have been studied by several groups at the liquid−vapor interface.[256,319] LC films of 8CB spin coated onto a glass substrate have been studied by Moyer et al. in a reflection-mode geometry.[319] Following polarized illumination in the near-field at 488 nm, the light reflected/scattered off the LC surface was collected from the side with a long working distance objective at an angle of 45°. The results showed that the LC film could be modified with the light exiting the NSOM tip without substantial modification of the surface topography. The ability to optically modify and subsequently read the LC films with ≈65 nm resolution was cast in terms of its potential for future applications in data storage.

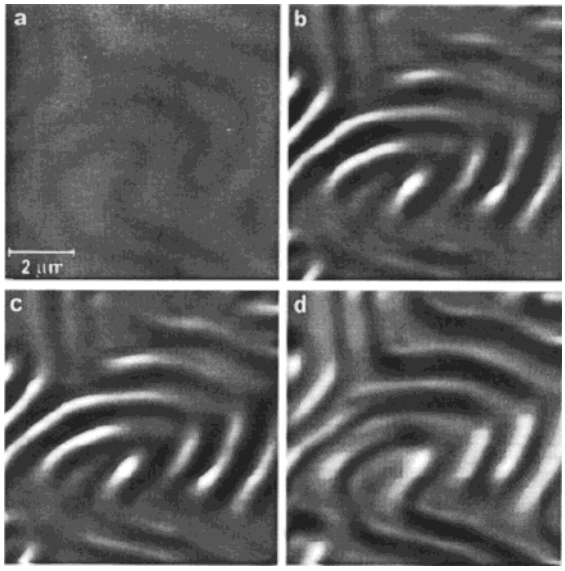


**Figure 26.** NSOM images of a liquid crystal film taken using a polarization modulation technique to measure the sample birefringence. Shown are the (a) topography, (b) total amplitude of the modulated intensity, (c) average intensity, and (d) phase of the modulated signal. Reproduced with permission from ref 318. Copyright 1998 American Institute of Physics.

Cholesteric liquid crystals spin coated onto a glass coverslip have been studied using a polarization modulation NSOM technique sensitive to sample birefringence.[318] This particular LC forms a helical structure in which the pitch can be varied by mixing in a chiral dopant, ZLI-4572. Polarization modulation NSOM, in which linearly polarized light from a 633 nm HeNe laser is directed through a Pockels cell to modulate the polarization before coupling into the fiber optic NSOM probe, was used to probe the sample birefringence. The sample birefringence is directly related to the structures formed in the LC sample making it a sensitive probe of the submicrometer organization in the film.

NSOM topography, amplitude of the modulated intensity signal, phase of the signal, and average optical intensity were collected as a function of the sample constituents. Figure 26a−d displays the topography, amplitude, average intensity, and phase, respectively, of a typical cholesteric LC.[318] Clearly evident in the optical images are textures consistent with the known LC patterns observed with far-field optical techniques. The patterns consist of ordered tubular structures with semihelical designs intermingled. The shear-force topography image also shows the same sample periodicity in structure, in agreement with previous AFM studies. As a check against artifacts associated with a coupling between the optical and topography images, the optical images were also collected in constant height scans of the same sample region. These revealed similar optical results indicating no significant dependence on the topography or tip−sample gap. Upon lowering of the chiral dopant, smaller periodic structures were observed in the film. Analysis of the origin of both the modulated intensity amplitude and phase indicate that variations in sample birefringence contribute to both signals. The analysis also showed that both signals contained contributions from both the sample birefringence and the orientation of the helical axis, although each has a different dependence.

Recently Higgins and co-workers have worked to develop new NSOM methods for probing both the structure and dynamics of polymer dispersed liquid crystal films.[28,93,94,316] These films consist of small birefringent nematic LC droplets suspended in a polymer matrix. The films are electrically switchable between opaque and transparent states which again makes them useful for display and window applications. The interest lies in understanding both the microscopic structure of the LC in the droplet and the dynamics associated with LC switching in response to potential changes. NSOM studies using polarized light, therefore, offer a unique probe to understand the submicrometer organization of the droplets, the correlations between LC structure and droplet topography, and the dynamics of reorganization within the droplet.

NSOM topographic images of LC droplets encapsulated in a poly(vinyl alcohol) (PVA) film reveal significant distributions in their shapes. While some droplets appear spheroidal, others adopt a more toroidal shape which may reflect the leakage of LC from the droplet during formation. Repeatable and stabletopographic images of the PVA sample indicate a fairly rigid encapsulated LC structure.

Transmitted light NSOM images taken in a crossed-polarizer arrangement probe the birefringence present in the LC droplets. Comparison of the NSOM optical and force images provides a self-consistent view of the droplet organization and allows for the assignment of the LC alignment within the droplet. This can be seen in the NSOM topography and cross-polarized optical images shown in Figure 27 for spheroidal and toroidal shaped droplets.[93] Clearly evident in the topography images are the shape differences between these two droplet forms. The cross-polarizerd NSOM optical images, which map the LC orientations, also demonstrate a clear difference between the two droplets. These differences are consistent with the idealized organizations shown schematically in Figure 27.[93] Due to the thickness of the droplets, some mixing of the near-field and far-field information may occur which can obscure some of the high-resolution optical information. However, high resolution is only one of the NSOM attributes exploited in these studies. The simultaneous collection of sample topography allows the confident assignment of the various droplet forms which strongly influences the LC alignment. The simultaneous optical and topography information proves to be a powerful tool in assigning the particular droplet shape and resulting LC organization.

To investigate the reorientation dynamics of the LC within the droplets, a sinusoidal voltage was applied to the end of the NSOM probe.[316] The polymer-encapsulated LC films were deposited onto a glass cover slip coated with indium tin oxide (ITO), which provided a transparent conductive support for the film. Model calculations of the electric field gradients between the NSOM tip and the sample indicate that sample volumes as small as $10^{-14}$ $cm^3$

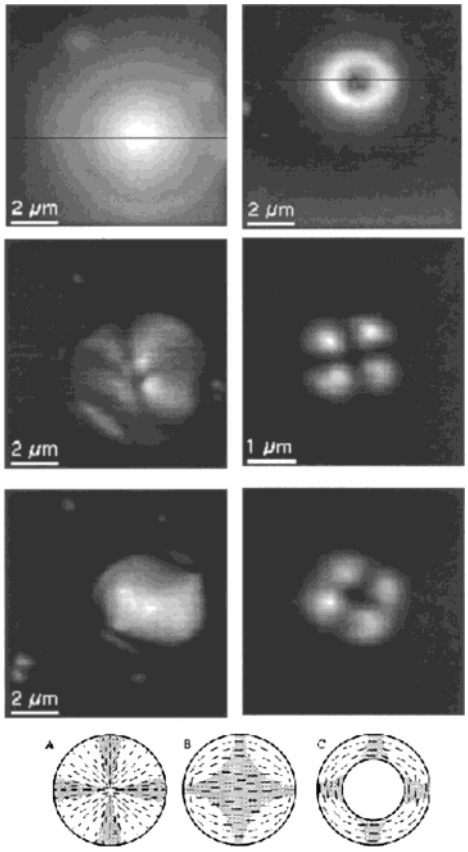


**Figure 27.** NSOM topography (top images) and cross-polarized optical (middle and bottom) images of LC droplets suspended in a polymer film. Results from two droplet shapes are shown. The upper left image shows the topography of a spheroidal droplet with the cross-polarized optical images indicative of these droplet forms located directly below. A toroidal shape droplet is shown in the upper right image with the cross-polarized optical images shown directly below it. The optical images provide insight into the LC organization, a schematic of which is shown at the bottom of the figure. Reproduced with permission from ref 93. Copyright 1998 American Chemical Society.

can be probed at low applied potentials.[316] Thus this arrangement provides a method in which a wave of varying frequency can be applied between the NSOM tip and the sample to reorient a fraction of the LC molecules under the tip. Detection of the amplitude and phase of the modulated signal with phase-sensitive methods, therefore, probes the LC dynamics in localized regions of the droplet.

Figure 28 shows a schematic of an idealized spheroidal droplet and the shear-force topographical image of the droplet in the film. Also shown are the dynamic amplitude and phase images of the same droplet taken by modulating an electric field between the NSOM tip and the sample at 100 Hz.[316] The double-ended arrows indicate the directions of polarization for the incident and detected light. The dynamic phase measurements turn out to be more straightforward to interpret than the dynamic amplitude signal, which is complicated by both static and dynamic contributions.

The dynamic phase signal is sensitive to variations in the reorientation times of the LC molecules and, unlike the amplitude signal, is less sensitive to the initial LC orientation and sample thickness. In

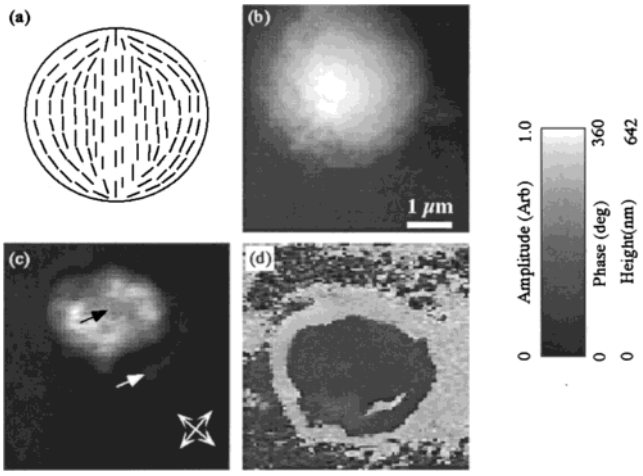


**Figure 28.** Results from polarization modulation experiments on a spheroidal LC droplet similar to that shown in Figure 27. (a) shows a schematic of the LC organization, (b) is a topography image of the droplet, and (c) and (d) show the dynamic amplitude and phase images, respectively, taken while modulating the polarization at 100 Hz. Reproduced with permission from ref 316. Copyright 1998 American Chemical Society.

Figure 28, a positive phase shift in the signal near the droplet edges produces a bright ring in the phase image. The observed contrast indicates that the reorientation times for LC molecules near the polymer interface of the spheroid are different than those centrally located in the particle. To gain quantitative information on the dynamics, single point measurements were taken as a function of tip location over a droplet. Both relaxation times (field off) and rise times (field on) were measured and generally exhibited faster orientation dynamics for molecules located near the polymer interface.[316] Interestingly, this contradicts previous work which proposed a long relaxation time for molecules near the interface and shorter times for those in the bulk. It was suggested that this apparent contradiction may arise from difficulties in measuring the molecules truly at the interface and not merely located in a region near the interface. Further experiments will be needed to reveal the source of this contradiction, but these measurements nonetheless illustrate the power of NSOM in correlating structural and optical properties of films and in measuring dynamics in specific local environments.

## V.D. Langmuir–Blodgett Films

Langmuir films consist of molecules trapped at the interface between two dissimilar phases. A prototypical example is amphoteric molecules trapped at the air/water interface. This class of molecules includes phospholipids which contain a hydrophilic headgroup and nonpolar tail groups. When dispersed on an aqueous subphase, the polar headgroups solvate in the subphase while the nonpolar tailgroups prevent the complete solvation of the molecule. By compression of the dispersed film at the air/liquid interface with a moving barrier, the monolayer can be forced through phase transitions that change the packing and order of the molecules. The transitions through the various phases are observable in the pressure

isotherm measured by monitoring the surface pressure of the film as it is compressed. The resulting film can be studied at the air/water interface or transferred onto a solid support using the Langmuir−Blodgett dipping technique.

Films transferred onto solid supports using the Langmuir−Blodgett (LB) technique have been studied for optical coating applications, for use as nonlinear optical devices, and in forming supports for novel sensor devices. In more fundamental studies, LB films are often used to examine the phase partitioning and resulting structures formed in monolayers as parameters such as constituents added to the film or when external conditions are varied. They have also served as mimics of natural biological membranes. These types of studies, for instance, have revealed insights into the role of cholesterol and other natural membrane constituents on film properties such as phase partitioning and fluidity. The coexisting phases in these films are often studied by doping in fluorescent analogues that partition into a distinct phase. The phase partitioning in the film can then be visualized using conventional fluorescence microscopy techniques, and these studies have provided a wealth of information on the micrometer scale.

To probe the submicrometer structure of LB films, atomic force microscopy (AFM) has proven effective. The small height differences between the various phases in the film provides the necessary contrast for AFM. However, because these measurements rely mainly on small topographical differences in the film, unambiguous assignment of the phase structure is sometimes problematic. Furthermore, there is frequently information that is not tied to height changes in the film which AFM cannot access. For instance, experiments described below by Hwang et al. use NSOM fluorescence measurements to probe properties of phase boundaries in LB films not accessible in height measurements alone.[324] NSOM, therefore, holds the potential of complementing AFM and fluorescence microscopy measurements by simultaneously measuring both the fluorescence and height signatures at the submicrometer level.[65,72,73,78,80,84,99,100,103,105,118,123,213,231,232,268,277,278,311,312,324−329]

One of the early NSOM studies on lipid monolayers found evidence for previously undetected structures. LB monolayers of DPPC doped with 0.5 mol % fluorescent Bodipy-PC were studied by Hwang et al. as a function of constituents added to the film such as cholesterol.[324] Monolayers were transferred onto a glass substrate at various locations along the pressure isotherm to study the structural features associated with the lipid phases. These studies led to the discovery of previously undetected features in the monolayer structure and pointed to interesting new phenomena only visible through the high-resolution optical signal. For instance, DPPC monolayers containing a small mole percentage of cholesterol showed a fine branching structure on the submicrometer level connecting domains of the liquid expanded (LE) phase. The existence of these structures fits well with current theories predicting the effects of cholesterol on the boundary energies of the lipid phases.[324]

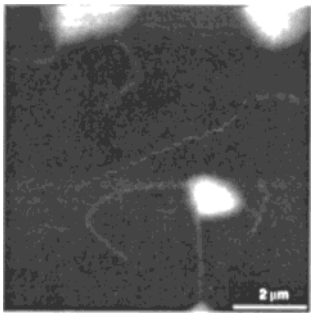


**Figure 29.** NSOM fluorescence image of a DPPC/Bodipy-PC/0.5 mol % ganglioside $G_{M1}$ LB monolayer transferred onto a glass substrate at a surface pressure of 10 mN/m. The fluorescent liquid-expanded domains have narrow fluorescent "whiskers" stretching out into the dark liquid-condensed regions of the film. Reproduced with permission from ref 324. Copyright 1995 American Association for the Advancement of Science.

As the pressure of the film was further increased, the NSOM images showed an increasingly complicated weblike structure in the lipid monolayer. Similar experiments with DPPC layers doped with 0.5 mol % ganglioside $G_{M1}$, transferred at a pressure of 10 mN/m, showed the formation of thread type structures in the NSOM images. The NSOM fluorescence of this film is shown in Figure 29.[324] Small fluorescent strands are seen to connect the larger fluorescent domains in the film. These small strands were interpreted as arising from residual liquid expanded regions trapped in the larger liquid condensed (LC) lipid domains. The ganglioside present at the grain boundaries may act to prevent the complete coalescing of the different lipid phases in the film thus leading to the intricate patterns.

The transition across a grain boundary was also investigated by examining the fluorescence intensity profile at the lipid phase interface. A true phase boundary would be expected to have a very sharp transition in the fluorescence image indicating the complete partitioning of the dye between the two regions. NSOM fluorescence and line cuts through the LE/LC domain boundaries of a DPPC/Bodipy-PC film and a similar film containing 0.5 mol % ganglioside are shown in Figure 30.[324] For the DPPC/Bodipy-PC film, a gradual gradient in the NSOM fluorescence intensity is seen indicating a smoother transition across the LE/LC boundary than that expected for a phase separation. It was suggested that this may result from electric fields near the boundary acting to induce a concentration gradient in the monolayer. Upon the addition of ganglioside, the transition across a boundary becomes much steeper in the NSOM fluorescence image, information not accessible with AFM or far-field measurements.

A recent electrostatic model shows that parameters such as the molecular packing density, dipole density, and electric field gradients are all able to influence the concentration gradient in lipid monolayers. These effects were investigated on the DPPC monolayers by using combinations of monolayer content (i.e. the presence of ganglioside) and pressure to demonstrate that the fluorescence gradient did indeed behave differently for the various monolayers. As shown in Figure 30, monolayers incorporating ganglioside

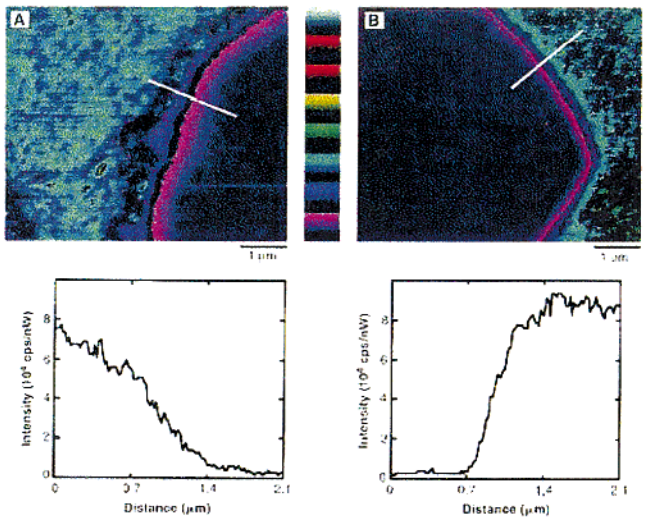


**Figure 30.** NSOM fluorescence images and associated line-cuts across the phase boundaries. The line-cut across the DPPC/Bodipy-PC monolayer shown in (a) indicates a gradual change in the dye concentration across the phase boundary. For monolayers of DPPC/Bodipy-PC/0.5 mol % ganglioside $G_{M1}$, as shown in (b), the transition is much sharper. Reproduced with permission from ref 324. Copyright 1995 American Association for the Advancement of Science.

display a much steeper concentration gradient across the phase boundary indicating that the negatively charged headgroups influence the films either through screening dipoles or altering the packing densities. It is important to note that the NSOM fluorescence signal used to measure the gradient in the ganglioside doped film rose over a length scale less than 700 nm, indicating the need for the high spatial resolution afforded by NSOM measurements.[324]

Several studies have demonstrated the ability to probe the phase differences in LB films by comparing the simultaneously collected fluorescence and topographical images.[65,72,99,100,103,105,118,123,213,232,268,277,278,311,312,325−329] In one study, DPPC was transferred onto a glass coverslip at a surface pressure of 15 mN/m in the LC/LE coexistence region of the pressure isotherm.[72] The fluorescent membrane probe $diIC_{18}$ was doped into the film at a concentration of 0.25 mol % providing a marker for the less dense LE lipid phase domains. NSOM fluorescence images of the film revealed fluorescent LE domains connected by small threadlike LE regions. Interestingly, as in previous studies, the threadlike structures often adopted a $C_3$-like symmetry at the junctions with a 120° separation between the different arms. For the larger LE domains, corresponding regions of decreased height were observed in the NSOM topographical image providing an additional marker for the phase segregation. The measured height differences between the LE and LC phases was measured to be 5−8 Å, consistent with previous AFM measurements on similar LB films.[72]

Although a direct correlation was seen in the NSOM fluorescence and topography images for the larger lipid domains, a direct one-to-one correspondence was not apparent for many of the smaller features. This was attributed to complications arising

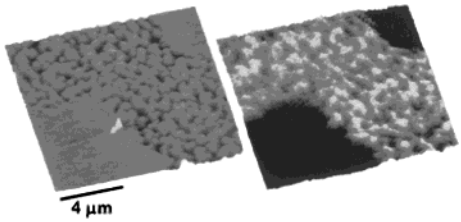


**Figure 31.** Simultaneous NSOM topography (left) and fluorescence (right) images of a DPPC/0.25 mol % $diIC_{18}$ lipid monolayer transferred onto a mica surface at a pressure of 9 mN/m. The small 5−8 Å height differences between the LE and LC phases observed in the topography image correlate directly with the structure observed in the fluorescence image, where the LE regions contain the fluorescent dopant. Reproduced with permission from ref 278. Copyright 1998 Biophysical Society.

from a convolution in the height contrast from the glass substrate used to support the film. A later study in which the DPPC films were transferred onto a freshly cleaved, atomically flat mica substrate was successful in correlating all the domains in both fluorescence and force images.[278] This study found that for DPPC monolayers transferred onto mica at 9 mN/m, small nanometric LE and LC islands are formed in the "LE" regions between the larger LC domains. Figure 31 shows the NSOM topography and fluorescence images for a DPPC/0.25 mol % $diIC_{18}$ film transferred onto mica.[278] The topography image shows height changes in the film of 5−8 Å which correspond to the difference in height between the LE and LC phases. The lower height LE regions correspond directly with the fluorescently doped LE regions observed in the NSOM fluorescence image, and the LC regions that do not contain the fluorescent dye appear dark. The small islands observed between the large circular LC regions, which are beyond the resolution of far-field fluorescence microscopy, have been seen previously in AFM studies and assigned to either distinct lipid phases or defects in the film exposing the substrate. The simultaneous fluorescence and force measurements, however, confirm that these are distinct lipid islands.

In addition to the fluorescence and topography images normally collected with NSOM, other contrast modes have been incorporated to further probe these films. For example, a contrast mechanism commonly used in tapping-mode AFM to measure compliance differences in samples has been incorporated into NSOM measurements. This method utilizes phase-sensitive detection to monitor the changes in the phase of the tip resonance as the sample is imaged.[72] With cantilevered NSOM tips, this contrast mode is easily implemented to provide a third contrast mode that is sensitive to changes in the sample compliance.

In another example, Muramatsu et al. have demonstrated the capability of simultaneously measuring frictional contrast on LB films with NSOM.[103,105,311] Bent fiber tips were etched to small diameters, thus reducing the spring constant of the tip approximately 2 orders of magnitude.[106] With the reduced spring constant, contact mode imaging was possible without damaging the delicate NSOM probe or the sample. Height, friction, and fluorescence images of LB films formed from a three-component mixture of arachidic

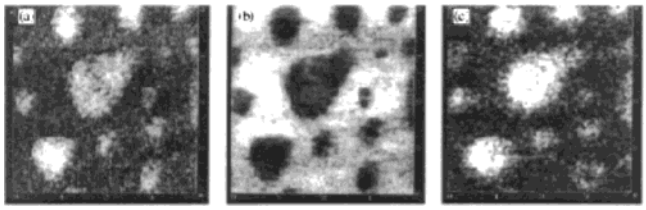

**Figure 32.** Simultaneous NSOM (a) height, (b) friction, and (c) fluorescence measurements taken on an LB film formed from a three-component mixture of arachidic acid, partially fluorinated carboxylic ether acid, and a cyanine dye in the ratio of 1:1:0.01. Reproduced with permission from ref 105. Copyright 1998 Elsevier Science.

acid, partially fluorinated carboxylic ether acid, and a cyanine dye in the ratio of 1:1:0.01 are shown in Figure 32.[105] Distinct frictional contrast is seen and can be correlated with the domains seen in both the height and fluorescence images. Frictional force measurements with modified tips is becoming increasingly useful in AFM applications. The demonstration by Muramatsu et al. of frictional NSOM measurements should open new areas of study for NSOM which provides complementary views of sample properties.[103,105,311]

Both far-field and near-field fluorescence studies have suggested that the phase structures formed in LB films can be influenced by the dipping mechanism utilized to transfer the film onto the substrate. The hydrodynamics induced by the dipping motion and dewetting following film transfer have both been shown to affect film structure under certain conditions. Far-field fluorescence measurements taken at the air/water/substrate (three-phase line) interface where the film is transferred onto the substrate have also found evidence for a substrate-mediated structural change in LB films. Insight into the various mechanisms for domain formation and their relative contributions to film structure have been studied with NSOM. These studies have found evidence for structural changes that are strongly tied to the subphase components used in transferring the film onto the substrate.

In one such study, DPPC monolayers were transferred onto mica at a surface pressure of 4 mN/m, which is lower than the main phase transition ($\pi_c$). The films show distinctive stripe structures as shown in Figure 33.[327] Figure 33 compares the NSOM fluorescence (A) and height (B) images for DPPC transferred from a pure water subphase (18 MΩ) and the fluorescence (C) and height (D) images for DPPC transferred from a subphase of 10 mM $MgCl_2$. As before, contrast in the height images arises from the 5−8 Å height differential between the LE and LC lipid phases. Contrast in the fluorescence images results from the fluorescent $diIC_{18}$ dopant which partitions into the LE phase.

Both films contain vertical stripes running in the direction of dipping and horizontal stripes perpendicular to the dipping direction. In both films the LE stripes are 200−300 nm in width and have a period of approximately 1−3 $\mu$m. Similar structures have been seen in previous fluorescence microscopy and AFM observations. For the film transferred from the pure water subphase (Figure 33A,B), the LE stripes

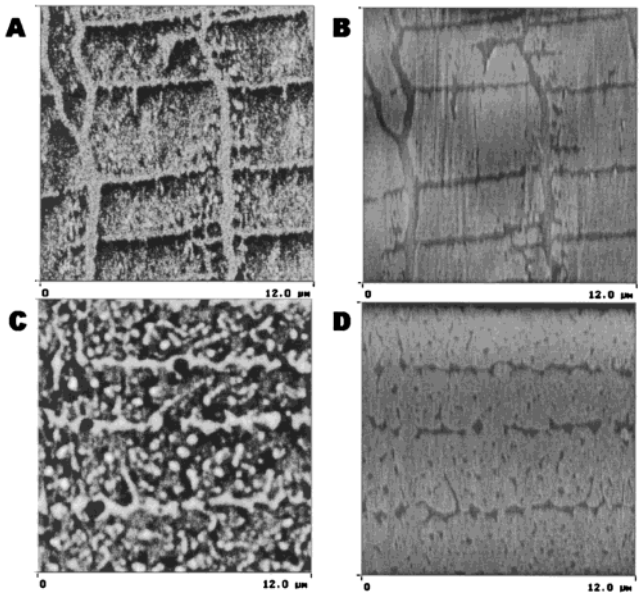


**Figure 33.** NSOM fluorescence (a, c) and height (b, d) images of DPPC/0.25 mol % $diIC_{18}$ transferred onto mica at a pressure of 4 mN/m. The film shown in (a) and (b) was transferred from a pure water subphase, and the film in (c) and (d) was transferred from a subphase containing 10 mM $MgCl_2$. Reproduced with permission from ref 327. Copyright 1999 Marston Book Service.

are separated by LC regions which contain a nonhomogeneous distribution of small LE domains.[327] This is evidenced by the fluorescence which maps the LE regions of the film. For this film, analysis of the lipid transfer ratios at several points along the pressure isotherm shows that when transferred below the $\pi_c$ the films are more dense than those at the air/water interface.

The structures observed in Figure 33C,D are indicative of domain aggregation following transfer that essentially lowers the film energy.[277,326,327] Compared to the film transferred from pure water, the stripe structures are more confluent and broken and the small LE domains have begun to aggregate into larger circular LE domains, similar to those formed at high humidity through domain aggregation.[277] This is suggestive of a "long" time structural evolution in the LB film in addition to the prompt surface mediated condensation occurring at the three-phase line.

These observations raise questions about the origin of the submicron structures seen in supported films and whether they are also present in similar films trapped at the air/water interface. This question, however, is problematic to address given the difficulties in making high-resolution measurements at this interface. Far-field fluorescence techniques, which are most readily applied to floating films, are restricted in resolution since high numerical aperture objectives cannot be used at these interfaces. Scanning probe techniques such as AFM are also problematic due to tip invasiveness toward these soft samples. NSOM, however, is unique in that the light exiting the tip can be used to implement new methods of tip feedback appropriate for probing the air/water interface. Several groups have begun implementing these schemes and have been successful at

making NSOM measurements on films at the air/liquid interface.[78,231,232,326] Initial results for DPPC films dispersed on a sucrose solution subphase seems to indicate that the small domains observed in supported films are not present in similar films at the air/liquid interface.[326]

The stated goals for many studies on lipid films is to provide insight into the possible submicrometer structures present in biological membranes.[72,83,278,324] Evidence for lipid microdomains in natural biomembranes has been found using a variety of techniques, but NSOM offers the possibility of directly studying these structures on the nanometric scale. Steps toward this goal have been taken in several NSOM studies that have been effective in identifying new structures in LB films that contain components commonly found in natural biomembranes.

The extension of these NSOM studies to biomembranes relies on the ability to detect similar lipid domains in bilayer films. This has recently been demonstrated with the results demonstrating how NSOM may be uniquely equipped to detect the small domains over other high-resolution techniques. This study by Hollars and Dunn focused on DPPC bilayers formed on mica in a stepwise fashion using a combination of the LB technique and the Langmuir–Schaefer (LS) technique.[278] Each monolayer of the bilayer was transferred onto the mica in the LE/LC coexistence region. AFM images of the resulting bilayer, shown in Figure 34a, reveal three quantized height changes in the bilayer consistent with the stacking of the lipid phase domains from each side of the membrane—LE on LE, LE on LC (or equally LC on LE), and LC on LC. This convolution in height information from both sides of the membrane complicates the assignment of the individual phase partitioning occurring in each side of the bilayer. However, by preferential doping of either side with a fluorescent marker, NSOM can selectively probe each side of the membrane with high spatial resolution. This is shown in Figure 34b,c which displays the NSOM fluorescence and topography images, respectively, for a bilayer in which only the bottom layer is doped with the fluorescent 0.25 mol % $diIC_{18}$.[278] The NSOM fluorescence image clearly reveals the underlying phase structure in the bottom monolayer of the film, providing a means of selectively probing each side of the membrane at the nanometric level.

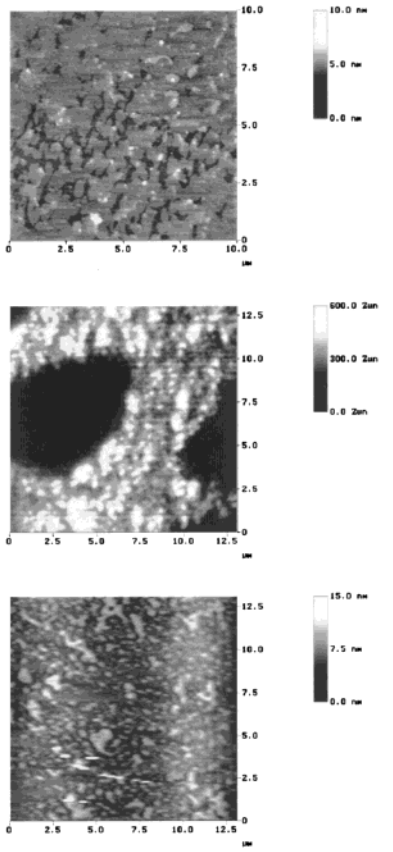

**Figure 34.** (a) AFM image of a DPPC bilayer formed on a mica surface. Three distinct height levels are observed in the film consistent with the convolution in phase height information from both sides of the membrane. Panels b and c show the NSOM fluorescence and height images, respectively, of a similar bilayer in which the bottom layer is fluorescently doped with 0.25 mol % $diIC_{18}$. This shows that the phase partitioning on each side of the membrane can be selectively probed. Reproduced with permission from ref 278. Copyright 1998 Biophysical Society.

## *VI. Applications in the Biological Sciences*

The simultaneous fluorescence and force mapping capabilities of NSOM seem particularly well suited to probe biological samples and provide new insights into complex structure–function relationships (see refs 1–3, 10, 19, 40, 41, 46, 49, 52, 53, 66, 67, 112, 120, 121, 123–129, 131–134, 136–142, 144–148, 150, 151, 154–156, 213, 232, 267, 278). These capabilities often complement other techniques routinely used in the analysis of biological samples. For instance, confocal microscopy, while having single molecule detection limits and exquisite sectioning capabilities, has lower spatial resolution and does not provide a force mapping of the surface topography. AFM, on the other hand, is remarkably sensitive to surface topography but under normal operation yields little specific chemical information. Used in conjunction with other techniques, NSOM should provide an informative new tool for exploring many biological structures and processes.

To compare the high-resolution imaging capabilities of NSOM with confocal microscopy, Betzig et. al. imaged the fluorescence from cytoskeletal actin of fixed mouse fibroblast cells stained with rhodamine-phalloidin.[121] The results clearly illustrate the greater detail observable with the higher resolution afforded by NSOM. These early results are significant for several reasons: they showed that (1) biological specimens can be imaged without damage due to the shear-force feedback mechanism used to position the tip near the sample, (2) high resolution near-field fluorescence measurements are possible even on relatively thick samples such as a cell, and (3) samples with complex surface topology and/or contamination remain amenable to high-resolution near-field fluorescence measurements. These studies also found that fluorescence photobleaching was greatly reduced in the NSOM experiments compared to similar confocal studies.

Since these original proof-of-principle reports, NSOM has been used to probe the photosynthetic systems,[40,41,46,52,120] genetic material,[66,67,123,127,129,134,138,139,141,148,156] membrane organization in cells,[19,131,132,136,267] green fluorescent protein,[131,140,146,154] and other biological systems.[1−3,10,19,149,151,330] Interesting applications have also included functionalizing the probes for use as nanometric chemical sensors.[8,122] To date, however, the NSOM imaging of unfixed cells under natural buffered conditions remains elusive due to the forces involved in the tip feedback mechanisms utilized. Following a survey of NSOM studies on biological samples, a brief look at progress toward reducing the tip−sample interactions in NSOM will be presented. Advancements in tip design and/or feedback are rapidly taking place and the imaging of living cells with NSOM will undoubtedly be reported soon, opening vast new applications in the biological sciences.

## VI.A. Photosynthetic Systems

High temporal resolution was combined with the high spatial resolution of NSOM to study the distribution of photosynthetic protein complexes in the thylakoid membrane from green algae.[41,52,120] The thylakoid membrane contains the light harvesting complex (LHC), photosystem I (PSI), and photosystem II (PSII), which are transmembrane protein complexes that participate in converting light energy into chemical energy. The spatial distribution of these complexes within the membrane is of interest and has been the subject of many studies utilizing techniques such as electron microscopy. Electron-based methods require destructive, unnatural sample preparations and only measure the size and shape of the embedded protein complexes, from which their identity remains ambiguous. Each complex, however, contains natural chlorophyll pigments which impart spectral signatures that are distinctive for the various complexes. This provides a mechanism for identifying and spatially mapping their location using the spectroscopic capabilities of NSOM.

As an initial NSOM trial, thylakoid membrane fragments from the *Chlamydomonas reinhardtii* PSI−PSII doubly deficient C2 strain which retain only the LHC II proteins were studied.[41,52,120] Membrane fragments were deposited onto a freshly cleaved mica surface and air-dried before imaging. Figure 35 shows the simultaneous force and near-field fluorescence image of the thylakoid membrane fragments lying flat on the mica surface.[120] The fluorescence is from the chlorophyll pigments contained in the LHC II which were excited using 633 nm light exiting the NSOM tip. As can be seen, the field of view contains two large membrane fragments and two smaller ones. From the force image, the heights of the membrane pieces range from 6.5 to 9.5 nm, which is consistent with that expected for a single bilayer membrane lying flat on the mica surface. Fluorescence is observed from the two larger membrane fragments indicating the presence of LHC II complexes. The lack of structure in the emission, it was suggested, reflects the isotropic distribution of LHC II throughout the membrane, which agrees with other studies showing a close packed arrangement of the LHC within the membrane. The absence of emission from the two smaller fragments indicates either a lack of LHC II complexes in these pieces or a prompt loss of fluorescence from photobleaching processes.

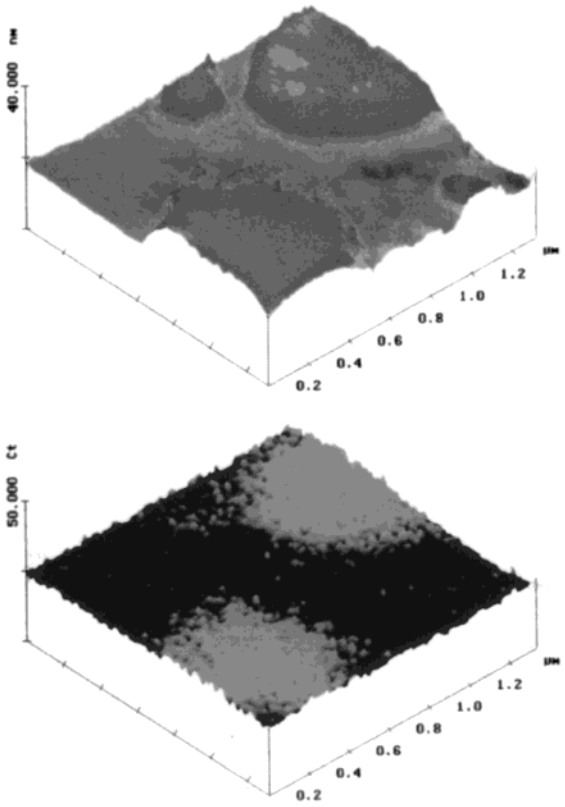


**Figure 35.** 1.3 $\mu$m × 1.3 $\mu$m NSOM (a) height and (b) fluorescence images of intact photosynthetic membrane fragments deposited onto a mica substrate. The LHC II proteins in the membrane fluoresce providing a marker for their locations. Reproduced with permission from ref 120. Copyright 1994 American Chemical Society.

The above results illustrate the ability to correlate near-field topography and fluorescence measurements to locate populations of LHC II in the membrane fragments. The resolution, however, is insufficient to resolve the individual LHC II units. Recently, however, these measurements have been extended down to the single LCH II level using a novel apertureless probe approach. By illuminating a sharpened metal tip with pulses from a femtosecond laser source, Xie and co-workers were able to resolve the fluorescence from LHC II containing membranes with 20 nm resolution.[207] Several features observed in the membrane fragments exhibited sizes at the resolution limit (≫20 nm) and with similar intensity levels. These were assigned to individual LHC II units in the membrane on the basis of previous electron microscopy results that found similar dimensions (≫13 nm) for the protein.

As mentioned earlier, the eventual goal of these studies is to spectrally map the locations of PSI, PSII, and LHC II in the photosynthetic membrane. One method of discriminating between these complexes is through fluorescence lifetime measurements. The feasibility of these types of measurements is demonstrated by measuring the fluorescence lifetime of the

LHC II in the membrane fragments. For these measurements, picosecond light pulses generated from a YAG pumped dye laser were coupled through the NSOM tip. The NSOM tip was precisely positioned above a region of interest and the lifetime was measured using the time-correlated single photon counting method. The fluorescence lifetime of the LHC II embedded in the membrane was found to be best fit by a sum of two exponentials with lifetimes of 450 ps (65%) and 2.7 ns (35%).[120] While the long lifetime component is identical to that measured in bulk samples, the fast component is almost a factor of 2 shorter. The amplitudes are also much different than those measured in the bulk which may reflect processes such as singlet−singlet annihilation or possibly tip effects such as those discussed earlier. These measurements are significant in that they show how NSOM can be used to probe natural pigment organization in a native membrane.

## VI.B. Protein Localization

In an elegant illustration of the advantages resulting from the high spatial resolution and spectral advantages inherent in NSOM, Weiss et al. carried out two color experiments on proteins colocalized in the erythrocyte membrane.[124,136] Human red blood cells infected with human malaria parasite (*Plasmodium falciparum*) were studied to probe the interactions between the parasitic proteins and the host skeletal proteins. It is known that as these parasitic proteins interact with the host proteins, the erythrocyte is altered such that ~100 nm knoblike structures are formed on the membrane of infected erythrocytes. To study these parasitic interactions, the two protein types (host and parasite) were selectively labeled and fluorescently imaged using simultaneous two color excitation and emission NSOM.

When the two color fluorescence images were acquired simultaneously using both excitation wavelengths exiting the NSOM tip, the two images provide a perfect pixel-by-pixel spatial mapping of the protein types in the membrane. Figure 36a,b shows the results from two experiments in which the host−parasite protein pairs of protein 4.1/MESA and protein 4.1/PfHRP1 were labeled.[124] The proteins were antibody labeled with FITC and Texas Red, and the dual color results for each experiment are shown in the left-hand column. The center column displays the combined red and green images, and the right column shows the direct pixel-to-pixel correlation between the two protein locations in the cell.

This mode of NSOM imaging avoids artifacts introduced by chromatic aberrations, inherent in studies using conventional lens microscopes, which can complicate this type of direct two color comparisons. Moreover, the shear-force feedback mechanism provides a simultaneous spatial mapping of the membrane topography that further allows for the identification of protein locations.[124,136] The low detection limits, chromatic free two color fluorescence capability, topographical information, and limited excitation volume of NSOM were all combined in this study to reveal a new and self-consistent picture of protein colocalization in malarial infected erythrocytes.

Several studies have used uncoated NSOM probes to study biological systems.[19,138−141,156] The origin of subdiffraction resolution with uncoated NSOM probes, however, remains controversial and requires more experimental work to firmly establish the resolution limits using this approach.[101,102,331,332] Clearly the fields emerging from an uncoated probe are not confined to a well-defined aperture as they are with metal-coated tips and light is able to escape from the sides of the probe. When a separate collection element is used to collect the optical signal, this leakage proves detrimental to obtaining high-resolution images. When used as both the excitation and collection element (shared aperture), it is suggested that uncoated fiber tips can achieve high resolution by double passing the aperture and rejecting the unwanted stray light.

Using this shared aperture mode that utilizes an uncoated fiber tip as the excitation and collection element, several studies have reported results for probing cell surface receptors.[19] Mouse fibroblast cells were cultured on glass coverslips and fluorescently labeled with both fluorescein and tetramethylrhodamine-conjugated concanavalin, which binds to glycoproteins on the cellular surface. Cells were subsequently fixed with formaldehyde and dried before imaging. The simultaneously measured shear-force topography, feedback signal, and fluorescence of the labeled cells are shown in Figure 37a−c, respectively.[19] The contours of the cell can be clearly seen in both the shear-force topography and feedback signal images. This can be compared to the NSOM fluorescence image which maps the locations of binding of the conjugated concanavalin with glycoproteins on the cell surface. A fourth image is shown in Figure 37d which combines the NSOM topography and fluorescence information into one plot. The structure observed in the fluorescence image points to a nonhomogeneous distribution of glycoproteins across the cell surface.[19]

As mentioned earlier, the cells were double labeled with conjugates of fluorescein and tetramethylrhodamine, a well-known FRET pair. To probe energy transfer between the two labels on the cell surface, photobleaching time scales of the donor (fluorescein) were measured both in the presence and absence of the second tetramethylrhodamine label. If energy transfer is significant in the double labeled samples, then a decrease in the photobleaching rate of the donor should be observed in these samples. As expected, experiments performed on both donor only and double labeled cells found a significant decrease in the photobleaching rate for the double labeled samples.[19] These and other results illustrate the possibility of combining FRET measurements with NSOM to probe distance relationships on the 1−10 nm scale in biological systems.

## VI.C. Chromosome Mapping

The high resolution of NSOM has also motivated the exploration of possible applications in the genome mapping areas.[123,127,129,134,138,139,148,156] Fluorescence in situ hybridization (FISH) is a standard technique used to locate specific gene sequences on a chromo-

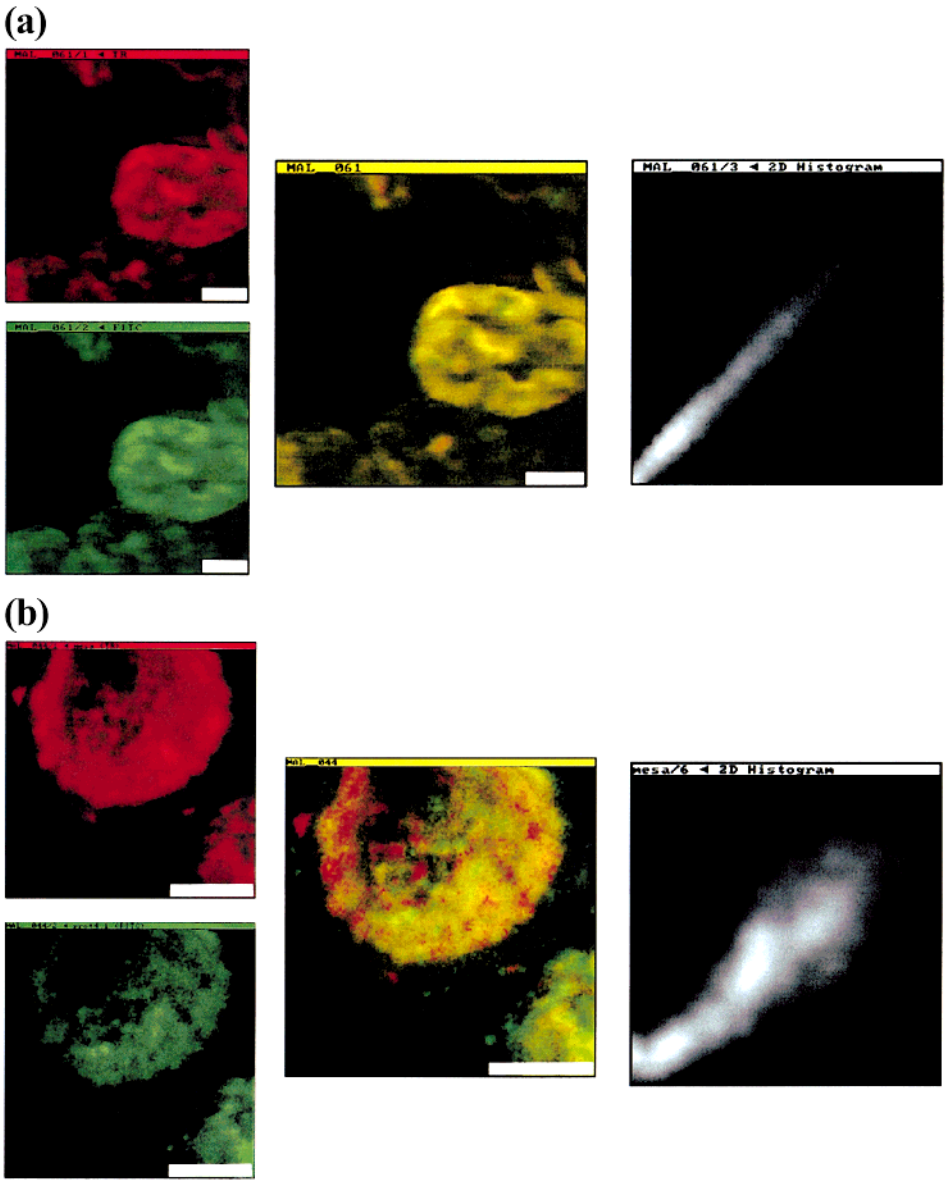


**Figure 36.** NSOM images of erythrocyte cells infected with parasites that have been antibody labeled with FITC for protein 4.1 and TR for MESA or PfHRP1. The images in the left column show the simultaneously collected fluorescence from the FITC and TR. The center column shows an overlay image and the right image shows a pixel-by-pixel correlation for the two fluorescence channels. The top collection of images colocalizes MESA and protein 4.1, and the bottom images show similar experiments for PfHRP1 and protein 4.1. Reproduced with permission from ref 124. Copyright 1999 National Academy Press.

some. Using conventional fluorescence microscopy, resolutions better than $10^6$ base pairs can be achieved with the FISH technique. For higher resolution, techniques such as AFM have been explored using topographical markers. This, however, loses the inherent advantages of multicolor labeling available with the fluorescence-based methods. The combined advantages of fluorescent tagging and high resolution have recently been demonstrated in a NSOM study by van Hulst and co-workers on labeled human chromosomes.[123,127,134] Figure 38 displays the results of two-color NSOM FISH measurements on a human metaphase chromosome labeled with CY-3 labels at the telomere probe p1−79 (Figure 38b) and FITC probes at the centromeric probe pUC-1.77 (Figure 38c).[134] The characteristic shape of the chromosome is easily observed in the force image shown in Figure 38a which facilitates the accurate determination of the individual marker locations revealed in the NSOM fluorescence images.

Many of the probes used in biology to specifically tag species in or on cells require excitation in the ultraviolet region of the spectrum. This creates problems for NSOM due to the optical fiber used to deliver the excitation light. Absorption and emission from the fiber becomes increasingly strong as the wavelength approaches the UV. These effects either limit the wavelength that can be delivered by the fiber or create large background signals that reduce the sensitivity of the detection system. One possible solution to circumvent many of these problems is through two-photon excitation, now gaining popularity in far-field applications. For far-field microscopy, two-photon excitation dramatically reduces the ex-

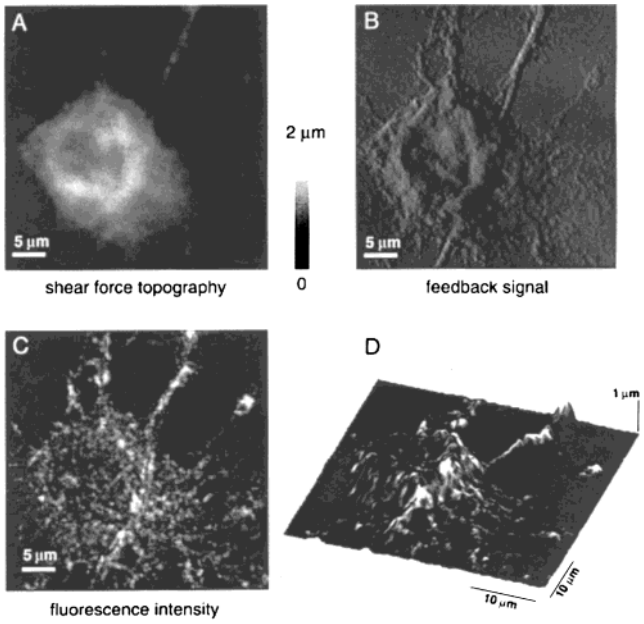


**Figure 37.** (a) Shear-force topography, (b) feedback error signal, (c) fluorescence, and (d) overlay of the topography and fluorescence signals for 3T3 Balb/c cells in which the glycoproteins on the cellular surface have been fluorescently labeled using fluorescein and tetramethylrhodamine bound to concanavalin A. The NSOM images were taken in the shared aperture mode using an uncoated fiber optic probe. Reproduced with permission from ref 19. Copyright 1998 CMB Association.

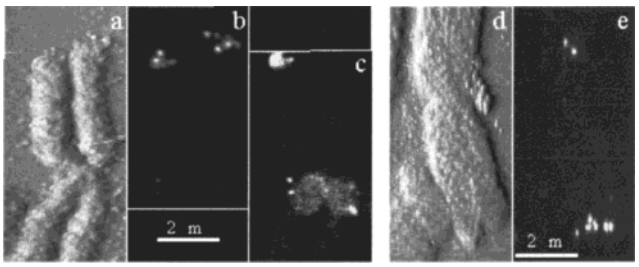


**Figure 38.** Two-color FISH NSOM images of a human chromosome. The two fluorescent labels observed in the images shown in (b) and (c) can be correlated with their location on the chromosome by comparing them with the simultaneously collected shear-force image shown in (a). Reproduced with permission from ref 134. Copyright 1997 Academic Press.

citation volume, suppresses background emission, and decreases photobleaching. Two-photon excitation combined with NSOM has the potential of opening applications involving UV dyes used extensively in biological applications.

Jovin and co-workers have used uncoated fiber tips in the shared aperture arrangement to demonstrate multiphoton excitation NSOM.[138,139,156] Two-photon NSOM was used to probe chromosomes labeled with DAPI and mouse fibroblast cells in which the DNA in the nucleus was labeled with BBI-342.[138,139] The 647 nm line of an Ar−Kr laser was coupled into the NSOM tip, and excitation powers ranging from 68 and 92 mW were used to image the samples. To unambiguously assign the signal to a two-photon process, the power dependence in the signal for excitation powers ranging from 8 to 180 mW was measured. The power dependence was complicated by a linear component presumably arising from emission from the fiber. However, a significant quadratic component showing the expected dependence in the square of the intensity was found on stained samples confirming the presence of a two-photon process. This results illustrate the feasibility of extending NSOM into applications requiring UV light through two-photon excitation.

## VI.D. Membrane Microstructure

As in the above examples, there is considerable interest in probing and understanding the organization present in cellular membranes at the submicrometer level.[58,83,124,132,136,267,278,324] One area that is receiving increased attention concerns the presence and role of lipid microdomains in cellular function. Various measurements have revealed the presence of lateral heterogeneities in cellular membranes that may play important functional roles. For instance, small lipid microdomains may play important roles in sequestering enzymes in unique physical environments, increasing passive transport across the membrane, or in promoting vesicle fusion. Evidence for these lipid domains comes mainly from far-field diffusion measurements where small areas of a fluorescently labeled membrane are photobleached and the recovery in fluorescence measured. The presence of multiple diffusion lifetimes or large immobile fractions in the measurements suggests the presence of heterogeneity in the cellular membrane. These lipid microdomains, however, are thought to exist on the submicrometer level and are, therefore, beyond the resolution of far-field techniques.

Recently, Edidin and co-workers have begun to probe these lipid domains directly on the nanometric scale using NSOM fluorescent measurements on fixed cells.[132] These measurements build on their previous work studying the phase distribution and structure in model lipid films. Human skin fibroblast cells in which the plasma membrane was fluorescently labeled with lipid analogues were plated onto glass coverslips, fixed, and dried. NSOM fluorescence measurements reveal the presence of membrane domains or patches in the plasma membrane of the cell which ranged in size from approximately 70 to 600 nm. When compared with the simultaneous force mapping of the cell contours, fluorescence domains were seen even in areas of the membrane that appeared smooth. This argues that the patchiness seen was not simply a result of disruptions in the membrane.

Similar measurements taken on cells in which fluorescent antibodies to the HLA class I membrane proteins were introduced found a stronger correlation between structural features of the cell and the organization seen in the fluorescence.[132] In these measurements, the structure in the fluorescence tracked ridges of the cell measured in the force image. To analyze the images, a two-dimensional spatial autocorrelation function was employed to reveal the important domain sizes in the images. Using this analysis to resolve the cluster sizes of the HLA-I domains, two domain sizes of 67 and 623 nm were recovered.[132] The combined high-resolution fluores-

cence and topographical images provides a unique comparison between membrane organization and structural details of the cell.

## VI.E. Progress toward Imaging Living Cells

To date, all NSOM reports probing cellular structure have been on fixed samples. The imaging of soft biological samples such as unfixed cells is often problematic for scanning probe microscopies including NSOM. However, there have been numerous reports of NSOM imaging of fixed biological samples in aqueous environments which removes one obstacle toward the ultimate goal of imaging natural cells. The problem lies in the forces involved in the force feedback mechanism used to position and hold the NSOM tip close to the sample surface. The forces imparted to the sample during imaging are largely governed by the spring constant of the NSOM tip or compliance of the feedback system and the quality of the feedback signal. Steps to decrease the forces involved in imaging by modifying these parameters are well underway in several labs.

Fujihara et al. have been very active in both developing new probe design and in investigating new methods for reducing the forces involved in imaging. They have reported the underwater imaging of fixed mouse keratinocytes using bent NSOM probes in tapping-mode feedback and have recently begun exploring the imaging capabilities of etched probes.[106,155,263] By the immersion of the probe in an HF solution, the diameter of the probe can be etched down to a small diameter in a very controllable manner. The spring constant, $k$, for a cylindrical cantilever is given by

$$k = 3\pi d^4 E/64l^3 \quad (9)$$

where $d$ is the diameter of the cylindrical rod, $E$ is the elastic modulus of the rod material, and $l$ is the length of the cantilever.[106] The fourth power dependence on the probe diameter, therefore, provides an effective route to dramatically reduce the spring constant of the NSOM probe and decrease the forces involved in imaging. Figure 39 shows a magnified view of a bent NSOM fiber probe that has been etched down to a reduced diameter.[106] Figure 39 also shows spring constants calculated using eq 9 where both the diameter of the probe, $d$, and the length of the cantilever, $l$, were varied.[106] As can be seen from the graph, orders of magnitude reductions in the spring constant can be achieved using this approach.

Other approaches toward imaging soft samples revolve around changing or modifying the way the tip is held in feedback. One such approach may involve the use of the light exiting the NSOM probe to implement a feedback signal based on the interference between the light exiting the tip and that reflected off the sample.[78,231,232,326] This feedback mode can be truly noncontact and has been used by several groups to implement feedback at the air/liquid interface.[78,326] The technique, however, is susceptible to artifacts in the height image due to variations in sample refractive index and, in some cases, to the specific topography of the sample.[232] This will likely limit the usefulness of this technique in future applications on samples exhibiting complex topographical features until these obstacles are overcome.

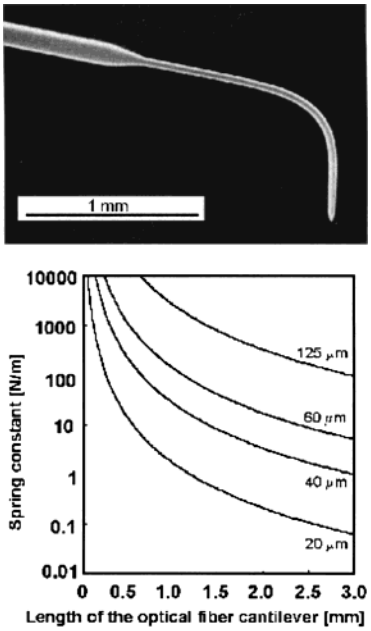


**Figure 39.** (top) Bent fiber optic NSOM probe which has its diameter reduced by etching in a HF solution. (bottom) Calculated spring constants for several different probe diameters as a function of the length of the probe. Reproduced with permission from ref 106. Copyright 1998 Elsevier Science.

The wide adoption of the tuning fork method for tip feedback may also lead to improved, gentler interactions between the NSOM tip and the sample. As mentioned earlier, the high $Q$ of the tuning fork oscillator leads to an exquisitely sensitive probe of small viscous forces.[66,67,241,248,249,254,259,265,333] Therefore, despite the high static compliance of the tuning fork, the effective compliance can be quite small leading to reduced tip−sample interactions. This has been demonstrated by imaging DNA strands deposited on a mica substrate.[66,67,248,254]

The strategies listed above basically involve modifying the fiber optic probe or changing or improving the feedback capabilities to decrease the tip−sample interactions. A final strategy involves completely changing the probe used in NSOM. For instance, the energy transfer probes mentioned in section II.C may offer a new approach toward imaging soft samples. The FRET idea for high-resolution fluorescence imaging demonstrated in Figure 6,[213] should work equally well with the acceptor dye attached to an AFM tip instead of a fiber optic probe.[8,20,211−213] AFM tips have been successfully used to image living cells which may provide a new route toward the illusive goal of high-resolution fluorescence imaging of living cells.

## VII. Conclusions

It is clear from the examples discussed here that NSOM has developed into a viable technique for elucidating new insights into sample properties at the nanometric scale. The single molecule fluorescence detection limits and spectroscopic capabilities

provide a powerful tool when combined with the high spatial resolution and simultaneous topographical information. The breadth of applications that are already taking advantage of NSOM measurements illustrates its flexibility in working conditions and unique information content. It is also clear, however, that NSOM is a work in progress.

The majority of articles written are still technical in nature, either discussing imaging characteristics or new ways of making NSOM measurements. Significant obstacles remain in areas such as the biological sciences, where probing soft or fragile samples is still problematic. However, significant hurdles have already been overcome and it seems unlikely that these new difficulties are insurmountable problems. Undoubtedly, the technique is still evolving, but what is equally true is that it has already evolved to a point where unique and useful measurements can be made on a wide range of samples. Hopefully the examples discussed here in single molecule studies, thin film analysis, and biological applications have illustrated these capabilities. For the future, the introduction of new probes, as in the apertureless design, which has the potential of significantly improving the spatial resolution possible with NSOM, may provide the next quantum leap in the development of the technique. This would firmly set NSOM apart from confocal microscopy or AFM establishing it as an important new tool in sample analysis.

## VIII. Acknowledgments

R.C.D wishes to thank Hitoshi Shiku, Christopher W. Hollars, M. Annie Lee, Chad E. Talley, Jeffrey R. Krogmeier, and Sarah A. Vickery for critically reading the manuscript and Laura Mack for help in preparing the figures. Support was provided by the NSF (Grant CHE-9612730), NSF-CAREER (Grant CHE-9703009), and Searle Scholars Program/The Chicago Community Trust.

## IX. References

(1) Special Issue on Near-Field Optics. *Ultramicroscopy* **1998**, *71*.
(2) Special Issue on Near-Field Optics. *Ultramicroscopy* **1995**, *57*.
(3) Special Issue on Near-Field Optics. *J. Microscopy*, in press.
(4) Betzig, E.; Trautman, J. K. *Science* **1992**, *257*, 189−195.
(5) Betzig, E.; Trautman, J. K.; Harris, T. D.; Weiner, J. S.; Kostelak, R. L. *Science* **1991**, *251*, 1468−1470.
(6) *Scanning Near-Field Optical Microscopy (SNOM)*; Pohl, D. W., Ed.; Academic Press: London, 1991; Vol. 12.
(7) Harris, T. D.; Grober, R. D.; Trautman, J. K.; Betzig, E. *Appl. Spectrosc.* **1994**, *48*, 14A−21A.
(8) Kopelman, R.; Tan, W. *Appl. Spectrosc. Rev.* **1994**, *29*, 39−66.
(9) Courjon, D.; Bainier, C. *Rep. Prog. Phys.* **1994**, *57*, 989−1028.
(10) Paesler, M. A.; Moyer, P. J. *Near-Field Optics: Theory, Instrumentation, and Applications*; John Wiley and Sons: New York, 1996.
(11) Vanden Bout, D. A.; Kerimo, J.; Higgins, D. A.; Barbara, P. F. *Acc. Chem. Res.* **1997**, *30*, 204−212.
(12) Buratto, S. K. *Curr. Opin. Solid State Mater. Sci.* **1996**, *1*, 485−492.
(13) Pohl, D. W. *IBM J. Res. Dev.* **1995**, *39*, 701−711.
(14) Pohl, D. W.; et. al. *Chimia* **1997**, *51*, 760−767.
(15) Heinzelmann, H.; Pohl, D. W. *Appl. Phys. A* **1994**, *59*, 89−101.
(16) Heinzelmann, H.; et. al. *Opt. Eng.* **1995**, *34*, 2441−2454.
(17) Pohl, D. W.; Hecht, B.; Heinzelmann, H. *Nanoscale Science and Technology*; 1998; pp 175−183.
(18) Lewis, A.; Lieberman, K. *Anal. Chem.* **1991**, *63*, 625A−638A.
(19) Subramaniam, V.; Kirsch, A. K.; Jovin, T. M. *Cell. Mol. Biol.* **1998**, *44*, 689−700.
(20) Fujihira, M. In *Optics at the Nanometer Scale*; Garcia, M. N.-V. a. N., Ed.; IBM: The Netherlands, 1996.
(21) Heinzelmann, H.; Lacoste, Th.; Huser, Th.; Guntherodt, H. J.; Hecht, B.; Pohl, D. W. *Thin Solid Films* **1996**, *273*, 149−153.
(22) Lewis, A.; Lieberman, K.; Ben-Ami, N. K.; Fish, G.; Khachatryan, E.; Strinkovski, A.; Shalom, S.; Druckmann, S.; Ottolenghi, M.; Ben-Ami, U. *Isr. J. Chem.* **1996**, *36*, 89−96.
(23) Fischer, U. C.; Koglin, J.; Naber, A.; Raschewski, A.; Tiemann, R.; Fuchs, H. In *Quantum Optics of Confined Systems*; Ducley, M., Bloch, D., Eds.; Kluwer Academic Publishers: Dordrecht, The Netherlands, 1996.
(24) Heinzelmann, H.; Huser, T.; Lacoste, T.; Guntherodt, H.-J.; Pohl, D. W.; Hecht, B.; Novotny, L.; Martin, O. J. F.; Hafner, C. V.; Baggenstos, H.; Wild, U. P.; Renn, A. *Opt. Eng.* **1995**, *34*, 2441−2454.
(25) Courjon, D.; Spajer, M.; Baida, F.; Bainier, C.; Davy, S. *Condens. Matter News* **1998**, *6*, 14−20.
(26) Betzig, E. R. Cornell, 1988.
(27) *Near-Field Nano/Atom Optics and Technology*; Ohtsu, M., Ed.; Springer-Verlag: Tokyo, 1998.
(28) Higgins, D. A.; Mei, E. In *Scanning Tunneling Microscopy and Spectroscopy*, 2nd ed.; Bonnell, D., Ed.; in press.
(29) Abbe, E. *Arch. Mikrosk. Anat.* **1873**, *9*, 413−468.
(30) Synge, E. H. *Philos. Mag.* **1928**, *6*, 356−362.
(31) Synge, E. H. *Philos. Mag.* **1931**, *11*, 65−80.
(32) Synge, E. H. *Philos. Mag.* **1932**, *13*, 297.
(33) Ash, E. A.; Nicholls, G. *Nature* **1972**, *237*, 510−512.
(34) Pohl, D. W.; Denk, W.; Lanz, M. *Appl. Phys. Lett.* **1984**, *44*, 651−653.
(35) Durig, U.; Pohl, D. W.; Rohner, F. *J. Appl. Phys.* **1986**, *59*, 3318−3327.
(36) Betzig, E.; Lewis, A.; Harootunian, A.; Isaacson, M.; Kratschmer, E. *Biophys. J.* **1986**, *49*, 269−279.
(37) Harootunian, A.; Betzig, E.; Isaacson, M.; Lewis, A. *Appl. Phys. Lett.* **1986**, *49*, 674−676.
(38) Betzig, E.; Harootunian, A.; Lewis, A.; Isaacson, M. *Appl. Opt.* **1986**, *25*, 1890−1900.
(39) Betzig, E.; Chichester, R. J. *Science* **1993**, *262*, 1422−1425.
(40) Xie, X. S.; Allen, E. V.; Holtom, G. H.; Dunn, R. C.; Mets, L. *SPIE Proceedings of Time-Resolved Laser Spectroscopy in Biochemistry IV*; SPIE: Bellingham, WA, 1994; pp 264−276.
(41) Xie, X. S.; Holtom, G. R.; Mets, L.; Dunn, R. C. *Ultrafast Phenom. 9* **1994**.
(42) Xie, X. S.; Dunn, R. C. *Science* **1994**, *265*, 361−364.
(43) Trautman, J. K.; Macklin, J. J.; Brus, L. E.; Betzig, E. *Nature* **1994**, *369*, 40−42.
(44) Ambrose, W. P.; Goodwin, P. M.; Martin, J. C.; Keller, R. A. *Science* **1994**, *265*, 364−367.
(45) Ambrose, W. P.; Goodwin, P. M.; Martin, J. C.; Keller, R. A. *Phys. Rev. Lett.* **1994**, *72*, 160−163.
(46) Dunn, R. C.; Allen, E. V.; Joyce, S. A.; Anderson, G. A.; Xie, X. S. *Ultramicroscopy* **1995**, *57*, 113−117.
(47) Bian, R. X.; Dunn, R. C.; Xie, X. S.; Leung, P. T. *Phys. Rev. Lett.* **1995**, *75*, 4772−4775.
(48) Bian, R. X.; Dunn, R. C.; Xie, X. S.; Leung, P. T. *Phys. Rev. Lett.* **1995**, *75*, 4772−4775.
(49) Ambrose, W. P.; Affleck, R. L.; Goodwin, P. M.; Keller, R. A.; Martin, J. C.; Petty, J. T.; Schecker, J. A.; Wu, M. *Exp. Technol. Phys.* **1995**, *41*, 237−248.
(50) Tarrach, G.; Bopp, M. A.; Zeisel, D.; Meixner, A. J. *Rev. Sci. Instrum.* **1995**, *66*, 3569−3575.
(51) Meixner, A. J.; Zeisel, D.; Bopp, M. A.; Tarrach, G. *Opt. Eng.* **1995**, *34*, 2324−2332.
(52) *Near-Field Microscopy and Spectroscopy of Single Molecules, Single Proteins and Biological Membranes*; Xie, X. S., Dunn, R. C., Eds.; World Scientific Publishing Co.: Singapore, 1996; in press.
(53) Ha, T.; Enderle, Th.; Ogletree, D. F.; Chemla, D. S.; Selvin, P. R.; Weiss, S. *Proc. Natl. Acad. Sci. U.S.A.* **1996**, *93*, 6264−6268.
(54) Trautman, J. K.; Macklin, J. J. *Chem. Phys.* **1996**, *205*, 221−229.
(55) Bopp, M. A.; Meixnew, A. J.; Tarrach, G.; Zschokke-Granacher, I.; Novotny, L. *Chem. Phys. Lett.* **1996**, *263*, 721−726.
(56) Novotny, L. *Appl. Phys. Lett.* **1996**, *69*, 3806−3808.
(57) Chang, R.; Fann, W.; Lin, S. H. *Appl. Phys. Lett.* **1996**, *69*, 2338−2340.
(58) Ha, T.; Enderle, Th.; Chemla, D. S.; Weiss, S. *IEEE J. Sel. Top. Quantum Electron.* **1996**, *2*, 1115−1128.
(59) Bopp, M. A.; Meixner, A. J.; Tarrach, G.; Zschokke-Granacher, I.; Novotny, L. *Chem. Phys. Lett.* **1996**, *263*, 721−726.
(60) Xie, X. S. *Acc. Chem. Res.* **1996**, *29*, 598−606.
(61) Chang, R.; Wei, P.-K.; Fann, W. S.; Hayashi, M.; Lin, S. H. *J. Appl. Phys.* **1997**, *81*, 3369−3376.
(62) Ruiter, A. G. T.; Veerman, J. A.; Garcia-Parajo, M. F.; van Hulst, N. F. *J. Phys. Chem. A* **1997**, *101*, 7318−7323.
(63) Bopp, M. A.; Tarrach, G.; Lieb, M. A.; Meixner, A. J. *J. Vac. Sci. Technol. A* **1997**, *15*, 1423−1426.
(64) Ha, T.; Chemia, D. S.; Enderle, Th.; Weiss, S. *Appl. Phys. Lett.* **1997**, *70*, 782−784.
(65) Talley, C.; Lee, M. A.; Dunn, R. C. *Appl. Phys. Lett.* **1998**, *72*, 2954−2956.

(66) Garcia-Parajo, M. F.; Veerman, J.-A.; Ruiter, A. G. T.; van Hulst, N. F. *Ultramicroscopy* **1998**, *71*, 311−319.
(67) Garcia-Parajo, M. F.; Veerman, J.-A.; van Noort, S. J. T.; de Grooth, B. G.; Greve, J.; van Hulst, N. F. *Bioimaging* **1998**, *6*, 43−53.
(68) Adams, D. M.; Kerimo, J.; Olson, E. J. C.; Zaban, A.; Gregg, B. A.; Barbara, P. F. *J. Am. Chem. Soc.* **1997**, *119*, 10608−10619.
(69) Kerimo, J.; Adams, D. M.; Barbara, P. F.; Kaschak, D. M.; Mallouk, T. E. *J. Phys. Chem. B* **1998**, *102*, 9451−9460.
(70) Kerimo, J.; Adams, D. M.; Vanden Bout, D. A.; Higgins, D. A.; Barbara, P. F. *Inter-Am. Photochem. Soc. News.* **1996**, *19*, 57−61.
(71) Higgins, D. A.; Barbara, P. F. *J. Phys. Chem.* **1995**, *99*, 3−7.
(72) Hollars, C. W.; Dunn, R. C. *J. Phys. Chem.* **1997**, *101*, 6313−6317.
(73) Tamm, L. K.; Bohm, C.; Yang, J.; Shao, Z.; Hwang, J.; Ediden, M.; Betzig, B. *Thin Solid Films* **1996**, *284−285*, 813−816.
(74) Ade, H.; Toledo-Crow, R.; Vaez-Iravani, M.; Spontak, R. J. *Langmuir* **1996**, *12*, 231−234.
(75) Higgins, D. A.; Reid, P. J.; Barbara, P. F. *J. Phys. Chem.* **1996**, *100*, 1174−1180.
(76) Blatchford, J. W.; Gustafson, T. L.; Epstein, A. J.; Vanden Bout, D. A.; Kerimo, J.; Higgins, D. A.; Barbara, P. F.; Fu, D. K.; Swager, T. M.; MacDiarmid, A. G. *Phys. Rev. B* **1996**, *54*, R3686−R3686.
(77) Reid, P. J.; Higgins, D. A.; Barbara, P. F. *J. Phys. Chem.* **1996**, *100*, 3892−3899.
(78) Kramer, A.; Hartmann, T.; Eschrich, R.; Guckenberger, R. *Ultramicroscopy* **1998**, *71*, 123−132.
(79) Weston, K. D.; Buratto, S. K. *J. Phys. Chem. B* **1997**, *101*, 5684−5691.
(80) Brunner, R.; Bietsch, A.; Hollricher, O.; Marti, O.; Lambacher, A. *Surf. Interface Anal.* **1997**, *25*, 492−495.
(81) DeAro, J. A.; Weston, K. D.; Buratto, S. K.; Lemmer, U. *Chem. Phys. Lett.* **1997**, *277*, 532−538.
(82) Hofkens, J.; Latterini, L.; Vanoppen, P.; Faes, H.; Jeuris, K.; De Feyter, S.; Kerimo, J.; Barbara, P. F.; De Schryver, F. C.; Rowan, A. E.; Nolte, R. J. M. *J. Phys. Chem.* **1997**, *101*, 10588−10598.
(83) Tamm, L. K.; Bohm, C.; Yang, J.; Shao, Z.; Hwang, J.; Edidin, M.; Betzig, E. *Thin Solid Films* **1996**, *284−285*, 813−816.
(84) Kajikawa, K.; Hara, M.; Sasabe, H.; Knoll, W. *Colloids Surf. A* **1997**, *126*, 97−101.
(85) Nagahara, L. A.; Yanagi, H.; Tokumoto, H. *Nanotechnology* **1997**, *8*, A50−A53.
(86) Webster, S.; Smith, D. A.; Batchelder, D. N.; Lidzey, D. G.; Bradley, D. D. C. *Ultramicroscopy* **1998**, *71*, 275−279.
(87) Rucker, M.; De Schryver, F. C.; Vanoppen, P.; Jeuris, K.; De Feyter, S.; Hotta, J.; Masuhara, H. *Nucl. Instrum. Methods Phys. Res. B* **1997**, *131*, 30−37.
(88) Pohl, D. W. *Thin Solid Films* **1995**, *264*, 250−254.
(89) Wei, P.-K.; Hsu, J.-H.; Fann, W.; Chuang, K.-R.; Lee, H.-T.; Chen, S.-A. *Appl Opt.* **1997**, *36*, 3301−3304.
(90) Hsu, J.-H.; Wei, P.-K.; Fann, W.; Chuang, K.-R.; Chen, S.-A. *J. Appl. Phys.* **1998**, *83*, 1782−1784.
(91) Hsu, J. H.; Wei, P. K.; Fann, W. S.; Chuang, K. R.; Chen, S. A. *Ultramicroscopy* **1998**, *71*, 263−267.
(92) Wei, P. K.; Hsu, J. H.; Hsieh, B. R.; Fann, W. S. *Adv. Mater.* **1996**, *8*, 573−576.
(93) Mei, E.; Higgins, D. A. *Langmuir* **1998**, *14*, 1945−1950.
(94) Mei, E.; Higgins, D. A. *Appl. Phys. Lett.* **1998**, *73*, 3515−3517.
(95) Fann, W. S.; Wei, P. K.; Hsu, J. H.; Hsieh, B. R.; Chuang, K. R.; Chen, S. A. *Proc. SPIE-Int. Soc. Opt. Eng.* **1995**, *2384*, 158−165.
(96) Zeisel, D.; Dutoit, B.; Deckert, V.; Roth, T.; Zenobi, R. *Anal. Chem.* **1997**, *69*, 749−754.
(97) Higgins, D. A.; Kerimo, J.; Vanden Bout, D. A.; Barbara, P. F. *J. Am. Chem. Soc.* **1996**, *118*, 4049−4058.
(98) Birnbaum, D.; Kook, S. K.; Kopelman, R. *J. Phys. Chem.* **1993**, *97*, 3091−3094.
(99) Kirsch, A. K.; Meyer, C. K.; Huesmann, H.; Mobius, D.; Jovin, T. M. *Ultramicroscopy* **1998**, *71*, 295−302.
(100) Kirsch, A. K.; Schaper, A.; Huesmann, H.; Rampi, M. A.; Mobius, D.; Jovin, T. M. *Langmuir* **1998**, *14*, 3895−3900.
(101) Kaupp, G.; Herrmann, A.; Haak, M. *J. Vac. Sci. Technol. B* **1997**, *15*, 1521−1526.
(102) Kaupp, G.; Herrmann, A. *J. Phys. Org. Chem.* **1997**, *10*, 675−679.
(103) Muramatsu, H.; Chiba, N.; Fujihira, M. *Appl. Phys. Lett.* **1997**, *71*, 2061−2063.
(104) Fujihira, M.; Do, L.-M.; Koike, A.; Han, E.-M. *Appl. Phys. Lett.* **1996**, *68*, 1787−1789.
(105) Fujihira, M.; Monobe, H.; Koike, A.; Ivanov, G. R.; Muramatsu, H.; Chiba, N.; Yamamoto, N.; Ataka, T. *Ultramicroscopy* **1998**, *71*, 269−274.
(106) Muramatsu, H.; Chiba, N.; Yamamoto, N.; Homma, K.; Ataka, T.; Shigeno, M.; Monobe, H.; Fujihira, M. *Ultramicroscopy* **1998**, *71*, 73−79.
(107) Nagahara, L. A.; Tokumoto, H. *Thin Solid Films* **1996**, *281−282*, 647−650.
(108) Chiba, N.; Muramatsu, H.; Nakajima, K.; Homma, K.; Ataka, T.; Fujihira, M. *Thin Solid Films* **1996**, *273*, 331−334.
(109) Ataka, T.; Muramatsu, H.; Nakajima, K.; Chiba, N.; Homma, K.; Fujihira, M. *Thin Solid Films* **1996**, *273*, 154−16.
(110) Pohl, D. W.; Novotny, L.; Hecht, B.; Heinzelmann, H. *Thin Solid Films* **1996**, *273*, 161−167.
(111) Williamson, R. L.; Miles, M. J. *J. Vac. Sci. Technol. B* **1996**, *14*, 809−811.
(112) Yamada, H.; Tokumoto, H.; Akamine, S.; Fukuzawa, K.; Kuwano, H. *J. Vac. Sci. Technol. B* **1996**, *14*, 812−815.
(113) Nagahara, L. A.; Tokumoto, H. *J. Vac. Sci. Technol. B* **1996**, *14*, 800−803.
(114) Rucker, M.; Vanoppen, P.; De Schryver, F. C.; Ter Horst, J. J.; Hotta, J.; Masuhara, H. *Macromolecules* **1995**, *28*, 7530−7535.
(115) Rogers, J. A.; Bao, Z.; Dhar, L. *Appl. Phys. Lett.* **1998**, *73*, 294−296.
(116) Hamano, M.; Irie, M. *Jpn. J. Appl. Phys.* **1996**, *35*, 1764−1767.
(117) Oesterschulze, E. *Surf. Coat. Technol.* **1997**, *97*, 694−706.
(118) Fujihira, M. In *Forces in Scanning Probe Methods*; al., H.-J. G. e., Ed.; Kluwer Academic Publishers: Dordrecht, The Netherlands, 1995.
(119) Nakajima, K.; Muramatsu, H.; Chiba, N.; Ataka, T.; Fujihira, M. *Thin Solid Films* **1996**, *273*, 327−330.
(120) Dunn, R. C.; Holtom, G. H.; Mets, L.; Xie, X. S. *J. Phys. Chem.* **1994**, *98*, 3094−3098.
(121) Betzig, E.; Chichester, R. J.; Lanni, F.; Taylor, D. L. *Bioimaging* **1993**, *1*, 129−135.
(122) Tan, W.; Shi, Z. Y.; Smith, S.; Birnbaum, D.; Kopelman, R. *Science* **1992**, *258*, 778−781.
(123) van Hulst, N. F.; Moers, M. H. P. *IEEE Eng. Med. Biol.* **1996**, 51−57.
(124) Enderle, TH.; Ha, T.; Ogletree, D. F.; Chemla, D. S.; Magowan, C.; Weiss, S. *Proc. Natl. Acad. Sci. U.S.A.* **1997**, *94*, 520−525.
(125) Haydon, P. G.; Marchese-Ragona, S.; Basarsky, T. A.; Szulczewski, M.; McCloskey, M. *J. Microsc.* **1996**, *182*, 208−216.
(126) Jia, W.; Dacheng, L. *SPIE* **1995**, 115−117.
(127) Moers, M. H. P.; Kalle, W. H. J.; Ruiter, A. G. T.; Wiegant, J. C. A. G.; Raap, A. K.; Greve, J.; deGrooth, B. C.; van Hulst, N. F. *J. Microscopy* **1996**, *182*, 40−45.
(128) Valaskovic, G. A.; Holton, M.; Morrison, G. H *Ultramicroscopy* **1995**, *57*, 212−218.
(129) Iwabuchi, S.; Muramatsu, H.; Chiba, N.; Kinjo, Y.; Murakami, Y.; Sakaguchi, T.; Yokoyama, K.; Tamiya, E. *Nucleic Acids Res.* **1997**, *25*, 1662−1663.
(130) Rousso, I.; Khachatryan, E.; Gat, Y.; Brodsky, I.; Ottolenghi, M.; Sheves, M.; Lewis, A. *Proc. Natl. Acad. Sci. U.S.A.* **1997**, *94*, 7937−7941.
(131) Tamiya, E.; Iwabuchi, S.; Nagatani, N.; Murakami, Y.; Sakaguchi, T.; Yokoyama, K.; Chiba, N.; Muramatsu, H. *Anal. Chem.* **1997**, *69*, 3697−3701.
(132) Hwang, J.; Gheber, L. A.; Margolis, L.; Edidin, M. *Biophys. J.* **1998**, *74*, 2184−2190.
(133) Gheber, L. A.; Hwang, J.; Edidin, M. *Appl. Opt.* **1998**, *37*, 3574−3581.
(134) van Hulst, N. F.; Garcia-Parajo, M. F.; Moers, M. H. P.; Veerman, J.-A.; Ruiter, A. G. T. *J. Struct. Biol.* **1997**, *119*, 222−231.
(135) Deckert, V.; Zeisel, D.; Zenobi, R. *Anal. Chem.* **1998**, *70*, 2646−2650.
(136) Enderle, Th.; Ha, T.; Chemla, D. S.; Weiss, S. *Ultramicroscopy* **1998**, *71*, 303−309.
(137) Moyer, P. J.; Kammer, S. B. *Appl. Phys. Lett.* **1996**, *68*, 3380−3382.
(138) Hell, S. W.; Booth, M.; Wilms, S.; Schnetter, C. M.; Kirsch, A. K.; Arndt-Jovin, D. J.; Jovin, T. M. *Opt. Lett.* **1998**, *23*, 1238−1240.
(139) Kirsch, A. K.; Subramaniam, V.; Striker, G.; Schnetter, C.; Arndt-Jovin, D. J.; Jovin, T. M. *Biophys. J.* **1998**, *75*, 1513−1521.
(140) Subramaniam, V.; Kirsch, A. K.; Rivera-Pomar, R. V.; Jovin, T. M. *J. Fluoresc.* **1997**, *7*, 381−385.
(141) Kirsch, A. K.; Meyer, C. K.; Jovin, T. M. *J. Microsc.* **1997**, *185*, 396−401.
(142) Brunner, R.; Bietsch, A.; Hollricher, O.; Marti, O. *Rev. Sci. Instrum.* **1997**, *68*, 1769−1772.
(143) Smolyaninov, I. I.; Atia, W. A.; Pilevar, S.; Davis, C. C. *Ultramicroscopy* **1998**, *71*, 177−182.
(144) Lambelet, P.; Pfeffer, M.; Sayah, A.; Marquis-Weible, F. *Ultramicroscopy* **1998**, *71*, 117−121.
(145) Keller, T. H.; Rayment, T.; Klenerman, D.; Stephenson, R. J. *Rev. Sci. Instrum.* **1997**, *68*, 1448−1454.
(146) Muramatsu, H.; Chiba, N.; Ataka, T.; Iwabuchi, S.; Nagatani, N.; Tamiya, E.; Fujihira, M. *Opt. Rev.* **1996**, *3*, 470−474.
(147) Muramatsu, H.; Chiba, N.; Nakajima, K.; Ataka, T.; Fujihira, M.; Hitomi, J.; Ushiki, T. *Scanning Microsc.* **1996**, *10*, 975−982.
(148) Wiegrabe, W.; Monajembashi, S.; Dittmar, H.; Greulich, K.-O.; Hafner, S.; Hildebrandt, M.; Kittler, M.; Lochner, B.; Unger, E. *Surf. Interface Anal.* **1997**, *25*, 510−513.

(149) Hollricher, O.; Brunner, R.; Marti, O. *Ultramicroscopy* **1998**, *71*, 143−147.
(150) Mertesdorf, M.; Schonhoff, M.; Lohr, F.; Kirstein, S. *Surf. Interface Anal.* **1997**, *25*, 755−759.
(151) Keller, T. H.; Raymet, T.; Klenerman, D. *Biophys. J.* **1998**, *74*, 2076−2079.
(152) Uttamchandani, D.; McCulloch, S. *Adv. Drug Deliv. Rev.* **1996**, *21*, 239−247.
(153) Hong, M. K.; Erramilli, S.; Huie, P.; James, G.; Jeung, A. *SPIE* **1996**, *2863*, 54−63.
(154) Tamiya, E.; Iwabuchi, S.; Murakami, Y.; Sakaguchi, T.; Yokoyama, K.; Chiba, N.; Muramatsu, H. *SPIE* **1996**, *2836*, 12−15.
(155) Muramatsu, H.; Chiba, N.; Umemoto, T.; Homma, K.; Nakajima, K.; Ataka, T.; Ohta, S.; Kusumi, A.; Fujihira, M. *Ultramicroscopy* **1995**, *61*, 265−269.
(156) Jenei, A.; Kirsch, A. K.; Subramaniam, V.; Arndt-Jovin, D. J.; Jovin, T. M. *Biophys. J.* **1999**, *76*, 1092−1100.
(157) Paesler, M. A.; Moyer, P. J.; Jahncke, C. J.; Johnson, C. E.; Reddick, R. C.; Warmack, R. J.; Ferrell, T. L. *Phys. Rev. B* **1990**, *42*, 6750−6753.
(158) Girard, C.; Courjon, D. *Phys. Rev. B* **1990**, *42*, 9340−9349.
(159) Meixner, A. J.; Bopp, M. A.; Tarrach, G. *Appl. Opt.* **1994**, *33*, 7995−8000.
(160) Moyer, P. J.; Jahncke, C. L.; Paesler, M. A.; Reddick, R. C.; Warmack, R. J. *Phys. Lett. A* **1990**, *145*, 343−347.
(161) Reddick, R. C.; Warmack, R. J.; Chilcott, D. W.; Sharp, S. L.; Ferrell, T. L. *Rev. Sci. Instrum.* **1990**, *61*, 3669−3677.
(162) Ferrell, T. L.; Goundonnet, J. P.; Reddick, R. C.; Sharp, S. L.; Warmack, R. J. *J. Vac. Sci. Technol. B* **1991**, *9*, 525−1517.
(163) Guerra, J. M. *Appl. Opt.* **1990**, *29*, 3741−3752.
(164) Betzig, R. E.; Trautman, J. K. (AT&T Bell Laboratories). U.S. Patent 5 272 330, 1993.
(165) Valaskovic, G. A.; Holton, M.; Morrison, G. H. *Appl. Opt.* **1995**, *34*, 1215−1228.
(166) Williamson, R. L.; Miles, M. J. *J. Appl. Phys.* **1996**, *80*, 4804−4812.
(167) Weston, K. D.; DeAro, J. A.; Buratto, S. K. *Rev. Sci. Instru.* **1996**, *67*, 2924−2929.
(168) Curran, J. E.; Page, J. S.; Pick, U. *Thin Solid Films* **1982**, *97*, 259−276.
(169) Hass, G.; Waylonis, J. E. *J. Opt. Soc. Am.* **1961**, *51*, 719−722.
(170) Krueger, W. H.; Pollack, S. R. *Surf. Sci.* **1972**, *30*, 263−279.
(171) Hollars, C. W.; Dunn, R. C. *Rev. Sci. Instrum.* **1996**, *69*, 1747−1752.
(172) Hecht, B.; Bielefeldt, H.; Pohl, D. W.; Novotny, L.; Heinzelmann, H. *J. Appl. Phys.* **1998**, *84*, 5873−5882.
(173) Novotny, L.; Pohl, D. W.; Regli, P. *J. Opt. Soc. Am. A* **1994**, *11*, 1768−1779.
(174) Novotny, L.; Pohl, D. W. *Photons and Local Probes*; 1995; pp 21−33.
(175) Kavaldjiev, D. I.; Toledo-Crow, R.; Vaez-Iravani, M. *Appl. Phys. Lett.* **1995**, *67*, 2771−2773.
(176) Stahelin, M.; Bopp, M. A.; Tarrach, G.; Meixner, A. J.; Zschokke-Granacher, I. *Appl. Phys. Lett.* **1996**, *68*, 2603−2605.
(177) LaRosa, A. H.; Yakobson, B. I.; Hallen, H. D. *Appl. Phys. Lett.* **1995**, *67*, 2597−2599.
(178) Lienau, Ch.; Richter, A.; Elsaesser, T. *Appl. Phys. Lett.* **1996**, *69*, 325−327.
(179) Goetz, M.; Drews, D.; Zahn, D. R. T.; Wannemacher, R. *J. Luminesc.* **1998**, *76−77*, 306−309.
(180) Emory, S. R.; Nie, S. *Anal. Chem.* **1997**, *69*, 2631−2635.
(181) Jahncke, C. L.; Paesler, M. A.; Hallen, H. D. *Appl. Phys. Lett.* **1995**, *67*, 2483−2485.
(182) Jahncke, C. L.; Hallen, H. D.; Paesler, M. A. *J. Raman Spectrosc.* **1996**, *27*, 579−586.
(183) Zeisel, D.; Deckert, V.; Zenobi, R.; Vo-Dinh, T. *Chem. Phys. Lett.* **1998**, *283*, 381−385.
(184) Betzig, E.; Grubb, S. G.; Chichester, R. J.; DiGiovanni, D. J.; Weiner, J. S. *Appl. Phys. Lett.* **1993**, *63*, 3550−3552.
(185) Bukofsky, S. J.; Grober, R. D. *Appl. Phys. Lett.* **1997**, *71*, 2749−2751.
(186) Mononobe, S.; Naya, M.; Saiki, T.; Ohtsu, M. *Appl. Opt.* **1997**, *36*, 1496−1500.
(187) Yatsui, T.; Kourogi, M.; Ohtsu, M. *Appl. Phys. Lett.* **1997**, *71*, 1756−1758.
(188) Mononobe, S.; Ohtsu, M. *J. Lightwave Technnol.* **1997**, *15*, 1051−1055.
(189) Zeisel, D.; Nettesheim, S.; Dutoit, B.; Zenobi, R. *Appl. Phys. Lett.* **1996**, *68*, 2491−2492.
(190) Dutoit, B.; Zeisel, D.; Deckert, V.; Zenobi, R. *J. Phys. Chem. B* **1997**, *101*, 6955−6959.
(191) Hoffmann, P.; Dutoit, B.; Salathe, R.-P. *Ultramicroscopy* **1995**, *61*, 165−170.
(192) Chuang, Y. H.; Gung, K. G.; Wang, C. J.; Huang, J. Y.; Pan, C. L. *Rev. Sci. Instrum.* **1998**, *69*, 437−439.
(193) Lambelet, P.; Sayah, A.; Pfeffer, M.; Philipona, C.; Marquis-Weible, F. *Appl. Opt.* **1998**, *37*, 7289−7292.
(194) Pilevar, S.; Edinger, K.; Atia, W.; Smolyaninov, I.; Davis, C. *Appl. Phys. Lett.* **1998**, *72*, 3133−3135.
(195) Veerman, J. A.; Otter, A. M.; Kuipers, L.; van Hulst, N. F. *Appl. Phys. Lett.* **1998**, *72*, 3115−3117.
(196) Muranishi, M.; Sato, K.; Hosaka, S.; Kikukawa, A.; Shintani, T.; Ito, K. *Jpn. J. Appl. Phys.* **1997**, *36*, L942.
(197) Betzig, E.; Trautman, J. K.; Weiner, J. S.; Harris, T. D.; Wolfe, R. *Appl. Opt.* **1992**, *31*, 4563−4568.
(198) Jackson, J. D. *Classical Electrodynamics*; Wiley: New York, 1975.
(199) Bouwkamp, C. J. *Rep. Prog. Phys.* **1954**, *17*, 35−100.
(200) Bachelot, R.; Lahrech, A.; Gleyzes, P.; Boccara, A. C. *SPIE* **1996**, *2782*, 570−581.
(201) Bachelot, R.; Gleyzes, P.; Boccara, A. C. *Appl. Opt.* **1997**, *36*, 2160−2170.
(202) Furukawa, H.; Kawata, S. *Opt. Commun.* **1998**, *148*, 221−224.
(203) Kawata, S.; Tani, T. *Opt. Lett.* **1996**, *21*, 1768−1770.
(204) Novotny, L.; Bian, R. X.; Xie, X. S. *Phys. Rev. Lett.* **1997**, *79*, 645−648.
(205) Novotny, L.; Sanchez, E. J.; Xie, X. S. *Ultramicroscopy* **1998**, *71*, 21−29.
(206) Zenhausern, F.; Martin, Y.; Wickramasinghe, H. K. *Science* **1995**, *269*, 1083−1085.
(207) Sanchez, E. J.; Novotny, L.; Xie, X. S. *Phys. Rev. Lett.* **1999**, *82*, 4014−4017.
(208) Kopelman, R.; Lewis, A.; Lieberman, K. *J. Lumin.* **1990**, *45*, 298−299.
(209) Kopelman, R.; Lieberman, K.; Lewis, A.; Tan, W. *J. Lumin.* **1991**, *48−49*, 871−875.
(210) Lieberman, K.; Harush, S.; Lewis, A.; Kopelman, R. *Science* **1990**, *247*, 59−61.
(211) Sekatskii, S. K.; Letokhov, V. S. *Appl. Phys. B* **1996**, *63*, 525−530.
(212) Sekatskii, S. K.; Letokhov, V. S. *JETP Lett.* **1996**, *63*, 319−323.
(213) Vickery, S. A.; Dunn, R. C. *Biophys. J.* **1999**, in press.
(214) Akamine, S.; Kuwano, H.; Yamada, H. *Appl. Phys. Lett.* **1996**, *68*, 579−581.
(215) Bergossi, O.; Bachelot, R.; Wioland, H.; Wurtz, G.; Laddada, R.; Adam, P. M.; Bijeon, J. L.; Royer, P. *Acta Phys. Pol., A* **1997**, *93*, 393−398.
(216) Bouju, X.; Dereux, A.; Vigneron, J. P.; Girard, C. *J. Vac. Sci. Technol. B* **1996**, *14*, 816−819.
(217) Fillard, J. P.; Castagne, M.; Benfedda, M.; Lahimer, S.; Danzebrink, H. U. *Appl. Phys. A* **1996**, *63*, 421−425.
(218) van Hulst, N. F.; Moers, M. H. P.; Noordman, O. F. J.; Tack, R. G.; Segerink, F. B.; Bolger, B. *Appl. Phys. Lett.* **1993**, *62*, 461−463.
(219) Ruiter, A. G. T.; Moers, M. H. P.; van Hulst, N. F.; de Boer, M. *J. Vac. Sci. Technol. B* **1996**, *14*, 597−601.
(220) Ruiter, A. G. T.; Moers, M. H. P.; Jalocha, A.; van Hulst, N. F. *Ultramicroscopy* **1995**, *61*, 139−143.
(221) Noell, W.; Abraham, M.; Mayr, K.; Ruf, A.; Barenz, J.; Hollricher, O.; Marti, O.; Guthner, P. *Appl. Phys. Lett.* **1997**, *70*, 1236−1238.
(222) Abraham, M.; Ehrfeld, W.; Lacher, M.; Mayr, K.; Noell, W.; Guthner, P.; Barenz, J. *Ultramicroscopy* **1998**, *71*, 93−98.
(223) Munster, S.; Werner, S.; Mihalcea, C.; Scholz, W.; Oesterschulze, E. *J. Microsc.* **1997**, *186*, 17−22.
(224) Tanaka, Y.; Fukuzawa, K.; Kuwano, H. *J. Appl. Phys.* **1998**, *83*, 3547−3551.
(225) Mihalcea, C.; Scholz, W.; Werner, S.; Munster, S.; Oesterschulze, E.; Kassing, R. *Appl. Phys. Lett.* **1996**, *68*, 3531−3533.
(226) Sakai, A.; Yamada, H.; Fujita, M.; Baba, T. *Jpn. J. Appl. Phys.* **1998**, *37*, 517−521.
(227) Sasaki, K.; Fujiwara, H.; Masuhara, H. *J. Vac. Sci. Technol. B* **1997**, *15*, 2786−2790.
(228) Sasaki, K.; Fujiwara, H.; Masuhara, H. *Appl. Phys. Lett.* **1997**, *70*, 2647−2649.
(229) Sugiura, T.l; Okada, T. *SPIE-Int. Soc. Opt. Eng.* **1998**, *3260*, 4−14.
(230) Hsu, J. W. P.; Lee, M.; Deaver, B. S. *Rev. Sci. Instrum.* **1995**, *66*, 3177−3181.
(231) Kramer, A.; Hartmann, T.; Stadler, S. M.; Guckenberger, R. *Ultramicroscopy* **1995**, *62*, 191−195.
(232) Shiku, H.; Krogmeier, J. R.; Dunn, R. C. *Langmuir* **1999**, in press.
(233) Guttroff, G.; Keto, J. M.; Shih, C. K.; Anselm, A.; Streetman, B. G. *Appl. Phys. Lett.* **1996**, *68*, 3620−3622.
(234) Courjon, D.; Vigoureux, J. M.; Spajer, M.; Sarayeddine, K.; Leblanc, S. *Appl. Opt.* **1990**, *29*, 3734−3740.
(235) Reddick, R. C.; Warmack, R. J.; Ferrell, T. L. *Phys. Rev. B* **1989**, *39*, 767−790.
(236) Betzig, E.; Finn, P. L.; Weiner, J. S. *Appl. Phys. Lett.* **1992**, *60*, 2484−2486.
(237) Toledo-Crow, R.; Yang, P. C.; Chen, Y.; Vaez-Iravani, M. *Appl. Phys. Lett.* **1992**, *60*, 2957−2959.
(238) Shchemelinin, A.; Rudman, M.; Lieberman, K.; Lewis, A. *Rev. Sci. Instrum.* **1993**, *64*, 3538−3541.
(239) Betzig, R. E. (AT&T Bell Laboratories). U.S. Patent 5,254,854, 1993.
(240) Leong, J.-K.; Williams, C. C. *Appl. Phys. Lett.* **1995**, *66*, 1432−1434.

(241) Karrai, K.; Grober, R. D. *Ultramicroscopy* **1995**, *61*, 197−205.
(242) Wei, C.-C.; Wei, P.-K.; Fann, W. *Appl. Phys. Lett.* **1995**, *67*, 3835−3837.
(243) Zhu, X.; Huang, G. S.; Zhou, H. T.; Dai, Y. D. *Solid State Commun.* **1996**, *98*, 661−664.
(244) Gregor, M. J.; Blome, P. G.; Schofer, J.; Ulbrich, R. G. *Appl. Phys. Lett.* **1996**, *68*, 307−309.
(245) Durkan, C.; Shvets, I. V. *J. Appl. Phys.* **1996**, *80*, 5659−5664.
(246) Durkan, C.; Shvets, I. V. *J. Appl. Phys.* **1996**, *79*, 1219−1223.
(247) Pfeffer, M.; Lambelet, P.; Marquis-Weible, F. *Rev. Sci. Instrum.* **1997**, *68*, 4478−4482.
(248) Ruiter, A. G. T.; Veerman, J. A.; van der Werf, K. O.; van Hulst, N. F. *Appl. Phys. Lett.* **1997**, *71*, 28−30.
(249) Atia, W. A.; Davis, C. C. *Appl. Phys. Lett.* **1997**, *70*, 405−407.
(250) Yang, Y. T.; Heh, D.; Wei, P. K.; Fann, W. S.; Gray, M. H.; Hsu, J. W. P. *J. Appl. Phys.* **1997**, *81*, 1623−1627.
(251) Hsu, J. W. P.; McDaniel, A. A.; Hallen, H. D. *Rev. Sci. Instrum.* **1997**, *68*, 3093−3095.
(252) Wei, P. K.; Fann, W. S. *J. Appl. Phys.* **1998**, *83*, 3461−3468.
(253) Wei, P. K.; Fann, W. S. *Ultramicroscopy* **1998**, *71*, 159−163.
(254) Ruiter, A. G. T.; van der Werf, K. O.; Veerman, J. A.; Garcia-Parajo, M. F.; Rensen, W. H. J.; van Hulst, N. F. *Ultramicroscopy* **1998**, *71*, 149−157.
(255) Davy, S.; Spajer, M.; Courjon, D. *Appl. Phys. Lett.* **1998**, *73*, 2594−2596.
(256) Williamson, R. L.; Miles, M. J. *J. Appl. Phys.* **1996**, *80*, 3143−3146.
(257) Froehlich, F. F.; Milster, T. D. *Appl. Phys. Lett.* **1997**, *70*, 1500−1502.
(258) Drummond Roby, M. A.; Wetsel, G. C.; Wang, C.-Y. *Appl. Phys. Lett.* **1996**, *69*, 130−132.
(259) Karrai, K.; Grober, R. D. *Appl. Phys. Lett.* **1995**, *66*, 1842−1844.
(260) Lieberman, K.; Lewis, A.; Fish, G.; Shalom, S.; Jovin, T. M.; Schaper, A.; Cohen, S. R. *Appl. Phys. Lett.* **1994**, *65*, 648−650.
(261) Lieberman, K.; Ben-Ami, N.; Lewis, A. *Rev. Sci. Instrum.* **1996**, *67*, 3567−3572.
(262) Shalom, S.; Lieberman, K.; Lewis, A.; Cohen, S. R. *Rev. Sci. Instrum.* **1992**, *63*, 4061−4065.
(263) Muramatsu, H.; Chiba, N.; Homma, K.; Nakajima, K.; Ataka, T.; Ohta, S.; Kusumi, A.; Fujihira, M. *Appl. Phys. Lett.* **1995**, *66*, 3245−3247.
(264) Muramatsu, H.; Chiba, N.; Ataka, T.; Monobe, H.; Fujihira, M. *Ultramicroscopy* **1995**, *57*, 141−146.
(265) Muramatsu, H.; Yamamoto, N.; Umemoto, T.; Homma, K.; Chiba, N.; Fujihira, M. *Jpn. J. Appl. Phys.* **1997**, *36*, 5753−5758.
(266) Mitsuoka, Y.; Nakajima, K.; Homma, K.; Chiba, N.; Muramatsu, H.; Ataka, T.; Sato, K. *J. Appl. Phys.* **1998**, *83*, 3998−4002.
(267) Talley, C. E.; Cooksey, G.; Dunn, R. C. *Appl. Phys. Lett.* **1996**, *69*, 3809−3811.
(268) Monobe, H.; Koike, A.; Muramatsu, H.; Chiba, N.; Yamamoto, N.; Ataka, T.; Fujihira, M. *Ultramicroscopy* **1998**, *71*, 287−293.
(269) Nakajima, K.; Mitsuoka, Y.; Chiba, N.; Muramatsu, H.; Ataka, T.; Sato, K.; Fujihira, M. *Ultramicroscopy* **1998**, *71*, 257−262.
(270) Fujihira, M.; Monobe, H.; Muramatsu, H.; Ataka, T. *Ultramicroscopy* **1995**, *57*, 118−123.
(271) Chiba, N.; Muramatsu, H.; Ataka, T.; Fujihira, M. *Jpn. J. Appl. Phys.* **1995**, *34*, 321−324.
(272) Fujihira, M.; Monobe, H.; Yamamoto, N.; Muramatsu, H.; Chiba, N.; Nakajima, K.; Ataka, T. *Ultramicroscopy* **1995**, *61*, 271−277.
(273) Fujimura, T.; Edamatsu, K.; Itoh, T.; Shimada, R.; Imada, A.; Koda, T.; Chiba, N.; Muramatsu, H.; Ataka, T. *Opt. Lett.* **1997**, *22*, 489−491.
(274) Fujihira, M.; Monobe, H.; Muramatsu, H.; Ataka, T. *Chem. Lett.* **1994**, 657−660.
(275) Lieberman, K.; Terkel, H.; Rudman, M.; Ignatov, A.; Lewis, A. *SPIE* **1996**, *2793*, 481−488.
(276) Ben-Ami, U.; Tessler, N.; Ben-Ami, N.; Nagar, R.; Fish, G.; Lieberman, K.; Eisenstein, G.; Lewis, A.; Nielsen, J. M.; Moeller-Larsen, A. *Appl. Phys. Lett.* **1996**, *68*, 2337−2339.
(277) Shiku, H.; Dunn, R. C. *J. Phys. Chem. B* **1998**, *102*, 3791−3797.
(278) Hollars, C. W.; Dunn, R. C. *Biophys. J.* **1998**, *75*, 342−353.
(279) Girard, C.; Dereux, A. *Rep. Prog. Phys.* **1996**, *59*, 657−699.
(280) Torok, P.; Sheppard, C. J. R.; Varga, P. *J. Mod. Opt.* **1996**, *43*, 1167−1183.
(281) Fukuzawa, K.; Kuwano, H. *J. Appl. Phys.* **1996**, *80*, 4799−4803.
(282) Fukuzawa, K.; Kuwano, H. *J. Appl. Phys.* **1996**, *79*, 8174−8178.
(283) Furukawa, H.; Kawata, S. *Opt. Commun.* **1996**, *132*, 170−178.
(284) Bozhevolnyi, S. I. *Phys. Rev. B* **1996**, *54*, 8177−8185.
(285) Grober, R. D.; Rutherford, T.; Harris, T. D. *Appl. Opt.* **1996**, *35*, 3488−3495.
(286) Keller, O. *Ultramicroscopy* **1998**, *71*, 1−9.
(287) Martin, O. J. F.; Girard, C.; Dereaux, A. *Helv. Phys. Acta* **1995**, *68*, 195−196.
(288) Paule, E.; Reineker, P. *J. Lumin.* **1998**, *76−77*, 299−302.
(289) Wei, P. K.; Chang, R.; Hsu, J. H.; Lin, S. H.; Fann, W. S.; Hsieh, B. R. *Opt. Lett.* **1996**, *21*, 1876−1878.
(290) Xiao, M. *Appl. Phys. Lett.* **1996**, *69*, 3125−3127.
(291) Xiao, M. *Chem. Phys. Lett.* **1997**, *270*, 167−177.
(292) Xiao, M.; Zayats, A.; Siqueiros, J. *Phys. Rev. B* **1997**, *55*, 1824−1837.
(293) Novotny, L. *J. Opt. Soc. Am. A* **1997**, *14*, 91−104.
(294) Novotny, L. *J. Opt. Soc. Am. A* **1997**, *14*, 105−113.
(295) Novotny, L.; Hecht, B.; Pohl, D. W. *J. Appl. Phys.* **1997**, *81*, 1798−1806.
(296) Bethe, H. A. *Phys. Rev.* **1944**, *66*, 163−182.
(297) Bouwkamp, C. J. *Philips Res. Rep.* **1950**, *5*, 401−422.
(298) Bouwkamp, C. J. *Philips Res. Rep.* **1950**, *5*, 321−332.
(299) Leviatan, Y. *J. Appl. Phys.* **1986**, *60*, 1577−1583.
(300) Roberts, A. *J. Appl. Phys.* **1989**, *65*, 2896−2899.
(301) Roberts, A. *J. Opt. Soc. Am. A* **1987**, *4*, 1970−1983.
(302) Roberts, A. *J. Appl. Phys.* **1991**, *70*, 4045−4049.
(303) Novotny, L.; Hafner, C. *Phys. Rev. E* **1994**, *50*, 4094−4106.
(304) Christensen, D. A. *Ultramicroscopy* **1995**, *57*, 189−195.
(305) Hecht, B.; Bielefeldt, H.; Inouye, Y.; Pohl, D. W.; Novotny, L. *J. Appl. Phys.* **1997**, *81*, 2492−2498.
(306) Novotny, L.; Hecht, B.; Pohl, D. W. *Ultramicroscopy* **1998**, *71*, 341−344.
(307) Chance, R. R.; Prock, A.; Silbey, R. *Adv. Chem. Phys.* **1978**, *37*, 1−65.
(308) Xie, X. S.; Trautman, J. K. *Annu. Rev. Phys. Chem.* **1998**, *49*, 441−480.
(309) Conboy, J. C.; Olson, E. J. C.; Adams, D. M.; Kerimo, J.; Zaban, A.; Gregg, B. A.; Barbara, P. F. *J. Phys. Chem.* **1998**, *102*, 4516−4525.
(310) Krausch, G.; Mlynek, J. *Microelectron. Eng.* **1996**, *32*, 219−228.
(311) Fujihira, M. *Ann. N.Y. Acad. Sci.* **1998**, *852*, 306−329.
(312) Jiang, S.; Ichihashi, J.; Monobe, H.; Fujihira, M.; Ohtsu, M. *Opt. Commun.* **1994**, *106*, 173−177.
(313) Vanden Bout, D. A.; Kerimo, J.; Higgins, D. A.; Barbara, P. F. *J. Phys. Chem.* **1996**, *100*, 11843−11849.
(314) Higgins, D. A.; Vanden Bout, D. A.; Kerimo, J.; Barbara, P. F. *J. Phys. Chem.* **1996**, *100*, 13794−13803.
(315) Vanden Bout, D. A.; Yip, W. T.; Hu, D.; Fu, D. K.; Swager, T. M.; Barbara, P. F. *Science* **1997**, *277*, 1074−1077.
(316) Mei, E.; Higgins, D. A. *J. Phys. Chem. A* **1998**, *102*, 7558−7563.
(317) Wang, H.; Bardo, A. M.; Collinson, M. M.; Higgins, D. A. *J. Phys. Chem. B* **1998**, *102*, 7231−7237.
(318) Huser, Th.; Lacoste, Th.; Heinzelmann, H.; Kitzerow, H.-S. *J. Chem. Phys.* **1998**, *108*, 7876−7880.
(319) Moyer, P. J.; Walzer, K.; Hietschold, M. *Appl. Phys. Lett.* **1995**, *67*, 2129−2131.
(320) Lacoste, Th.; Huser, Th.; Prioli, R.; Heinzelmann, H. *Ultramicroscopy* **1998**, *71*, 333−340.
(321) Teetsov, J.; Vanden Bout, D. A. Private communication.
(322) Kook, S. K.; Kopelman, R. *J. Phys. Chem.* **1992**, *96*, 10672−10676.
(323) Pohl, D. W.; Bach, H.; Bopp, M. A.; Deckert, V.; Descouts, P.; Eckert, R.; Guntherodt, H.-J.; Hafner, C.; Hecht, B.; Heinzelmann, H.; Huser, T.; Jobin, M.; Keller, U.; Lacoste, T.; Lambelet, P.; Marquis-Weible, F.; Martin, O. J. F.; Meixner, A. J.; Nechay, B.; Novotny, L.; Pfeiffer, M.; Philipona, C.; Plakhotnik, T.; Renn, A.; Sayah, A.; Segura, J.-M.; Sick, B.; Siegner, U.; Tarrach, G.; Vahldieck, R.; Wild, U. P.; Zeisel, D.; Zenobi, R. *Chimia* **1997**, *51*, 760−767.
(324) Hwang, J.; Tamm, L. K.; Bohm, C.; Ramalingam, T.; Betzig, E.; Edidin, M. *Science* **1995**, *270*, 610−614.
(325) Moers, M. H. P.; Gaub, H. E.; van Hulst, N. F. *Langmuir* **1994**, *10*, 2774−2777.
(326) Shiku, H.; Dunn, R. C. *J. Microsc.* **1999**, in press.
(327) Shiku, H.; Dunn, R. C. *J. Microsc.* **1999**, in press.
(328) Ivanov, G. R.; Petkova, J. I.; Okabe, Y.; Aoki, D.; Takano, H.; Kawate, H.; Fujihira, M. *Supramol. Sci.* **1997**, *4*, 549−557.
(329) Fujihira, M.; Sakomura, M.; Aoki, D.; Koike, A. *Thin Solid Films* **1996**, *273*, 168−176.
(330) Smith, S.; Monson, E.; Merritt, G.; Tan, W.; Birnbaum, D.; Shi, Z. Y.; Thorsrud, B. A.; Harris, C.; Grahn, H. T.; Ploog, K.; Merlin, R.; Orr, B.; Langmore, J.; Kopelman, R. *SPIE, Scanning Probe Microscopies III*; SPIE: Bellingham, WA, 1993; pp 81−92.
(331) Atia, W. A.; Pilevear, S.; Gungor, A.; Davis, C. C. *Ultramicroscopy* **1998**, *71*, 379−382.
(332) Bozhevolnyi, S. I.; Vohnsen, B. *J. Opt. Soc. Am. B* **1997**, *14*, 166−16635.
(333) Tsai, D. P.; Lu, Y. Y. *Appl. Phys. Lett.* **1998**, *73*, 2724−2726.

CR980130E